Erasmus Mundus

ITM - CNR
Istituto per la Tecnologia delle Membrane

UNIVERSITÀ DELLA CALABRIA

UNIVERSIDADE NOVA DE LISBOA

VYSOKÁ ŠKOLA CHEMICKO-TECHNOLOGICKÁ V PRAZE

Scuola di Dottorato di Ricerca in

Scienze e Ingegneria dell'Ambiente, delle Costruzioni e dell'Energia - XXIX ciclo

CHIM/07 FONDAMENTI CHIMICI DELLE TECNOLOGIE

Dipartimento di Ingegneria per l'Ambiente e il Territorio e Ingegneria Chimica (DIATIC)

Ph.D. Thesis

Development of Tailored Hydrogel Composite Membranes for Application in Membrane Contactors

Ph.D. Candidate

Shabnam Majidi Salehi

Tutors

Prof. Efrem Curcio

Dr. Gianluca Di Profio

Dr. Enrica Fontananova

Co-tutors

Prof. Joao Crespo

Dr. Eng. Vlasmil Fila

Coordinator

Prof. Pietro Pantano

Rende, May 2017

Universita della Calabria

Dipartimento di Ingegneria per l'Ambiente e il Territorio e Ingegneria Chimica (DIATIC)

Scuola di Dottorato di Ricerca in

Scienze e Ingegneria dell'Ambiente, delle Costruzioni e dell'Energia - XXIX ciclo

CHIM/07 FONDAMENTI CHIMICI DELLE TECNOLOGIE

Development of Tailored Hydrogel Composite Membranes for Application in Membrane Contactors

Ph.D. Candidate

Shabnam Majidi Salehi

Tutors

Prof. Efrem Curcio

Dr. Gianluca Di Profio

Dr. Enrica Fontananova

Abstract

This work was performed during the period from November 2013 to May 2015 in the Institute on Membrane Technology (ITM-CNR) at the University of Calabria (UNICAL), under supervision of Prof. Efrem Curcio, Dr. Gianluca Di Profio and Dr. Enrica Fontananova, from May 2015 to December 2015 at Universidade Nova de Lisboa (UNL), under supervision of Prof. Joao Crespo and from March 2016 to September 2016 at the University of Chemistry and Technology (ICT) Prague, under supervision of Dr. Eng. Vlastmil Fila. The main objective of this study was to design and develop tailored hydrogel composite membranes for application in membrane contactors, in particular, membrane distillation and membrane crystallization. Among various methods for membrane surface functionalization, surface photo-initiated graft polymerization technique (at UNICAL) and surface coating by incorporating nanoparticles (at UNL) were investigated to fabricate tailored hydrogel composite membranes.

In the first year at the University of Calabria, various hydrogel composite membranes were prepared by using photo-initiated polymerization method. The possibility of fine tuning the porosity and the chemical nature of hydrogels, were implemented with the preparation of composites containing diverse hydrogel components (monomer and cross-linker) and ratio among them. The selection of hydrogel components was based on the possibility to obtain homogeneous and stable composites by using specific polymeric porous membranes as supports. The resulting composite membranes were characterized by electron scanning microscopy, surface chemistry analysis, swelling degree, ion exchange capacity and water contact angle measurements. Furthermore, virgin and hydrogel composite membranes were used in membrane distillation and crystallization experiments and the performance improvement was evaluated. As a result, higher water-transfer flux and enhanced ion rejection than traditional MD membranes was observed in MD treatment of saline solutions. When such HCMs used in membrane assisted crystallization of carbonate calcium (biomineralization), a wide range of crystal morphologies, most of them displaying a polycrystalline or mesocrystalline structure, was obtained in a great variety of experimental conditions. We demonstrated that this composite provides the opportunity to fine control the delivery of additives to the gel network through the porous structure of both support membrane and hydrogel layer, thus affecting crystallization kinetics, and crystal morphologies.

In the second year of the study at Universidade Nova de Lisboa, hydrogel composite membranes with tailored surface roughness and patterning were designed to examine the influence of the topography of such composite membranes on the growth of protein crystals. Iron oxide nanoparticles (NPs) were used as topographical designers providing a good control of membrane surface roughness and patterning. Surface morphology and topography of the prepared membranes were characterized using electron scanning microscopy, profilometry analysis and contact angle measurements. Finally, their performance was evaluated in the crystallization of Lysozyme used as a model protein and the effect of surface chemistry and topography on the heterogeneous nucleation of lysozyme crystals was investigated. We demonstrated that roughness influences crystallization, but we also show that excessive roughness may be deleterious, since it increases the number of crystals formed at the expenses of crystal size. Therefore, there is an optimum value of roughness for the formation of a low number of well-faced crystals with a larger size.

In the third year at the University of Chemistry and Technology Prague, the modeling of membrane crystallization was studied. The main goal of this work was to develop general model of membrane crystallization process. The development of this model involved the fundamental theories and models in membrane process and crystallization engineering, especially the models described the mass and heat transfers in membrane module and the crystal size distribution (CSD) determined by both nucleation and crystal growth processes based on the concept of the population balance equation.

The experimental results of this study, allows to achieve new insight to fabricate and develop the novel hydrogel composite membranes with proper properties and novel functionality for application in membrane distillation and membrane crystallization processes.

Sommario

Sommario: L'obiettivo principale di questo studio è stato quello di sviluppare e progettare membrane composite con idrogel per l'applicazione in contattori a membrana, in particolare la distillazione e la cristallizzazione a membrana. Tra i vari metodi esistenti per la funzionalizzazione della superficie di membrana sono state studiate tecniche di foto-polimerizzazione e rivestimento superficiale incorporando nanoparticelle per la fabbricazione di membrane composite con idrogel.

Nel primo anno, sono state sviluppate presso l'Istituto per la Tecnologia delle Membrane del CNR (CNR-ITM) diverse membrane composite con idrogel utilizzando un metodo di foto-polimerizzazione. La possibilità di ottimizzare la porosità e la natura chimica degli idrogel è stata realizzata attraverso la preparazione di compositi contenenti diversi componenti di idrogel (monomero e cross-linker) e il loro rapporto. La selezione dei componenti dell'idrogel è stata basata sulla necessità di ottenere compositi omogenei e stabili usando specifiche membrane polimeriche porose come supporti. Le membrane composite risultanti sono state caratterizzate presso l'Università della Calabria (UNICAL) tramite microscopia a scansione elettronica, analisi chimica superficiale, misurazioni dell'angolo di contatto all'acqua. Inoltre, i supporti polimerici e le membrane composite sono state utilizzate in test di distillazione (MD) e cristallizzazione (MCr) a membrana così da valutarne le prestazioni. Nel trattamento MD di soluzioni saline è stato osservato un maggiore flusso trans-membrana dell'acqua e una reiezione di NaCl maggiore rispetto alle membrane MD tradizionali. Quando tali HCM sono utilizzate nella cristallizzazione di carbonato di calcio (biomineralizzazione), una vasta gamma di morfologie di cristalli, la maggior parte dei quali mostrano una struttura policristallina e mesocristallina ad architettura gerarchica su differente scala, è stata ottenuta in una grande varietà di condizioni sperimentali. E' stato dimostrato che tali compositi offrono l'opportunità di regolare il controllo dell'apporto di additivi alla matrice di gel per mezzo della struttura porosa sia della membrana di supporto che dello strato di idrogel, in modo da influenzare la cinetica di cristallizzazione e le morfologie delle strutture cristalline ottenute.

Nel secondo anno, sono state progettate presso l'Universidade Nova de Lisboa membrane composite con idrogel con rugosità e pattern superficiale controllati al fine di determinare l'influenza della topografia di tali membrane composite sulla crescita di cristalli proteici. A tal fine,

sono state utilizzate nanoparticelle di ossido di ferro (INP) come modificatori superficiali in grado di conferire un controllo della rugosità e del patterning delle superfici. La morfologia superficiale e la topografia delle membrane preparate sono state caratterizzate utilizzando la microscopia a scansione elettronica, la profilometria e le misure dell'angolo di contatto. Infine, le loro prestazioni sono state valutate nella cristallizzazione del lisozima, utilizzato come proteina modello, così da determinare l'effetto della chimica superficiale e della topografia sulla nucleazione eterogenea dei cristalli di lisozima. Si è dimostrato che la rugosità influenza la cristallizzazione, ma anche che l'eccessiva rugosità può essere deleteria, in quanto aumenta il numero di cristalli formati a spese della dimensione dei cristalli stessi. Pertanto, si è dimostrato l'esistenza di un valore ottimale di rugosità per la formazione di un ridotto numero di cristalli ben visibili di dimensioni più grandi.

Nel terzo anno è stata studiata presso l'Università di Chimica e Tecnologia di Praga la modellizzazione della cristallizzazione a membrana. L'obiettivo principale di questo lavoro è stato quello di sviluppare il modello generale del processo di cristallizzazione a membrana. Lo sviluppo di questo modello ha riguardato le teorie e i modelli fondamentali in processi a membrana e di ingegneria di cristallizzazione, in particolare dei modelli di trasferimento di massa e calore nel modulo a membrana e la distribuzione delle dimensioni dei cristalli (CSD), determinate sia dai processi di nucleazione che di crescita cristallina, basati sull'equazione del bilancio di popolazione.

I risultati sperimentali di questo studio hanno consentito di ottenere nuove conoscenze per la fabbricazione e lo sviluppo di nuove membrane composite con idrogel con proprietà innovative e nuove funzionalità per la loro applicazione in processi di distillazione e cristallizzazione a membrana.

Acknowledgments

First, I am grateful to Dr. Gianluca Di Profio, Dr. Enrico Fontananova and Prof. Efrem Curcio for giving me the opportunity to work in their research group at ITM-CNR, supporting me through the difficulties of my research work.

I would like to thank Prof. Joao Crespo for guiding my research at University of Lisbon (my first host university in the frame of EUDIME program), advising and encouraging me for my study. I am also thankful to his research group Prof. Isabel Coelhoso and Dr. Carla Portugal for supporting me during my stay in Portugal.

I wish thank to Dr. Vlastmil Fila for guiding my research at University of Prague (my second host university in the frame of EUDIME program) and helping me in developing my knowledge in the modeling field.

I would like also to thank Dr. Rocco Caliandro and his research group in the institute of crystallography, Bari, for his contribution to the statistical analysis on my resulting data and providing me with the opportunity to perform some of my crystallization experiments in his institute.

Lastly, I would like to thank my parents- Amir and Kobi, for their love and support through the years of my study. And thanks to my sister (Nassim) and my brother (Hossein) too, for their support and encouragement.

Shabnam Majidi Salehi

University of Calabria

May 2017

Table of Contents

Publications

- Membrane Distillation by Novel Hydrogel Composite Membranes, Shabnam Majidi Salehi; Gianluca Di Profio; Enrica Fontananova; Fiore P. Nicoletta; Efrem Curcio; Giovanni De Filpo, *Journal of Membrane Science*, 504, 220-229 (2016)

- Bioinspired Synthesis of $CaCO_3$ Superstructures through a Novel Hydrogel Composite Membranes Mineralization Platform: A Comprehensive View, Gianluca Di Profio; Shabnam Majidi Salehi; Rocco Caliandro; Pietro Guccione; Giovanni Nico; Efrem Curcio; Enrica Fontananova, *Advanced Materials*, 24, 610–616 (2016)

- Membrane Crystallization Technology, Gianluca Di Profio; Shabnam Majidi Salehi; Efrem Curcio; Enrico Driolli; Comprehensive Membrane Science and Engineering II, *Elsevier*, Article: 12247 (2017)

- Engineering Hydrogel Composite Membranes Incorporating Iron Oxide Nanoparticles as Suitable Hetronucleant for Protein Crystallization, Shabnam Majidi Salehi.; Anna C. Manjua; Carla A. M. Portugal; Joao G. Crespo; Isabel M. Coelhoso; Enrica Fontananova; Efrem Curcio; Gianluca Di Profio (Under preparation)

List of Tables

List of Figures

List of Abbreviations and Symbols

AA: acrylic acid

AGMD: air gap membrane distillation

CA: contact angle

CNT: classical nucleation theory

CSD: crystal size distribution

DCMD: direct contact membrane distillation

DGM: dusty gas model

EGDMA: ethylene glycol dimethacrylate

GA: glutaraldehyde

HCM: hydrogel composite membrane

HEMA: 2-hydroxyethyl methacrylate

HET: hetrogenous nucleation

HEWL: hen egg white lysozyme

HOM: homogenous nucleation

IEC: ion exchange capacity

MAA: methacrylic acid

MC: membrane contactor

MCr: membrane crystallization

MD: membrane distillation

MF: microfiltration

MIP: molecularly imprinted polymers

NF: nanofiltration

NPs: nanoparticles

LEP; liquid pressure entry

PBE: population balance equation

PEDGE: poly (ethylene glycol) diglycidyl ether

PEGDMA: polyethylene glycol dimethacrylate

PES: polyether sulfone

PLSR: partial least square regression

PP: polypropylene

PVA: polyvinyl alcohol

PV: pervaporation

RO: reverse osmosis

SGMD: sweeping gas membrane distillation

UF: ultrafiltration

VMD: vacuum membrane distillation

θ: contact angle

γ: surface tension

γ_{eff}: effective nucleus/solution interface energy

ε: overall surface porosity

ξ: activity coefficient

h: latent heat of vaporization

μ: electrochemical potential

τ: tortuosity factor

υ_0: molecular volume

φ : electrical potential

Ω: molar volume

a: activity

φ: volume factor

A: pre-exponential kinetic parameter

Am: membrane area

A$_{het}$: pre-exponential kinetic parameter for heterogeneous nucleation

A$_{hom}$: pre-exponential kinetic parameter for homogeneous nucleation

C^{*}: solubility

C_b: concentration in the bulk

C_m: concentration close to the membrane surface

D_i^k : Knudsen diffusion coefficient

G: crystal growth rate

$\varDelta G$: variation of the Gibbs free energy

Δp: vapor pressure gradient

ΔT: temperature gradient

δ: thickness of the membrane

j: trans-membrane flux

k_B: Boltzmann's constant

MW: molecular weight

J: nucleation rate

n: number of moles

n^*: critical size

N_a: Avogadro number

p: partial pressure

P: hydrostatic pressure

p^0: vapor pressure of pure component

P_{entry}: entry pressure limit

R: gas constant

r: curvature radius

r_p: pore radius

$r_{v,B}$: birth rate

$r_{v,D}$: dead rate

$r_{s^*,D}$: transfer rate

S: supersaturation

T: absolute temperature

t: time

T_{cry}: crystallization temperature

T_b: temperature in the bulk

T_m: temperature close to the membrane surface

T_p: temperature in permeate

t_{ind}: induction times

V: volume

W^*: nucleation work

x: liquid mole fraction

y: vapor mole fraction

Chapter I:

Introduction

1.1. Membrane Contactors: An Introduction to the Technology

Membranes are frequently used in the industry as an easy and efficient tool for separation processes. Among the large variety of membrane operations, membrane contactors (MCs) are relatively new membrane-based devices, and because of their potential advantages, are gaining consideration both in industry and science fields. A membrane contactor is a device where separation of compounds is accomplished due to a specific driving force through the membrane from the one phase to the other on opposite sides [1, 2]. This module achieves gas/liquid or liquid/liquid mass transfer without dispersion of one phase within another (Figure 1). The membrane represents only an interface and can be defined as a perm-selective barrier between two homogenous phases and the mass transport is due to a diffusive process through the membrane pores from one phase to the other. All traditional stripping, scrubbing, absorption and liquid–liquid extraction operations, as well as emulsification and crystallization can be carried out according to this configuration [3].
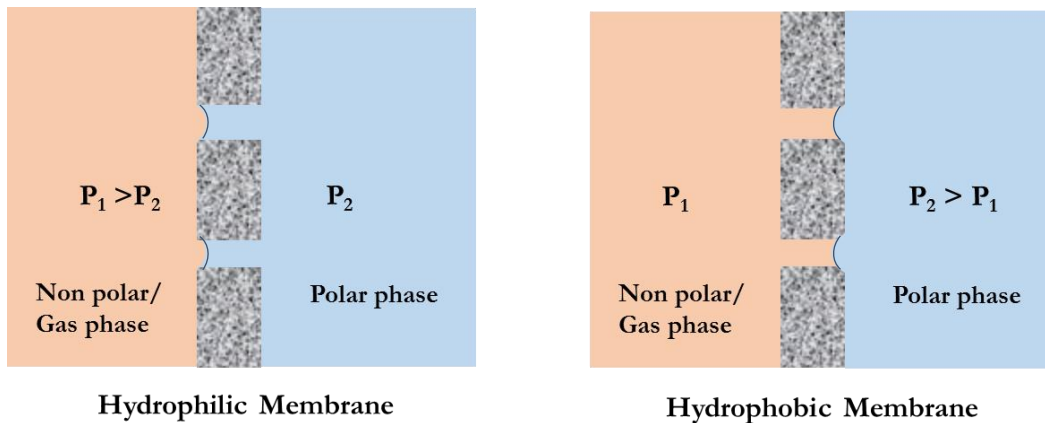
Figure 1 Schematic representation of membrane contactor: microporous, symmetric, hydrophobic/ hydrophilic membranes; P, pressure in each phase

The performances of membrane contactors depend on the properties of the membranes used. In general, high hydrophobicity is required to prevent wetting and mixing between contacting phases; high overall porosity leads to high fluxes, but might cause bubble coalescence in gas/liquid operations. Fluxes also increase with pore size, whereas the breakthrough pressure (LEP)

decreases; a low thickness reduces the resistance to mass transport through the membrane, whereas, in membrane distillation, the amount of heat lost by conduction is increased. Despite the apparent operational complexity, considerable advantages offered by membrane contactor technology make these devices very useful in a range of liquid/liquid and gas/liquid applications such as fermentation, pharmaceuticals, wastewater treatment, semiconductor manufacturing, carbonation of beverages, metal ion extraction, protein extraction, VOC removal from waste gas, membrane distillation/ osmotic distillation and membrane crystallization [4].

1.2. Membrane Distillation Technology

Membrane distillation (MD) is an emerging membrane technology used for desalination of sea or brackish water, solution concentration, recovery of volatile compounds from aqueous solutions and other separation and purification processes [5, 6]. The term MD comes from the similarity of the MD process to conventional distillation as both technologies are based on the vapor/liquid equilibrium for separation and both require heat to be supplied to the feed solution to achieve the necessary latent heat of vaporization.

1.2.1. General Principle of Membrane Distillation

Membrane distillation refers to a thermally driven transport of vapor through non-wetted porous hydrophobic membranes, with the vapor pressure difference between the two sides of the membrane pores being the driving force. The feed side of the membrane is operated at hot temperature and the permeate side at cold temperature (Figure 2). When a microporous hydrophobic membrane separates two aqueous solutions at different temperatures, selective mass transfer across the membrane occurs: this process takes place at atmospheric pressure and at temperatures which may be much lower than the boiling point of the solutions. The hydrophobicity of the membrane prevents the transport of the liquid phase across the pores of the partition while water vapor can be transported across them from the warm side, condensing at the cold surface [7].
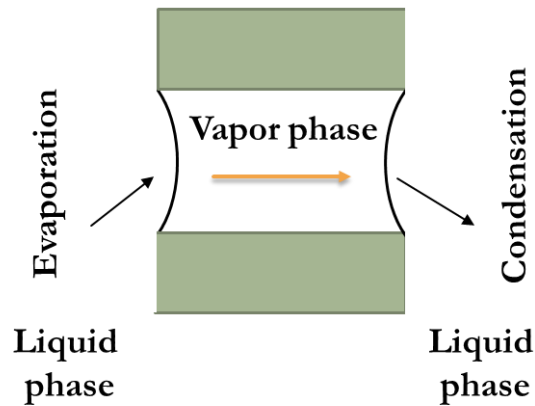
Figure 2 Schematic representation of membrane distillation process

1.2.2. Operational Configurations

Membrane distillation may be operated in different configurations in which several possibilities are applied on the permeate side such as direct contact membrane distillation (DCMD), sweeping gas membrane distillation (SGMD), vacuum membrane distillation (VMD) and air gap membrane distillation (AGMD) as shown in Figure 3. All configurations have in common that liquid feed is maintained in direct contact with the hot side of the membrane without penetrating the pores. The difference between the configurations is found only in the permeate side [5]. In DCMD, the feed as well as the permeate side are aqueous solutions. The feed is maintained at hot temperature and the permeate at cold temperature giving rise to a transmembrane temperature difference which induces a vapor pressure difference. Consequently, volatile molecules evaporate at the hot liquid/vapor interface across the membrane towards the cold permeate side and condense in the cold liquid/vapor interface inside the membrane module. In SGMD a cold inert gas is applied on the permeate side which carries the vapor molecules and condensation occurs outside the membrane module. The VMD arrangement generally uses smaller pore sizes than the other MD configurations because vacuum is applied in this case and the risk of pore wetting is high. AGMD arrangement is used to considerably reduce the heat loss by conduction and temperature polarization, by placing an air gap inside the membrane module between the permeate side and the condensing surface [6].
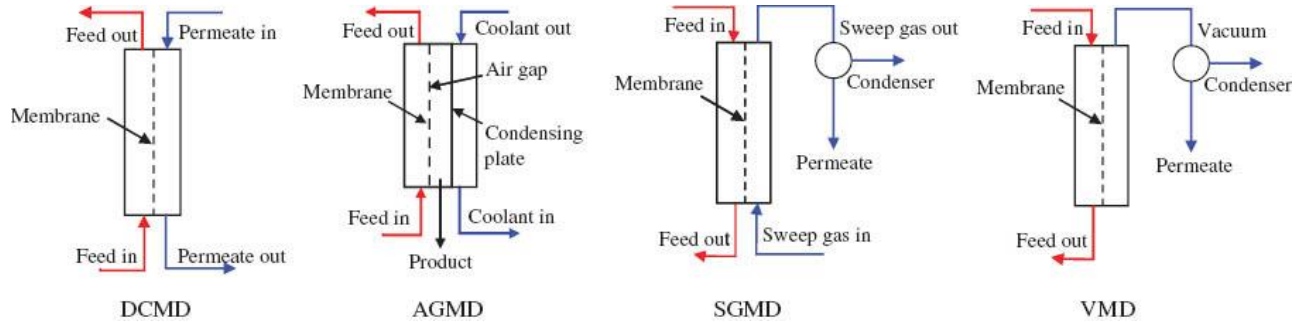
Figure 3 Different configurations of MD

Direct contact membrane distillation is the simplest MD configuration, and is the most widely used in laboratory research. In this configuration, both the aqueous feed and permeate are in direct contact with the surface of a hydrophobic porous membrane and the temperature difference across the membrane provides the driving force to generate water flux. Like other membrane processes, the temperature and concentration polarization leads the temperature and concentration at the membrane surface to differ from the bulk temperature measured in the feed and in the distillate and performs as the heat and mass transfer resistance in the conventional membrane distillation. While, the highly-concentrated region near the hydrophobic porous membrane interface is an ideal nucleation promoting circumstance in the crystallization process. Compared with the ultrasonic accelerating and adding seeds technologies, the membrane process has more controllable operational parameters (temperatures and pressure of feed and permeate sides, membrane material, and area, and so forth), which increases the operability of supersaturation regulation. This reveals the general benefits and application potential of membrane process to industrial crystallization, especially the solution crystallization [8].

1.3. Membrane Crystallization Technology

Well-controlled crystallization is the best method for preparing materials that are uniform in shape, size, structure and purity. Crystal growth as well as nucleation depends on supersaturation degree. The local gradient of supersaturation sometimes acts as a limiting factor in respect to uniformity of the product quality. Membrane crystallization (MCr) is an innovative methodology to control the generation of supersaturation; and the use of MD technique in the concentration of a solution by solvent removal in the vapour phase is proposed for this new technology [9]. The first application of a membrane as a crystallizer dates to a few decades ago and to date several publications have been described the use of membrane crystallization technology and its advantages over conventional evaporative techniques. MCr, is today recognized as an innovative and efficient method for producing enhancing crystallization of organic/inorganic materials, by allowing the formation of crystals with reduced and uniform size with high purity as well as large and single crystals for biotechnological application and X-ray crystallography analysis [10-12]. The main features of MCr are: (1) the use of membranes as the physical support for mass transport in vapour phase, (2) the role of the porous surface of the membrane as suitable tool to activate heterogeneous nucleation mechanism, and (3) the possibility to induce nucleation and crystal growth in separate sites, thus reducing the risk of membrane fouling and pore blocking even when the membrane acts as heterogeneous nucleation support. These features represent a potential application of MCr in the field of controlled crystallization processes especially in the case of bio(macro)molecules like proteins [13-16]. Furthermore, MCr technology is expected to represent an attractive option for realizing integrated and highly efficient industrial productive processes, well satisfying the requirements of the process intensification strategy [17-19]. A significant example in this sense is seawater desalination, where a rational integration of MCr technology with traditional pressure-driven membrane operations, might determine substantial improvements in terms of water quality, product recovery factor, overall cost, environmental impact and brine disposal management. In addition, separation and recovery of minerals (i.e. NaCl, KCl and Na_2CO_3) with high purity as well as other compounds of high economic benefit (i.e. barium, strontium and lithium) from the seawater is another advantage of using MCr unit in the integrated desalination systems [20, 21]

1.3.1. Working principle of Membrane Crystallization

The general working principle of MCr can be considered as an extension of the membrane distillation or the osmotic membrane distillation, where diffusion of solvent molecules in vapour phase through a porous membrane, under a gradient of temperature or concentration as driving force, generates supersaturation in crystallizing solution. Supersaturation is driving force for crystallization which induce crystal nucleation and growth (Figure 5). According to this design, porous hydrophobic membranes are used to separate the crystallizing solution and the distillate solution. When the membrane is prevented to be wet from the adjacent solutions, no mass transfer through the membrane occurs in liquid phase. Wetting of the membrane, with the consequent deleterious direct passage of liquids, can be avoided when the pressure of the solutions facing it is lower than the liquid entry pressure (LEP), defined by the Young-Laplace's equation [Atkin et al. 1993]:

$$P_{entry} = -\frac{(2\,\sigma\cos\theta)}{r_p} \qquad (1)$$

Where σ is the liquid surface tension, θ is the contact angle between the liquid crystallizing solution and the surface of membrane (Figure 4) and r_p is the pore radius.
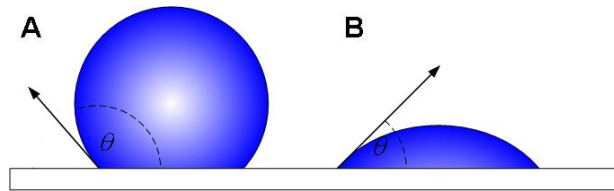
Figure 4 Definition of contact angle: $90° < \theta < 180°$, hydrophobic surface (A); $0° < \theta < 90°$, hydrophilic surface (B)

According to the equation above, for, $90° < \theta < 180°$, P_{entry} is positive. It means that hydrophobic membranes can be used for hydrophilic solutions and hydrophilic membrane are suitable for hydrophobic solutions. For a pressure, lower than P_{enry}, the two liquids are stopped at

the entrance of each pore on both membrane sides, thus generating a curved profile as shown in Figure 5.
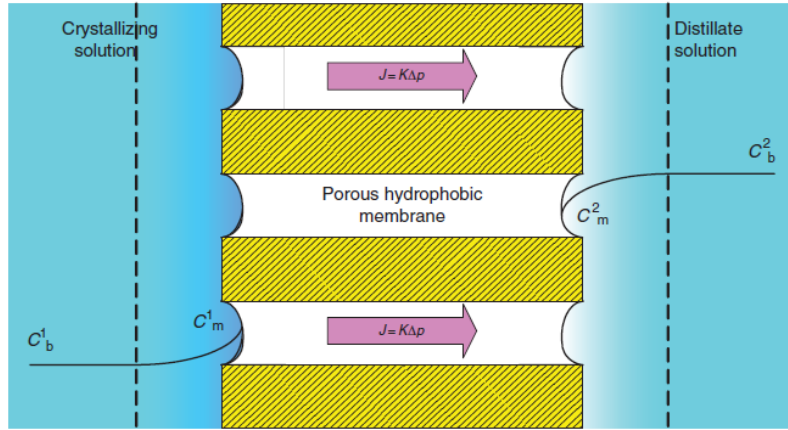
Figure 5 General principle of membrane crystallizer: C_b, bulk concentration; C_m, concentration close to the membrane surface; J, transmembrane flux; K, phenomenological constant; ΔP, partial pressure gradient between two sides of membrane [10]

In membrane crystallization, the membrane does not behave as a selective barrier, but it provides at the same time, the physical support for mass transport in vapour phase, thus generating supersaturation in crystallizing solution and the solid support to promote heterogeneous nucleation mechanism [10]. According to the classical nucleation theory (CNT), the nucleation rate $J\,[m^{-3}s^{-1}]$ for homogeneous nucleation can be expressed as [22]:

$$J = A\exp(\frac{-B}{\ln S^2})$$

(2)

In this equation, $A[m^{-3}S^{-1}]$ and $B[unitless]$ are kinetic parameters and S is the supersaturation ratio. In the presence of a heterogeneous surface in the supersaturated solution, the apparent interfacial energy γ decreases. In this case, the nucleation barrier is smaller and heterogeneous nucleation will start at lower supersaturation level compared to homogeneous nucleation. For heterogeneous nucleation, the effective interfacial energy becomes, $\gamma_{eff} = \emptyset\gamma$ with $0 < \emptyset < 1$, so that the term of B in eq. 2 can be smaller than for homogeneous nucleation. In the case of an ideal smooth surface, volume function $\emptyset$, can be evaluated by:

$$\emptyset = \frac{1}{4}(2 + \cos\theta)(1 - \cos\theta)^2 \tag{3}$$

Where, θ is the contact angle between the crystalizing solution and the membrane surface. In the case of heterogeneous nucleation induced by a porous membrane surface, this equation can be used:

$$\emptyset_{por} = \frac{1}{4}(2 + \cos\theta)(1 - \cos\theta)^2 \left[1 - \varepsilon \frac{(1 + \cos\theta)^2}{(1 - \cos\theta)^2}\right]^3 \tag{4}$$

With ε is the surface porosity [23].

1.3.2. Control of Supersaturation by means of Membrane

Supersaturation is the driving force for crystallization and the rates of nucleation and crystal growth depend on it. By choosing a suitable membrane and operating conditions, the extent of the crystalline population (crystal size distribution (CSD)), the crystals morphology (size, habit and shape) and structure properties as well as purity can be properly controlled. The fine control of the transmembrane flux and its effect on crystallization has been studied by membrane assisted crystallization processes. Generally, in MCr systems, the variation of the "thermodynamic parameters" such as temperature, concentration, flow rate and etc. in the direction of decreasing flux, produces at the same time a decrease of supersaturation generation rate by solvent removal, with the consequent tendency towards an extension of induction time but also a decrease of solubility which lead to the increase of supersaturation. Induction time is defined as time between the microdroplet deposition and the appearance of the first crystal. As induction time is inversely proportional to nucleation rate, it means that crystals are simulated to appear earlier and nucleation is accelerated. Accordingly, a parabolic behavior is usually observed in the curves displaying the relation between induction time and one of the thermodynamic parameters, due to the competition of the two forces on the overall process. When only "kinetic parameters" are varied in the direction of increasing the trans-membrane flux, supersaturation generation rate increases as well, and crystals are proven to nucleate faster due to the rapid establishment of a high level of supersaturation [24]. Control of trans-membrane flux in a membrane crystallization also has an

influence on the purity of the obtained crystals. Generally, high local supersaturation which generates a growth rate higher than that critical threshold value (which separates regions of impurity inclusion development and the growth of purer crystals), can reduce the crystal purity [25].

1.3.3. Heterogeneous Nucleation on the Membrane Surface

To create an environment that favors nucleation the use of solid templates (nucleants) has become a common practice. Such nucleants could help to enhance the chances of any single trial producing crystalline material thus reducing the initial concentration used for screening and/or to increase the nucleation rate, with consequent effect on crystal size and size distribution. In the nucleant-assisted interaction among the solute molecules, the surface will support the proper molecular orientation thus leading to the formation of crystalline clusters with well-ordered organization of the building blocks [26]. Furthermore, substrate-molecule interactions would reduce the surface tension of the growth units and hence will lower the activation energy for nucleation, allowing the crystallization to occur in that conditions which would not be adequate for spontaneous nucleation [13]; This effect is termed heterogeneous nucleation, the process by which the surface of a foreign material lowers the nucleation barrier and facilitate aggregation in that conditions which would not be adequate for spontaneous (homogeneous) nucleation [27].
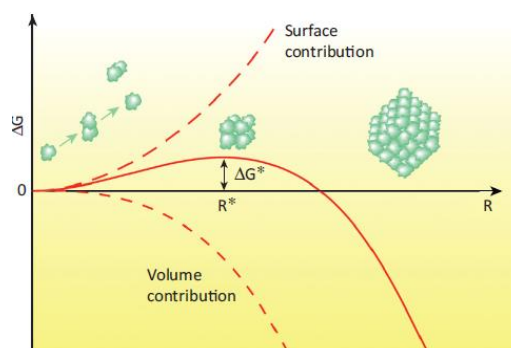
Figure 6 The energy barrier for nucleation. Gibbs free energy for crystallization (ΔG) as a function of the aggregate size (R), shown as an unbroken line. Contributions of surface formation and bulk incorporation are represented by broken lines. R* and ΔG* represent the size of the critical nucleus and the activation free energy (i.e., the energy barrier) for nucleation, respectively [26]

A first reason for the attractiveness of heterogeneous nucleation for crystal growers is that nucleation induced at lower degree of supersaturation can occur inside the metastable zone. Because growth in the metastable zone affords kinetic advantages that often lead to the production of larger and better-ordered crystals than those grown at higher supersaturation, an aim of crystallizers is the possibility to induce heterogeneous nucleation in a controlled manner. In a membrane crystallizer, the crystallizing solution is in direct contact with the membrane surface, and the membrane provides the solid support to promote heterogeneous nucleation mechanism in addition to good control of the supersaturation rate by solvent removal through its porous structure. This effect can be due to both the structural and chemical properties of the membrane surface. The porous membrane can supply cavities where solutes are physically entrapped leading, locally, to high super saturation values suitable for nucleation and also the interaction between the membrane and solute can allow to concentrate and orient molecules on the surface, thus facilitating effective interaction for crystallization [14]. Membrane surface promotes heterogeneous nucleation not only by lowering energy of aggregating but also by structural matching driven by specific polymer molecules interfacial interaction per a mechanism analogue to epitaxial growth. Capability of polymorph selection, kinetically driven by the preferential aggregation of molecules along specific crystalline facets, corroborates these assumptions [28]

1.3.4.   Operational Configurations

The specific mechanisms for mass transport depends on the operational configuration of the membrane crystallizer. Two configurations exist: (i) Solvent evaporation membrane crystallizer where solvent is removed in vapor phase under the gradient of temperature or concentration and (ii) Anti-solvent membrane crystallizer which an anti-solvent is dosed inside the crystallizing solution by means of membrane and the mass transfer occurs by evaporation as well. In Solvent evaporation membrane crystallizer configuration, the distillate side of the membrane consists in a condensing fluid (often the pure solvent) at a lower temperature than the feed side in the case of thermal activation of the driving force, or in a stripping solution consisting in a hypertonic solution of inert salts ($NaCl$, $MgCl_2$, $CaCl_2$, etc.) in the case of the isothermal configuration. The gradient of chemical potential between the two sides of the membrane induces

the evaporation of the solvent at the first interface on the feed side, then the migration of the solvent in vapor phase through the porous membrane and finally, its condensation at the second interface on the distillate side. The continuous removal of solvent from the feed solutions increases solute concentration thus generating supersaturation. Like other membrane process, the temperature and concentration polarization leads the temperature and concentration at the membrane surface to differ from the bulk temperature measured in the feed and in the distillate. Both concentration and temperature polarization nearby the membrane surface might affect locally the degree of supersaturation, so that the mechanism of crystallization can develop in a different way with respect to the bulk of the solution. The highly concentrated region near the porous membrane interface is an ideal nucleation promoting circumstance in the crystallization process. Accordingly, the properties of the crystal nucleated and grown on/near the membrane might display characteristics features that can be controlled by modulating the heat and mass profiles adjacent to the membrane. While in the case of inorganic substances or low molecular weight organic compounds, the thermal system can be affectively used, for the heat-sensitive molecules, like proteins, the osmotic configuration appears more appropriate because of its milder operating conditions. In the antisolvent membrane configuration, two configurations exist: (a) solvent/ antisolvent demixing configuration and antisolvent addition configuration. In the solvent/antisolvent demixing configuration, a solute is dissolved in an appropriate mix of a solvent and antisolvent. Under a gradient of chemical potential which is generated by temperature difference between both sides of the membrane, the solvent evaporates at higher flow rate. As the amount of solvent decreases, supersaturation is created. This configuration requires that the solvent and the antisolvent are miscible, the solvent evaporate at higher rate than the antisolvent and the initial solvent/antisolvent balance in the mixture guarantees that the solute is under its solubility limit. In antisolvent addition configuration, a solute is dissolved in a solvent and under a gradient of chemical potential, an antisolvent is gradually evaporated from other side of the membrane. The antisolvent mix with the solvent, then the solute dilute. At the certain time, the excess of antisolvent creates supersaturation. For this configuration is also required that the solvent and the antisolvent are miscible. In this study, the employed membrane configuration is solvent evaporation membrane crystallizer [5].

1.4. Membranes for Membrane Contactor

The membranes for membrane contactor application must be porous, generally hydrophobic, with good thermal stability and excellent chemical resistance to feed solutions. One of the most crucial aspects of the membrane distillation and membrane crystallization process is to have at disposal membranes with well controlled properties. Moreover, the final performance of a process is a direct consequence of the structural and physicochemical properties of the membranes. In this regards, development of well-structured and functionalized membranes becomes an imperative [2, 4]. Traditionally, the membranes prepared for ultrafiltration and microfiltration through phase inversion processes have been utilized for membrane contactor applications. These membranes generally have low porosity, limited hydrophobicity, broader pore size distribution and pore size not engineered for MD requirements. Therefore, many studies have been dedicated in the last years to fabricate innovative membranes of highly permeable and more selective membranes with low fouling and wetting aptitude for MD applications [5, 29, 30]. In addition, in MCr application, because of the role of membrane surface properties on heterogeneous nucleation, and to create a suitable environment that favors nucleation of the solutes, surface functionalization becomes more important. Therefore, since performances of membranes also depend on the properties of their surfaces, much attention has been paid to the membrane surface modification as an alternative method to improve the performance of membranes. In general, the major aim of surface modification is improving the performance of the membranes with a view to altering a wide range of characteristics of the surface, such as roughness, surface charge, hydrophilicity/hydrophobicity, biocompatibility, and functionality without changing the bulk properties of the membranes. In this respect, the combination of functional materials and membranes as a support might offer beneficial synergisms that endow the resulting composite membranes with entirely novel separation functions for membrane contactor, compared to the commercial membranes [31]. In this work, functional hydrogel materials were studied and selected to fabricate and develop the novel composite membranes with proper properties for application in membrane distillation and membrane crystallization processes.

1.5. Hydrogel Composite Membranes

Nowadays, hydrogel materials have attracted vast attention because of their novel properties and high potential as functional materials. Hydrogels are defined as porous cross linked polymeric structures capable to swell in water and adjust their dimensions and some other properties such as water content, porosity, and capacity to retain or release substances entrapped between the chains, according to the surrounding environment [32, 33]. Principally, these materials have three-dimensional network with ionic or covalent cross links, and hydrogen bonding and van der Waals forces can also act as cross links. In general, the cohesive forces are not only due to covalent bonds (chemical hydrogels) but can also be related to electrostatic forces or dipole-dipole links (physical hydrogels). However, it is important to consider that the swelling/deswelling behavior of hydrogels depends on the nature of the polymer, the polymer-solvent compatibility and the degree of crosslinking [34]. Volume phase transition is a peculiar phenomenon observed with these materials (Figure 7). At the transition, the volume of a hydrogel changes discontinuously in response to continuous changes in surrounding conditions such as temperature, pH, electric or magnetic fields, light and solvent [35-39].
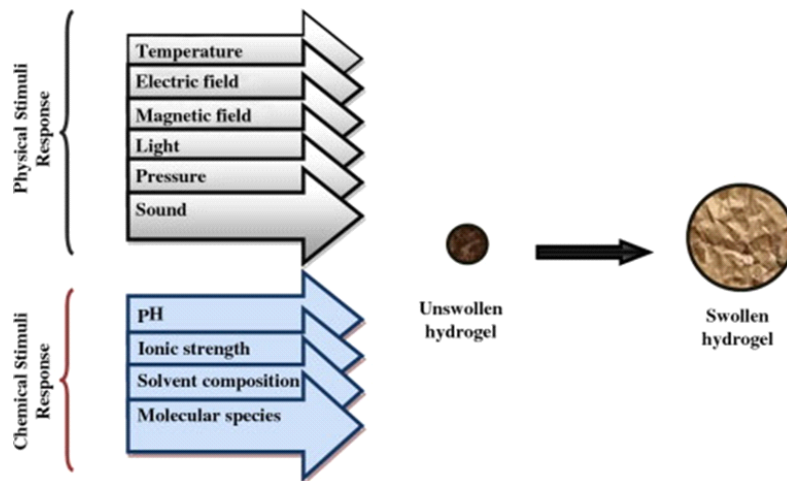
Figure 7 Volume phase transition in response to changes in surrounding conditions such as temperature, electric or magnetic fields, light, pH, solvent composition etc. [36]

Since the volume phase transition brings about dramatic changes in physical properties of the gel, this effect is expected to be applied to the preparation of switching functional materials.

Because of this specific feature, the fabrication and study of novel hydrogel have been intense because of their promise and use in a different branch of science and engineering [40]. Furthermore, hydrogel materials due to their tunable physical and chemical properties and versatility in fabrication, have recently emerged as advanced materials in the field of separation and membrane processes. The separation function of these hydrogel arises from two important features, the 3D network of hydrogels having a tunable mesh size in nanometer range and thus imposing exclusion of molecules based on size or charge [41, 42] and stimuli responsive behavior that can have an additional impact on the separation when sieving is adjusted using external stimuli. Transport through hydrogels, especially under convective flow condition is only possible when the gel is stabilized by a solid support to maintain its integrity. Consequently, hydrogels intended for separation applications should be fabricated in a suited format in order to control swelling without compression under convective flow and with ease of handling. One promising approach is combination of hydrogels and porous membranes as support that leads to composites structures. This is primarily achieved through the synthesis of a hydrogel either inside the pores of a support, thus obtaining a pore-filling composite or on the outer surface of a support, resulting in a thin-film composite membrane [31]. In this sense, hydrogel used in hybrid materials, would provide striking potentialities to accomplish advanced separation because of multi-scale and hierarchical porous structure that is achievable by the hydrogel/support composites synergism. As a hydrogel is simply a hydrophilic polymeric network cross-linked, it can be prepared by any polymerization technique which can be used to create a cross-linked polymer, including bulk solution and suspension polymerization. In general, the three integral parts of the hydrogels preparation are monomer, initiator and cross linker as shown in Figure 8.
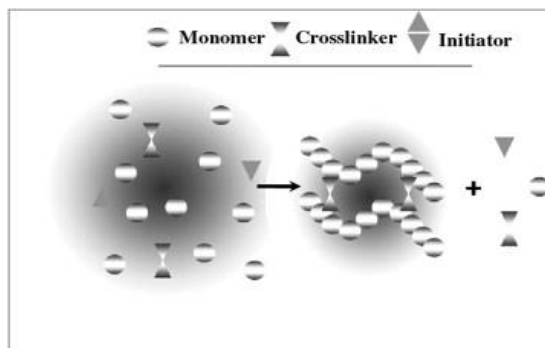
Figure 8 Three integral parts of the hydrogels preparation [35]

To control the heat of polymerization and the final hydrogels properties, diluents can be used, such as water or other aqueous solutions. The structural diversity of the hydrogels is based on the use of a wide range of synthetic monomers, but biopolymers or their derivatives can also be applied. To date, different techniques have been established for incorporation of hydrogel materials into porous membranes, i.e. various surface grafting methods, pore filling and combination thereof as shown in Figure 9.
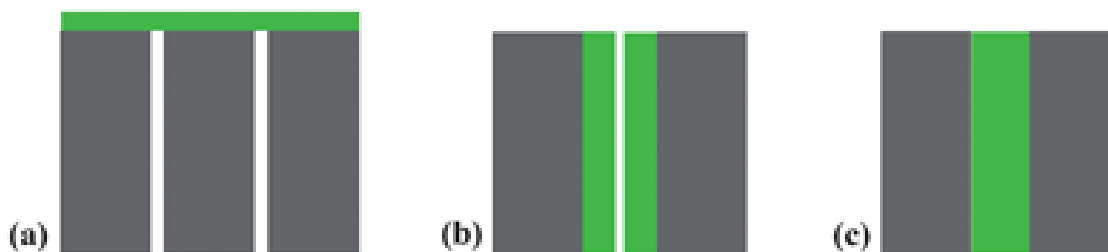
Figure 9 Schematic illustration of different types of (a, b) pore-surface functionalization and (c) pore-filling [31]

In surface grafting method, monomers are polymerized via initiation of the membrane surface and for initiation of the polymerization reaction, different methods can be used such as plasma treatment, high energy irradiation, redox initiation and UV irradiation. Among these methods, UV initiated grafting of hydrogel onto a micro or macro porous support has a much interest due to low cost of operation, mild reaction conditions, and potential for reducing or even avoiding negative effects onto the bulk polymer [43-45]. Composite hydrogel membranes have been prepared by different methods for ultrafiltration (UF) [46-48], nanofiltration (NF) [49, 50], reverse osmosis (RO) [51], and pervaporation (PV) [52] in liquid separations, with significant improvements in either selectivity and/or permeability. The only use of hydrogel composites in membrane distillation is related to the covering of commercial Teflon membranes by with a pre-formed agarose hydrogel layers with the aim to mitigate wetting effects in surfactants and dyeing wastewaters treatment which has been recently reported [53].

Chapter II:

Development of Hydrogel Composite Membranes
Preparation and Characterization

2.1. Polyelectrolyte Hydrogel Composite Membranes with Stimuli Responsive Behavior

2.1.1. Introduction

Hydrogels are three-dimensional network of polymer chains which are physically and/or chemically cross-linked. Generally, they are soft, flexible, with low surface friction and can absorb and retain large amount of water without dissolution [33]. Because of their permeable structure with not-well-defined pores, hydrogels can play separation functions by imposing exclusion based on molecular size [41, 42]. As they can be designed to adapt their swelling state in response to externally applied stimuli, such as temperature [35, 36], pH and ionic strength [37], electric or magnetic fields [38, 54], light [39], and interaction with specifics molecules [55, 56], additional control over separation mechanism is achievable under specific conditions. Furthermore, polyelectrolyte hydrogel layer can be attained using a charged/polarizable monomer and/or cross-linker in the hydrogel synthesis, so that, more than steric hindrance effects, transport selectivity would be driven by the electrical charge features of the gel network as well [57, 58]. Transport through hydrogels, especially under convective flow condition is only possible when the hydrogel is stabilized by a solid support so that it can maintain its integrity. Consequently, hydrogels intended for separation applications should be fabricated in a suited format to control their swelling/shrinking, without compression under convective flow, and to be easy to handle. One promising approach is the combination of hydrogel materials and porous membranes used as support [31]. When such hydrogel materials are supported on the porous membranes (due to enhance their mechanical properties), novel functional membranes with adjustable functionalities compared to the virgin membrane or bulk hydrogel are obtained. These hydrogel-based hybrid materials could provide novel potentialities to accomplish advanced separations thank to the synergistic combination between the hydrogel and the support [59]. Since the stimuli responsive changes in membrane properties will depend primary on the barrier itself, a change in the swelling/shrinking of the barrier leads to changes in permeability and selectivity. In this study, we prepared various polyelectrolyte hydrogel composite membranes (HCMs) directly synthesized on the surface of porous polypropylene (PP) and polyether sulfone (PES) flat sheet membranes using UV initiated graft polymerization technique. Commercial PP and PES membranes were chosen as support material due to high porosity, excellent chemical and mechanical stability, also their accessibility. Acrylic acid (AA), metacrylic acid (MAA) and 2-hydroxyethylmethacrylate

17

(HEMA) used as functional monomers, provide carboxyl (-COOH) and hydroxyl (-OH) groups. In particular, in our experiments, we have selected these functional monomers, because the presence of ionizable groups and their potential for preparing pH and ionic strength sensitive hydrogel system has been reported [60]. Moreover, formation of these hydrogel layer on the polymeric membranes is also possible. Ethylene glycol dimethacrylate (EGDMA) and Polyethylene glycol dimethacrylate (PEGDMA) were used as cross-linkers. Changes in the molar ratio between monomer(s) and cross-linker in the hydrogel synthesis, allowed modulating the ratio of hydrophilic to hydrophobic segments and the density of functional groups (the overall dissociation degree and charge density) in the polyelectrolyte hydrogel network. The resulting composite membranes were characterized by electron scanning microscopy, surface chemistry analysis (FTIR-ATR spectrometer), water contact angle, and ion exchange capacity and swelling degree measurements. As a result, a self-sustaining composite material with multi-scale porous structure, containing hydrogel mesh size in the nanometers range and porous support with pore size in the order of few hundreds of nanometers were obtained. These polyelectrolyte hydrogels displayed a volume phase transition property in response to the salt solution as stimulus as well. This responsive behaviour is related to the presence of hydroxyl and carboxyl groups in the hydrogel networks which causes to swelling/shrinking behaviour of them in response to the salt solution. Potential applications of such hydrogel composite membranes in membrane distillation as gating device because of the ionic strength-responsive behavior of the gel layer to obtain higher water flux, higher solute rejection and long-term stability and also in biomimetic synthesis of $CaCO_3$ superstructures because of the favorable interaction of the acidic groups with molecules of solute to control the crystal morphology are discussed in the chapter Ш.

2.1.2. Materials

Two commercial membranes: polypropylene flat sheet membranes (Accurel PP 2E HF, and poly ether sulfone (PES) flat sheet membranes (Micro PES 2F) were purchased from Membrana GmbH (Wuppertal, Germany). Acrylic acid (AA, monomer, cod.101302902), metacrylic acid (MAA, monomer, cod. 155721), 2-hydroxyethylmethacrylate (HEMA, monomer, cod.101095911), ethyleneglycoldimethacrylate (EGDMA, cross-linker, cod.1012880077), polyethylene glycol dimethacrylate (PEGDMA, average Mn. 750 Da, cross-linker, cod. 437468), 2-hydroxy-2-methyl propiophenone (photoinitiator, cod.1001451059), were obtained from Sigma Aldrich. The molecular structure of the monomers is shown in Figure 10. Sodium chloride (cod.131659.1211) was from Panreac (Nova Chimica, taly) and methanol was from Sigma Aldrich. All chemicals were used as received and water purified with a Milli-Q system was used for all experiments.
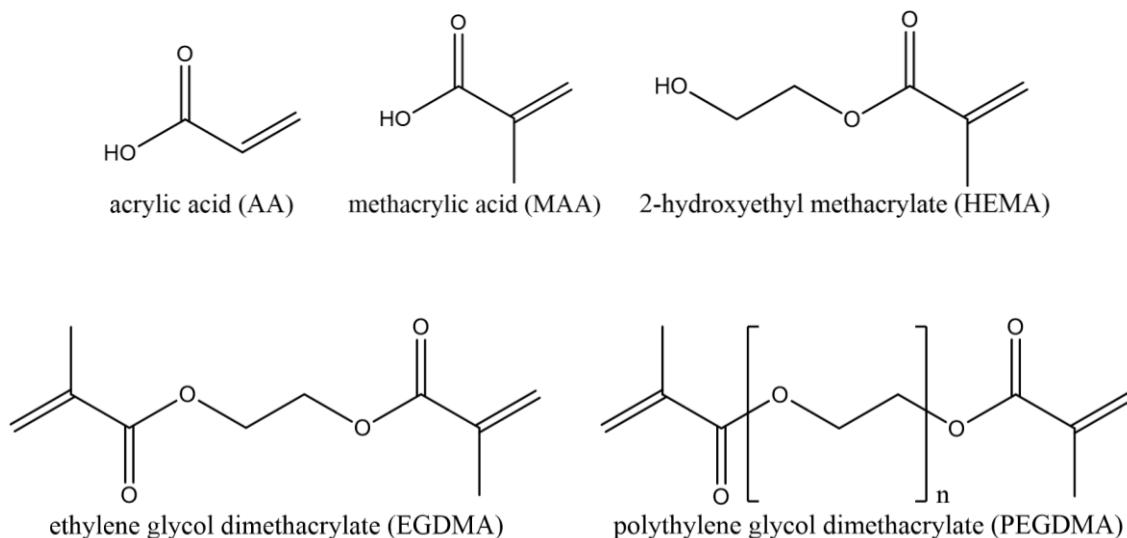
Figure 10 The different monomers (AA, MAA and HEMA) and cross-linkers (EGDMA and PEGDMA) used in this work to fabricate hydrogel composite membranes

2.1.3. Hydrogel composite membranes preparation

The polypropylene and the polyether sulfone membranes were conditioned by soaking in methanol and pure water respectively for 24 h at room temperature. Thereafter, the samples were taken out and dried between tissue paper before use. The hydrogel solutions (pre-polymerization solutions) were prepared by dissolving the accurate amount of monomer(s) in a known amount of pure water, followed by adding the cross-linker and the photo-initiator respectively. The compositions of the monomer solutions used for this study are listed in Table 1.

Table 1 Composition of the monomer solutions for preparation of HCMs

Monomer I	Monomer II	Monomer molar ratio	Cross-linker/amount	Support
AA	-		EGDMA,1 wt. % / PEGDMA,3 wt.%	PP/ PES
AA	HEMA	1:1	EGDMA, 1 wt.%	PP/ PES
AA	HEMA	1:2	EGDMA, 1 wt.%	PP/ PES
AA	HEMA	1:3	EGDMA, 1 wt.%	PP/ PES
AA	HEMA	1:4	EGDMA,1 wt. % / PEGDMA,3 wt.%	PP/ PES
AA	HEMA	1:5	EGDMA, 1 wt.%	PP/ PES
MAA	-		EGDMA,1 wt. % / PEGDMA,3 wt.%	PP/ PES
MAA	HEMA	1:4	EGDMA,1 wt. % / PEGDMA,3 wt.%	PP/ PES
HEMA	-		EGDMA,1 wt. % / PEGDMA,3 wt.%	PP/ PES

The solutions were magnetically stirred until complete dissolution and then free standing hydrogel were prepared from the reaction mixtures. The solute concentration was gradually increased to achieve stable and manageable gels. The solution then was cast onto the PP and PES membranes by rolling on the loaded support with a bar coater at 100 µm thickness. Photo-initiated graft polymerization was carried out under an UV/Vis irradiation lamp (GR. E. 500W) in a vented exposition chamber (Helios Italquartz, Italy), for 5 min. Experimental set up is shown in Figure 11.
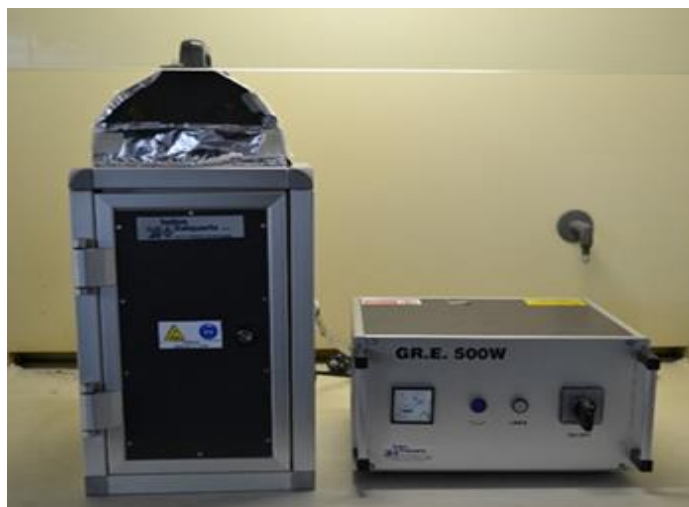
Figure 11 Experimental set up: UV/Vis irradiation lamp placed on the vented exposition chamber

Thereafter, the prepared hydrogel composite membranes were washed and stored in a large excess of distilled water at room temperature for further characterization and experiments. Schematic illustration of the preparation procedure of HCMs is shown in Figure 12.
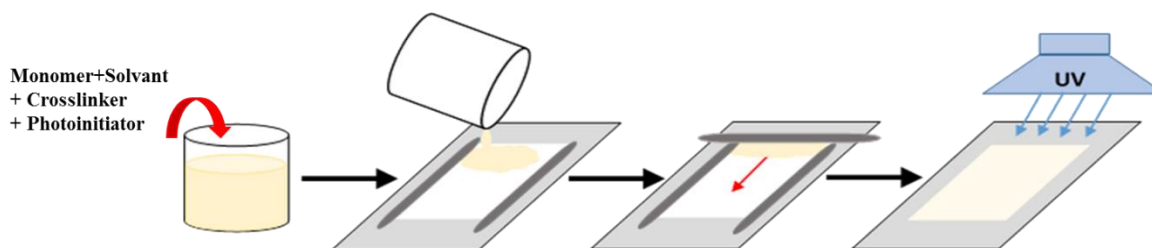
Figure 12 Preparation of hydrogel composite membranes: 1) Pre-conditioning of membranes, 2) Preparing of hydrogel solutions, 3) Casting a thin layer of hydrogel solution, 4) Polymerization of the solution under the UV lamp

2.1.4. Hydrogel Composite Membrane Characterization

2.1.4.1. Surface morphology analysis

Morphological analysis (top and cross section) of hydrogel composites was performed by a Quanta 200F FEI Philips scanning electron microscope (SEM). Samples were cut and attached

with carbon conductive double side tape to steal stubs, and then sputtered with chromium or gold prior to SEM analysis. The accelerating voltage during analyses was 12.0–15.0 kV under high vacuum conditions. To examine cross section, samples were cryo-fractures with liquid nitrogen.

2.1.4.2. Contact angle measurements

Static contact angle of water and NaCl solutions at different concentration (1-30 g L^{-1}) on hydrogel composite membranes was measured with a goniometer (Nordtest) at ambient temperature. A drop (2 µL) of solution was put onto the sample surface by a micro-syringe and measurements were carried out by setting the tangents on both visible edges of the droplet, on five different positions of each sample; the average value of the measurements was reported.

2.1.4.3. Surface chemistry analysis

Chemical surface analysis of membranes was performed by Fourier transform infrared spectroscopy (Nicolet iS10 FT-IR spectrometer, from Thermo Scientific, USA). Spectra were recorded using ATR (Attenuated Total Reflectance) technique in the range of 650 to 4000 cm^{-1} with a resolution of 1 cm^{-1} and averaged over 30 scans.

2.1.4.4. Swelling degree measurements (SD)

Hydrogel composite membranes were cut into 3×3 cm^2 squares and immersed in vials (15 mL) filled with distilled water or NaCl solutions in the range of 1-30 g L^{-1}, under controlled temperature conditions. After 24 h, they are weighed after removing the excess surface solution with tissue paper and then dried in an oven at 40 °C for 24 h. The swelling degree of the hydrogel is determined gravimetrically by the following equation:

$$S.D. = 100 \times \frac{m - m_0}{m_0} \tag{5}$$

Where m_0 and m are the dry and swollen sample weight, respectively. Calculations were performed by considering the weight of the support. Tests were also performed on bulk hydrogel (without support) synthetized in petri dishes, to check the different swelling/shrinking behavior of free bulky and anchored hydrogel layers.

2.1.4.5. Ion exchange capacity (IEC)

Hydrogel composite membranes were cut into 3×3 cm^2 squares and immersed in 0.5 M NaCl solution for 24 h to have the gel in the Na$^+$ form. Then they were washed with distilled water and immersed in 25 mL of 0.01 M HCl solution for 24 h. Thereafter, composites were removed and the exchanged solution was titrated with 0.1 M NaOH until neutrality. IEC is defined as the number of moles exchanged per gram of dry sample, and calculated using the following equation:

$$IEC = \frac{moles \cdot H^+ \cdot exchanged}{m_0} \tag{6}$$

With m_0 the dry weight of the samples. The reported values were the mean of at least three measurements.

2.1.5. Results and Discussion

Surface morphology: Hydrogel composite membranes were successfully prepared (see Table 2) with a uniform and defect-free thin hydrogel layer synthetized directly on the surface of the polypropylene porous membrane. A representative SEM image of a HCM supported on PP is shown in Figure 13; and it displays a 20 μm thick gel layer on the top of the PP support membrane (170 μm thick). The cross-section image reveals that the hydrogel phase does not penetrate in to the porous PP due to the hydrophobic nature of the support membrane. Developed hydrogel composite membranes have demonstrated good mechanical stability against delamination under static and convective flow conditions. Delamination was not observed even when leaving composites in water for more than three months. The conditioning step of the support before the gel synthesis is found crucial to obtain mechanically stable hydrogel composites. Furthermore, methanol-filled pores of PP are prevented to be flooded by the hydrogel solutions during the casting and the photo-polymerization stages, so that no penetrating gel layer is obtained.
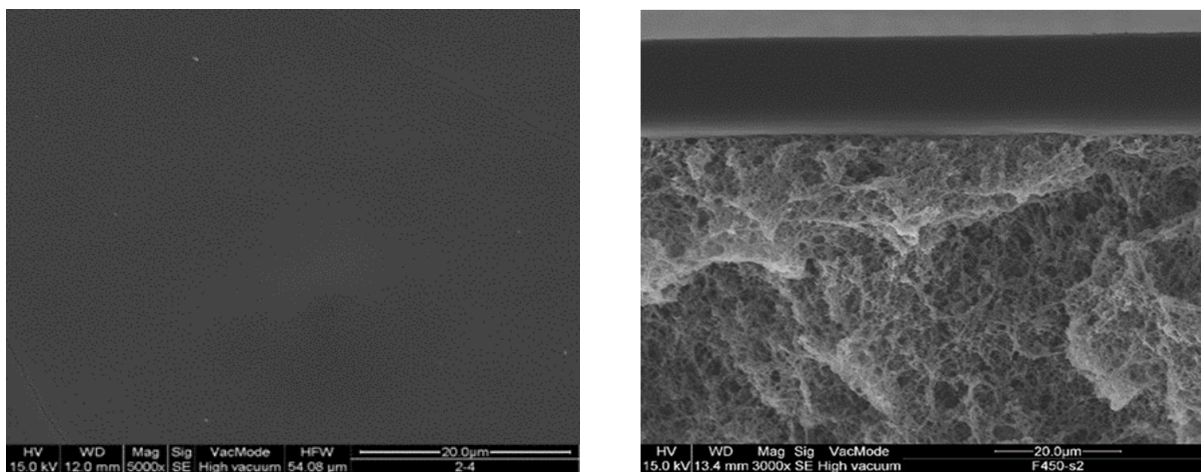
Figure 13 Characteristic SEM image of the top and cross section of AA-co-HEMA sample: A dense, uniform and defect-free hydrogel layer adheres to the surface of the porous PP support

In the case of PES membranes, it was difficult to obtain the homogenous gel layer because of the penetration of the solution inside the membranes pores due to the hydrophilic nature of the PES membrane (not shown here).

The UV-initiated polymerization reaction for the synthesis of the hydrogel layer on the PP support in HCMs: AA-co-HEMA/EGDMA has been shown in Figure 14.
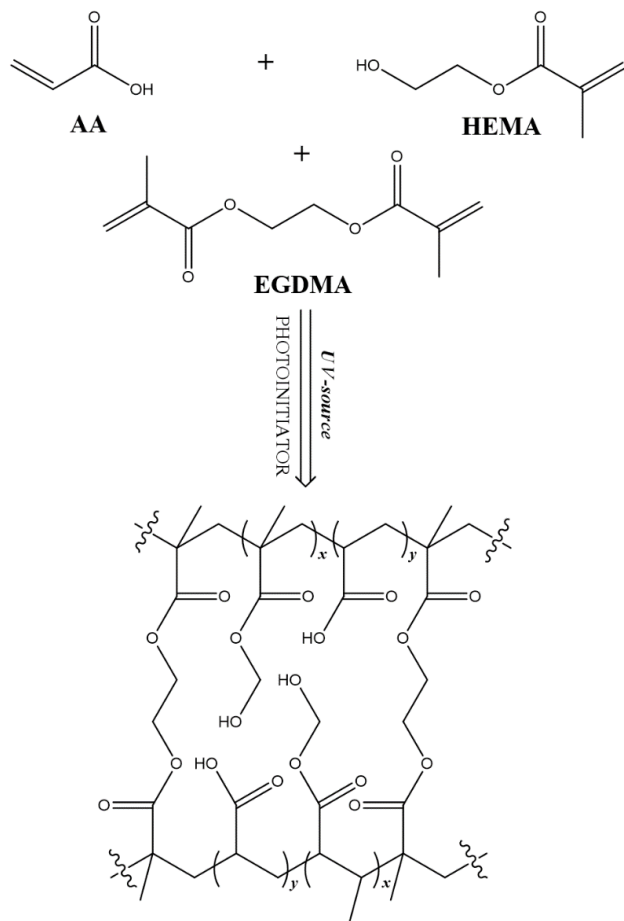
Figure 14 UV-initiated polymerization reaction for the synthesis of the hydrogel layer on the PP support: AA /HEMA/EGDMA

Water contact angle: The water contact angle was obviously decreased in the case of PP membranes. The water contact angle for virgin PP membrane was 137° and after modification, decreased in the range of 38-54° for HCMs. By increasing the amount of HEMA in the composite hydrogel, the water angle contact decreases as shown in the Table 2. The same trend for NaCl solution with different concentrations was observed as well.

Figure 15 Contact angle of Water for (a) virgin PP membrane and (b) hydrogel composite membranes

Table 2 Hydrogel composite membrane samples and corresponding contact angles with different solutions

Membrane sample code	AA/HEMA molar ratio	Contact angle			
		Water	NaCl 1 g/l	NaCl 10 g/l	NaCl 30 g/l
PP	-	137±1	138±1	137±1	136±1
AA-HEMA 1-1	1:1	54±1	53±2	53±2	50±1
AA-HEMA 1-2	1:2	52±1	51±1	51±1	49±1
AA-HEMA 1-3	1:3	44±1	44±1	43±2	42±1
AA-HEMA 1-4	1:4	43±2	43±1	42±2	40±1
AA-HEMA 1-5	1:5	43±3	42±1	42±1	40±1
HEMA	-	38±1	37±1	37±1	35±1

In the case of HCMs supported on PES membranes, the water contact angles were significantly lower and the water droplet penetrate deeply into the bulk and completely wet the membranes. By increasing the amount of HEMA in the composite hydrogel, there was no significant change in the water contact angle. The water contact angles were around 30˚ as the same with the virgin membrane ($\theta =28˚$).

Surface chemistry: Typical ATR-FTIR spectra of unmodified PP membrane and hydrogel composites has been shown in Figure 16 a. Unmodified PP membrane showed the characteristics peaks around 2945 cm^{-1} due to the C-H stretching and 1455 and 1380 cm^{-1} due to −CH deformation modes. After modification with the hydrogel layer, a new peak appears at 1718 cm^{-1} due to the C=O stretching vibration of the carboxylic groups. Since the strong absorption band at 1718 cm^{-1} in the spectrum of modified membranes is absent in the PP spectrum, the ratio of the intensity of the absorption band at 1718 cm^{-1} (A_{1718}) to the intensity of the absorption band at 2945 cm^{-1} (A_{2945}) was used as indicative of the composition of the sample. As it can be seen in Figure 14, the absorption bands ratio A_{1718}/A_{2945} is sensitive to the AA composition of the systems and it decreased when the concentration of AA decreased in the mixture. This trend indicates that the proportion of AA in the hydrogels decreased from AA hydrogel to HEMA hydrogel, as expected from the monomer composition.

Unmodified PES membrane displayed the characteristics peaks at 1577 cm^{-1} which is assigned to the aromatic ring in PES, and disappeared in the modified membranes spectra (not shown here). The second marked peak at carbonyl group at 1718 cm^{-1} is the characteristic band of the group of carboxylic acid of the functional monomer which is not present in the PES spectra. The ratio of the intensity of the absorption band at 1718 cm^{-1} to the intensity of the absorption band at 1577 cm^{-1} was used as indicative of the composition of the sample. The ratio A_{1718}/A_{1577} is sensitive to the AA composition of the systems and it decreased when the concentration of AA decreased in the mixture.
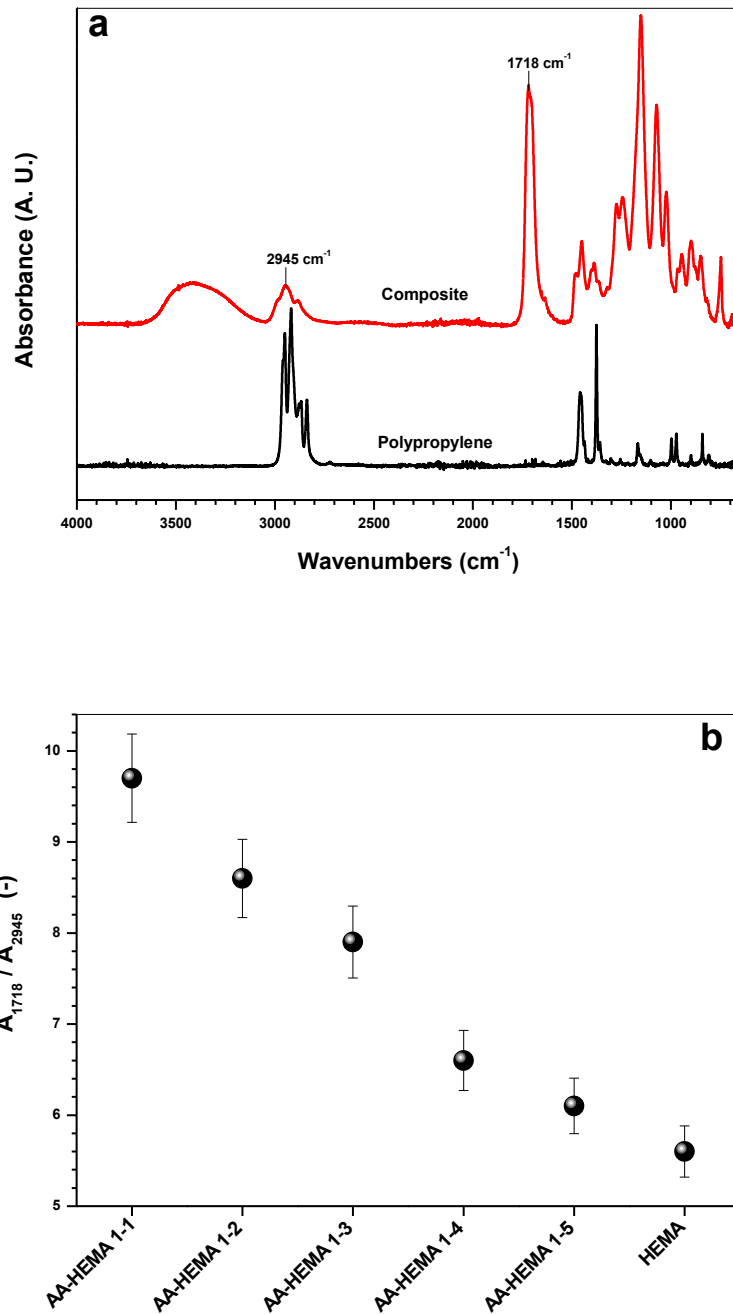
Figure 16 (a) Typical ATR-FTIR spectra of unmodified PP membrane and hydrogel composites. (b) Dependence of the FT-IR absorption signals ratio at 1718 and 2945 cm^{-1} (A_{1718}/A_{2945}) from the amount of AA (and carboxyl groups) in the hydrogel network structure

Swelling degree and ion exchange capacity: Ion exchange capacity and water swelling are among the most parameters for polyelectrolyte hydrogels. They are determined by nature of polymer matrix, number of changed groups, and density of crosslinks and external parameters (e.g. temperature, pH). An increase in ionic group content facilitates better proton exchange and make a membrane more proton conductive. On the other hand, an increase in the number of polar groups makes the membrane more swell able, which also leads to increased mobility of ions in the membrane. Acrylic acid and 2-hydroxyethyl methacrylate provide ionizable carboxylic and hydroxyl groups respectively (Figure 10). The ionic-strength-responsive behavior of the developed composites provides the unique opportunity to control over mass transport and ion retention of the composite membranes. The enhanced charge density in the hydrogel network with increasing AA/HEMA molar ratio is confirmed by the higher ion exchange capacity and a greater swelling degree as it is shown in Figure 17. Swelling degree of bulk hydrogels and composites in pure Water and NaCl solution at different concentration is shown in Figure 17 a. Shrinking/deswelling of poly AA-co-HEMA composites with NaCl solutions compared to pure water is in agreement to a polyelectrolyte behavior in the selected range of salt concentration (1-30 g L^{-1}). In the opportune range of NaCl concentrations, the addition of mobile counter ions (Na^+) to polyelectrolytes screens the repulsive electrostatic interactions of fixed anionic groups in the hydrogel network and simultaneously, leads to a substantial drop in solvent affinity of salt solution and deswelling of the hydrogel. The general reduction of water uptake by increasing NaCl concentration is observed as well because of increasing of mobile counter ions (Na^+) in the solution.
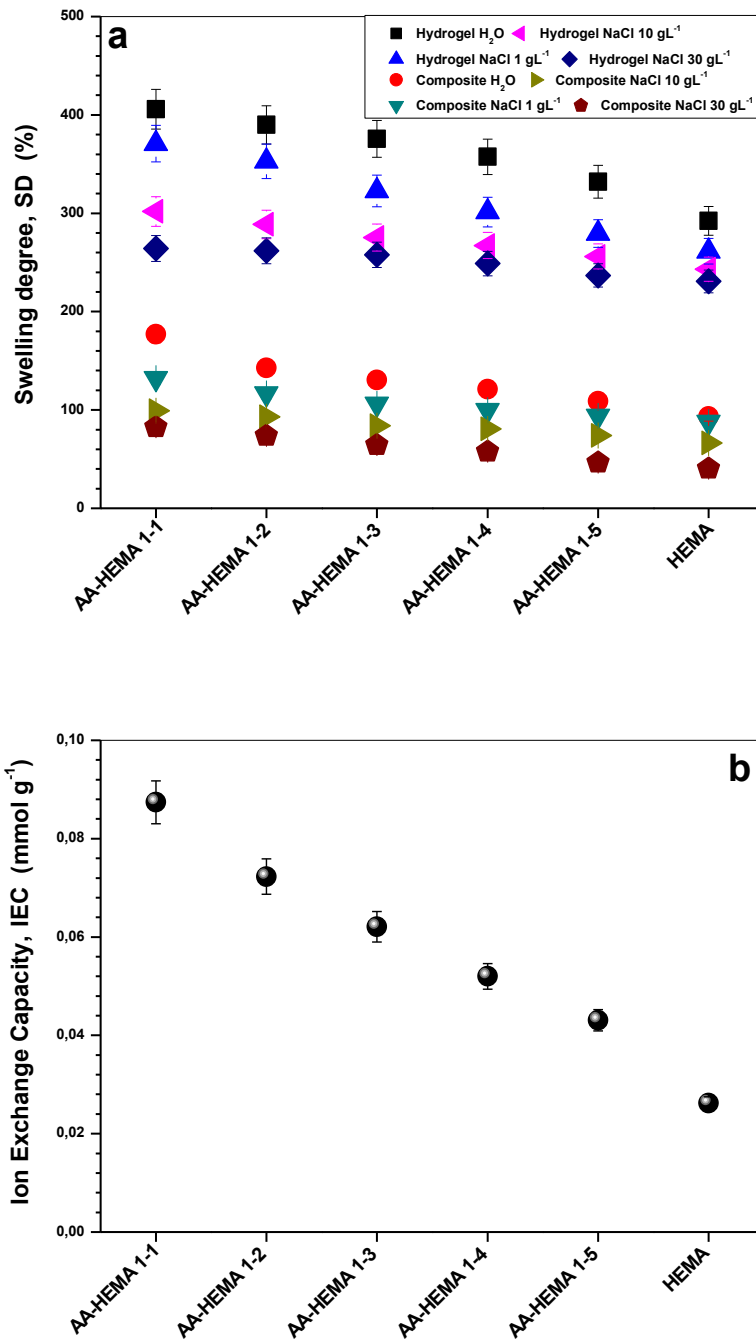
Figure 17 (a) Swelling degree SD of bulk-free hydrogel and gel layer in HCMs at 20 °C in pure water and different NaCl solutions. (b) Ion exchange capacity IEC of HCMs at 20 °C.

Stimuli responsive behavior of HCMs: The singular behavior of HCMs in response to the salt solution concentration is explained by the chemical nature of the soft hydrogel phase and its synergistic interaction with the solid hydrophobic PP support. AA and HEMA contain ionizable carboxylic and hydroxyl groups, respectively. In the excess of water, they dissociate giving rise to fixed anionic portions attracting water molecules, thus providing the swelling of the hydrogel. The addition of mobile counter-ions (Na^+) in the opportune range of concentrations screens the repulsive electrostatic interactions among fixed groups [61, 62] and, at the same time, leads to a substantial drop in solvent affinity in the salt solution compared to pure water and deswelling (shrinking) of the hydrogel [63]. The hydrogel microstructure strongly depends on its hydration level which is related to the density and dissociation degree of ionizable groups in its network and to the external electrolyte solution activity, that affects the strength of electrostatic interactions among polymeric chains through salt ions [64, 65]. This kind of response of the hydrogel to the ion concentration in the interacting solution and its relation to the chemical features of the gel layer, offers additional possibilities in regulating salt rejection and mass transport in composites. Collapse of the gel layer in poly AA- co-HEMA composites with NaCl solutions in the selected range of salt concentration is observed (Figure 17 a) and confirms this assumption. The general reduction of wate ruptake by increasing the concentration of NaCl was found for both bulk free hydrogel and gel layer incomposites, with the notable difference of the lower swelling degree of the latter for all compositions. This is because the gels anchored to the supportare predominantly characterized by uniaxial swelling/shrinking in the direction perpendicular to thesubstrate [66, 67], leading to strong anisotropic deformation in response to the salt solution.

2.1.6. Conclusions

Various polyelectrolyte hydrogel composite membranes were prepared by using UV initiated polymerization of functional monomers and cross-linkers on the surface of commercial PP and PES flat sheet membranes and then characterized by different techniques. Developed composites membranes demonstrated good mechanical stability under static and convective flow conditions. Changing the molar ratio between monomers in hydrogel synthesis allowed dosing the overall dissociation degree and fixed charge density in polyelectrolyte hydrogel network, thus

influencing the local distribution of mobile ions at the interface with the interacting solution. The enhanced charge density in the hydrogel network with increasing AA/HEMA molar ratio was confirmed by the higher ion exchange capacity which results in an increased concentration of mobile ions in the hydrogel phase, and a greater water uptake (swelling degree) due to their osmotic pressure. The ionic-strength-responsive behavior of the developed composites provides the unique opportunity to control over mass transport and ion retention of the composites. Potential applications of such hydrogel composite membranes in membrane distillation as gating device and in biomineral crystallization, as suitable microenvironment for biomimetic synthesis of $CaCO_3$ superstructures are described in the chapter III.

2.2. Hydrogel Composite Membranes Incorporating Iron Oxide Nanoparticles

2.2.1. Introduction

There is increasing interest in developing solid templates (hetronucleants) suitable to promote and control nucleation and crystal growth especially in the field of the crystallization of biological macromolecules. The search for suitable materials which can induce and control nucleation of proteins has been investigated, and different approaches have been proposed to promote and control nucleation to obtain crystals with high quality. These approaches have studied the influence of surface morphology, porosity, surface chemistry, and surface roughness. Several porous solid materials e.g. porous silicon, mesoporous gold and porous glasses with a distribution of pore sizes and shapes, have been reported to be successful templates for crystallizing different proteins [68-70]. In contrast to the rigid materials with nanoscopic pores, soft templates have also recently been used to crystallize proteins. In this regards, polymer surfaces with porosity and surface functionality has been well advanced [11, 14], and more recently the use of molecularly imprinted polymers (MIPs) have also been reported [71]. Hydrogel materials are a class of soft materials which can mimic the native microenvironment of proteins due to their porous and hydrated molecular structure. The incorporation of nanomaterials within polymeric hydrogels represents an attractive approach to tailor the mechanical properties of the hydrogels and/or to provide the hydrogel composite with responsiveness to mechanical, thermal, magnetic, and electric stimuli. In this study, with the aim to study the effect of surface energy and topography on protein crystallization, we developed and designed hydrogel composites by incorporating nanoparticles. Iron oxide nanoparticles (NPs) were used as topographical designers providing a good control of membrane surface roughness and patterning. The functional composite membranes prepared in this study, were constituted by a polyvinyl alcohol (PVA) hydrogel layer with embedded iron oxide nanoparticles, supported on a microporous polypropylene membrane. PVA is an attractive hydrogel material because of its higher hydrophilic and film forming capacity. The presence of many hydroxyl group, makes the membrane surface too polar. By crosslinking PVA, it is possible for one to decrease the hydrogel hydrophilicity and provide a suitable network to entrap proteins. Here, we investigated the crosslinking of PVA by glutaraldehyde (GA) and poly (ethylene glycol) diglycidyl ether (PEDGE). The composite membranes were prepared by coating of hydrogel layer using simple casting method. The morphology and topography of the membrane surfaces were

characterized using electron scanning microscopy (SEM), surface chemistry analysis (FTIR-ATR spectrometer and profilometry analysis. The dynamic contact angles glycerol at the surface of these functional composite membranes determined in a sessile mode using a drop shape analyzer system coupled to a video camera connected to a PC for data acquisition and the determination of the CA along time using the CAM100 software. Thereafter, the composite membranes were tested as heterogeneous nucleation support for protein crystallization and their performance in protein crystallization was evaluated. The results are discussed in Chapter III.

.

2.2.2. Materials

Commercial polypropylene flat sheet membrane (Accurel PP 2EHF, nominal pore size 200 nm, overall porosity 70%) were purchased from Membrana GmbH (Wuppertal, Germany). Polyvinyl alcohol (PVA, average Mw = 150,000 g/mol; 98.9% hydrolyzed, cod. 101302902), Glutaraldehyde (GA, grade II, 25% in H_2O, cross-linker, Lot# MKBG3597V), Poly (ethylene glycol) diglycidyl ether (PEDGE, average Mw = 500 g/mol, cross-linker, Lot# MKBL8500V), Iron oxide nanoparticles (average size of 7.403 ± 0.154 nm) were prepared with chemical precipitation technique [72]. The molecular structure of the monomers is shown in Figure 18. Ferric chloride hexahydrate (97% $FeCl_3 \cdot 6H_2O$) and ferrous chloride tetra hydrate (99% $FeCl_2 \cdot 4H_2O$), and potassium oleate (40 wt% paste in water, $CH_3 (CH_2)_7 CH=CH (CH_2)_7 COOK$, were from Sigma Aldrich. Ammonium hydroxide (NH4OH, Mallinckrodt) and Hitenol–BC (Daiichi KogyoSeiyaki) and ammonium persulfate (>98% $(NH_4)_2S_2O_8$ was from Sigma-Aldrich. Methanol and Hydrochloric acid were from Sigma Aldrich. All chemicals were used as received and water purified with a Milli-Q system was used for all experiments.

Polyvinyl alcohol (PVA)   Glutaraldehyde (GA)   Poly(ethylene glycol) diglycidyl ether (PEDGE)
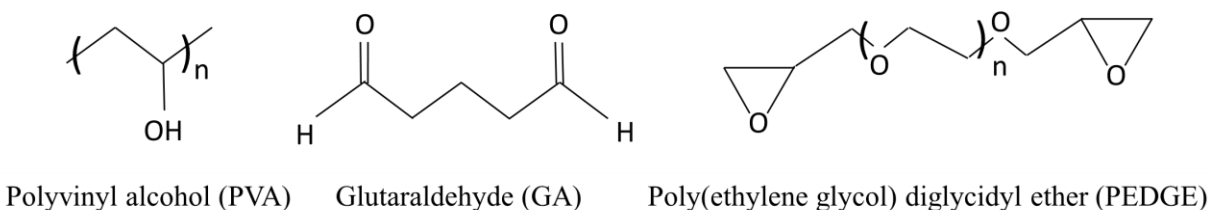
Figure 18 Molecular structures of the polymer rand the cross-linkers used in this work to fabricate hydrogel composite membranes

2.2.3. Synthesis of the Iron Oxide Nanoparticles

The synthesis of the iron oxide nanoparticles (Fe_2O_3) by chemical precipitation technique was based on the procedure described by Bernat Olle [72]. The particles were produced by precipitation of iron salts in alkaline medium under nitrogen atmosphere to prevent oxidation of the particles. Iron salts solutions were prepared, $FeCl_3.6H_2O$ (94.4 g), $FeCl_2.4H_2O$ (34.4 g) in aqueous solution (100 mL of distilled water) and added to a preheated oil bath at 80 °C under

constant magnetic stirring (1250 rpm) for 30 minutes. Potassium oleate then was added to ensure the coating of the particles, pending about 30 minutes to ensure the dissolution of the polymer. 100 mL of aqueous ammonia (25%) was added gradually to the mixture by pumping, under stirring for 30 minutes. Two stabilizers were also added: Hitenol- CB (100 g) and ammonium persulfate (5 g). The solution was stirred for 30 min to allow the formation of covalent bonds between hitenol groups and oleic acid. This synthetic procedure yielded iron oxide nanoparticles with an average size of 7.403 ± 0.154 nm.

2.2.4. Preparation of Hydrogel Composite Membranes Containing Iron Oxide NPs

PVA solutions (8 % w/v) were prepared by dissolving appropriate amounts of PVA in distilled water with heating (at around 80 °C) and constant stirring for 3 h. A calculated amount of iron oxide nanoparticles (Table 3) was added to PVA solution to make solutions of 0.25 wt. %, 0.5 wt. % and 1 wt. %.

Table 3 Hydrogel composite membrane samples

Membrane samples	Polymer Concentration (w/v)	Cross linker (Type/amount)	Nanoparticles (amount)
PVA-PEDGE-NPs 0 %	PVA 8 %	PEDGE 3 wt. %	-
PVA-PEDGE-NPs 0.25 %	PVA 8 %	PEDGE 3 wt. %	Iron oxide III, 0.25 wt.%
PVA-PEDGE-NPs 0.5%	PVA 8 %	PEDGE 3 wt. %	Iron oxide III, 0.5 wt.%
PVA-PEDGE-NPs 1 %	PVA 8 %	PEDGE 3 wt. %	Iron oxide III, 1 wt.%
PVA-GA-NPs 0 %	PVA 8 %	GA 3 wt. %	-
PVA-GA-NPs 0.25 %	PVA 8 %	GA 3 wt. %	Iron oxide III, 0.25 wt.%
PVA-GA-NPs 0.5 %	PVA 8 %	GA 3 wt. %	Iron oxide III, 0.5 wt.%
PVA-GA-NPs 1 %	PVA 8 %	GA 3 wt. %	Iron oxide III, 1 wt.%

To obtain good dispersion of nanoparticles, ultra-sonication was employed for 30 min immediately prior to the crosslinking reaction. Then the cross linker and 0.1 M hydrochloric acid (used as a catalyst) solution were added. To initiate the coating process, the surface of the PP support was conditioned by soaking in Methanol to increase the adhesion between the hydrophobic PP surface and the hydrophilic coating. Then hydrogel solution was cast on the membrane surface using a film applicator (Electrometer 4340, automatic film applicator) adjusted at 50 µm thickness. The experimental set up is shown in Figure 19.

Figure 19 Casting with the automatic film applicator adjusted at 50 µm thickness

Thereafter, the prepared hydrogel composite membranes were washed with distilled water and stored at room temperature for further characterization and experiments. Schematic illustration of the preparation procedure of HCMs is shown in Figure 20.
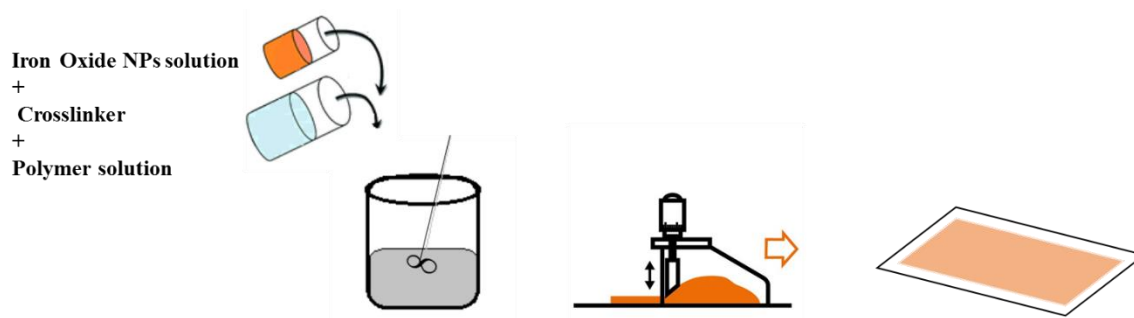
Figure 20 Preparation of hydrogel composite membranes: 1) Pre-conditioning of membranes, 2) Preparing of hydrogel solutions, 3) Casting a thin layer of hydrogel solution, 4) Crosslinking reaction

37

In the case of Glutaraldehyde, the reaction was carried out at room temperature under acidic conditions (HCl 0.1 M). Since the reaction is very fast, hydrogel layer was formed after a few minutes and the time was not enough to assure a good physisorption of the gel layer into the porous support, i.e. to guarantee a good entrapment of the gel solution into the porous structure of the support. In consequence, the resulting gel layer formed on the surface membrane was peeled off easily by hand. Pretreatment of PP membranes by soaking in methanol overnight, resulted in a good adherence of hydrogel layer to the support. In the case of poly (ethylene glycol) diglycidyl ether, the reaction was carried out in the oven at 30 °C for a few hours. Therefore, in this case the gel entrapment into the porous support was successful, resulting in the formation of a structurally stable composite membrane. Composite membranes with distinct structural inorganic anisotropies were prepared either with randomly dispersed particles or with aligned particles. Composite membranes with isotropic inorganic structure were obtained by random dispersion of the nanoparticles in to the gel top layer whereas anisotropic inorganic structures were achieved by with the magnetic induced alignment of the nanoparticles. Particle alignment was possible by applying a uniform magnetic field with a magnitude of 0.5 T parallel to the membrane surface (with the cast hydrogel layer) during crosslinking reaction.

2.2.5. Characterization of Hydrogel Composite Membranes

2.2.5.1. Optical microscopy

Hydrogel composite membranes with randomly dispersed or aligned Iron oxide NPs were observed using an optical microscope (DM 2500M, Leica Microsystems, Germany).

2.2.5.2. Surface morphology analysis

The samples were coated with an Au/Pd film of 20 nm thickness using a sputter coater from Quorum Technologies, model Q150TES and were analysed in a FEG-SEM system from JEOL, model JSM7001F equipped with a coupled EDS detector with light energies from Oxford, model INCA 250.

2.2.5.3. Surface chemistry analysis

Chemical surface analysis of membranes was performed by Fourier transform infrared spectroscopy (Nicolet iS10 FT-IR spectrometer, from Thermo Scientific, USA). Spectra were recorded using ATR (Attenuated Total Reflectance) technique in the range of 650 to 4000 cm^{-1} with a resolution of 1 cm^{-1} and averaged over 30 scans.

2.2.5.4. Contact angle measurements

The values of the contact angle of Glycerol on composite membranes were measured using CAM 101- Optical contact angle and surface tension meter (KSV Instruments Ltd, Helsinki, Finland) at room temperature. A small drop (2 µL) of the solution was placed on the sample surface by a micro syringe and measurements were carried immediately. The contact angle values reported are the averages of five consecutive measurements for each sample.

2.2.5.5. Surface roughness measurements

Surface roughness profiles were measured by DEKTAK Profilometer (Figure 21) using a 5 µm radius tip with 1 mg stylus load and at the velocity of 0.1 mm/s. The scanner sizes were 0.5 × 0.5 mm^2. A diamond stylus is moved vertically in contact with a sample and moved later across the sample for specified distance and contact force. The height position of the stylus generates an analogue signal which is converted into the digital signal stored, analysed and displayed. The average roughness, defined as the arithmetic average of the absolute values of the surface height deviation measured from the mean plane surface and the root-mean-square (rms) roughness, defined as the standard deviation of the surface profile from the mean plane surface, were calculated by Nanoscope software. The average value of three measurements is reported.
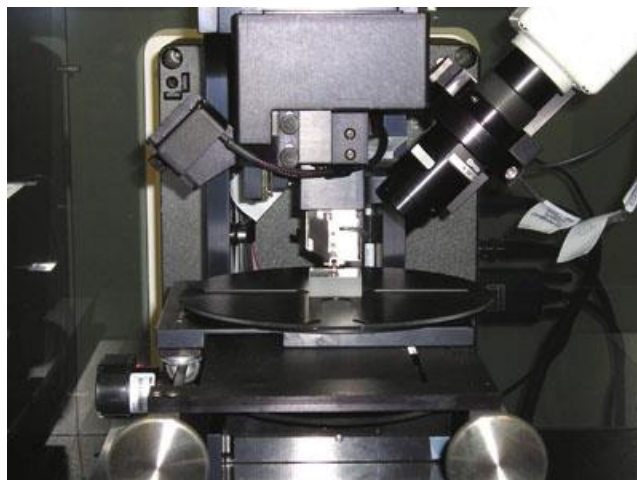
Figure 21 DEKTAK Profilometer

2.2.6. Results and Discussion

A thin layer of PVA hydrogel crosslinked with GA or PEDGE was formed on the surface of PP membrane under catalytic condition. Optical microscopic images of HCMs e.g. PVA-PEDGE-NPs 1% (Figure 22) show the uniform dispersion of disordered and aligned particle (with the magnetic field) and it confirms the possibility of surface patterning of HCMs constituted by a polyvinyl alcohol hydrogel layer with embedded iron oxide nanoparticles, supported on PP membrane by using this technique.
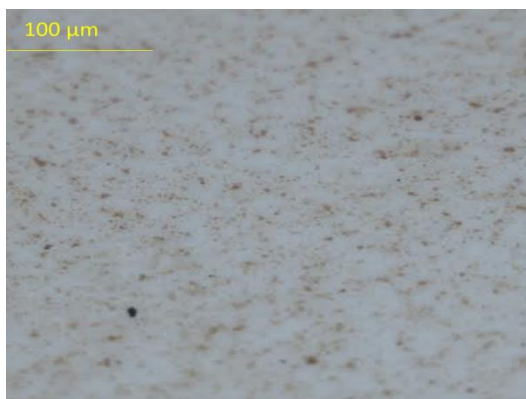
Figure 22 Surface patterning of HCMs constituted by a polyvinyl alcohol hydrogel layer with embedded iron oxide nanoparticles, supported on PP membrane (a) disordered and (b) aligned particles

A representative SEM image of the cryo-fractured cross section of HCM is shown in Figure 23; and it displays a uniform and defect free thin hydrogel layer (10 μm) on the surface of the PP porous membrane (170 μm thick). The cross-section image reveals that the hydrogel phase does not penetrate in to the porous PP due to the hydrophobic nature of the support membrane. Iron oxide particles were detected by EDS on the surface as well as throughout the hydrogel layer (Figure 24).
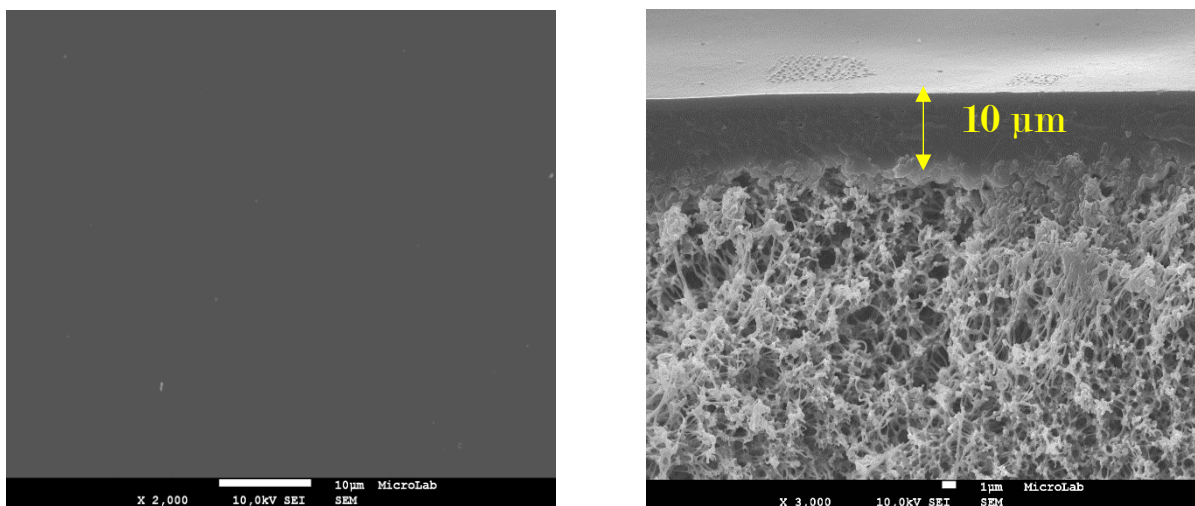
Figure 23 Characteristic SEM image of the top and cross section of PVA-GA-NPs 1% supported on PP sample: A dense, uniform and defect-free hydrogel layer adheres to the surface of the porous PP support
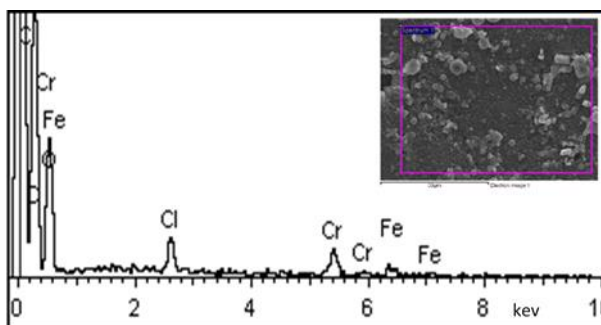
Figure 24 Iron oxide particles detected by EDS on the surface and inside the hydrogel layer

The crosslinking reaction Figure 25 for the synthesis of the hydrogel layer on the PP support in HCMs: PVA crosslinked with PEDGE or GA may be depicted as follows respectively:

(a)
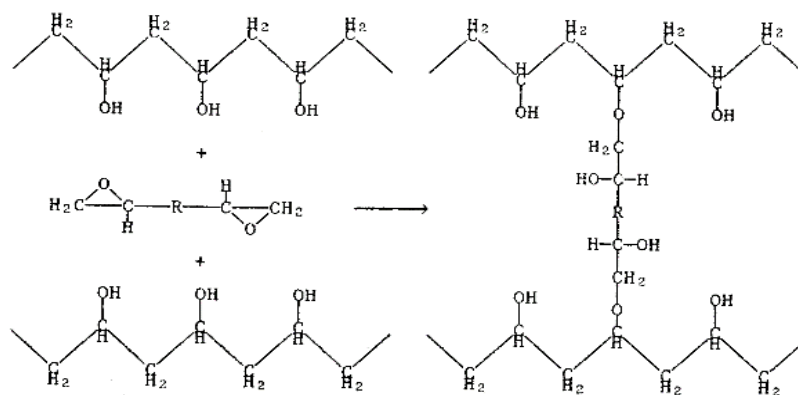
(b)
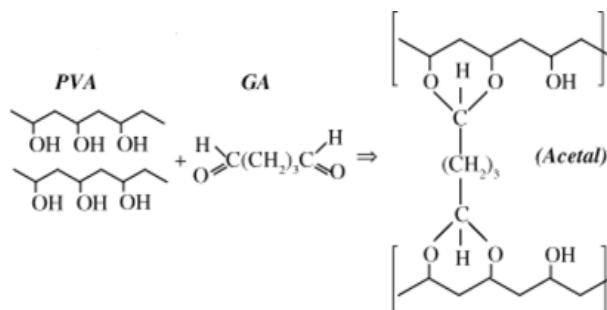
Figure 25 Crosslinking reactions under catalytic condition for (a) PEDGE and (b) GA

In ATR-FTIR spectra of HCMs (Figure 26), the large, broad band observed at 3000−3500 cm^{-1} are associated with the stretching vibration of hydroxyl (−OH) groups. The two vibrational bands observed between 2730 and 2860 cm^{-1} refer to the stretching vibration of C−H from alkyl and O=C−H from the aldehyde corresponding to PVA cross linked by PEDGE or GA which confirms the crosslinking reaction.
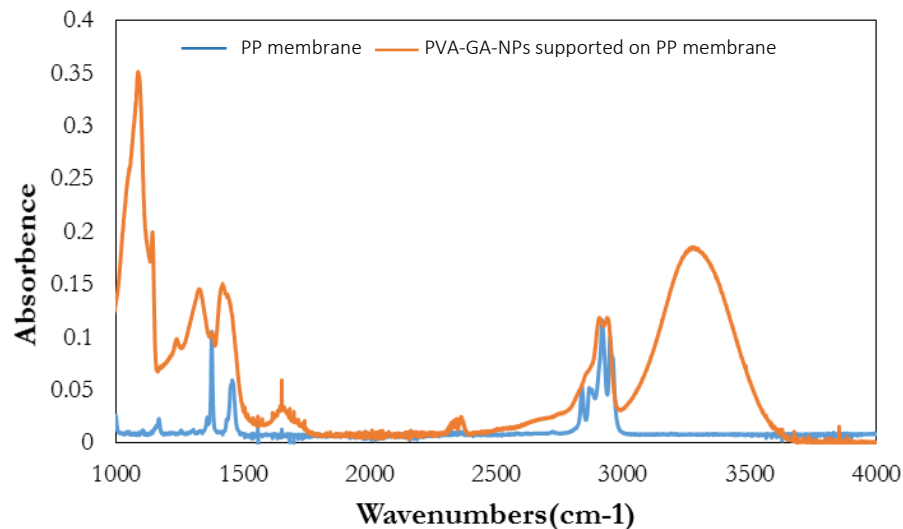
Figure 26 ATR-FTIR spectra of unmodified PP membrane and PVA-GA-NPs supported on PP membrane

The measured contact angles and surface roughness analysis of the prepared HCMs are compared in Table 4. Water contact angle measurements reveal relatively similar values for all PVA hydrogel composite membranes ranging from 42 to 56º, which are much lower than the hydrophobic pristine PP substrate (137º). These values confirm the increase in hydrophilicity from the PVA component and suggest a further slight increase in hydrophilicity upon incorporation of iron oxide nanoparticles. Both root-mean-square (rms) roughness and average roughness (Ra) are used to characterize the surface roughness. An increasing trend of the average roughness and rms values of different surfaces with the amount of NPs is observed. The surface roughness of the HCMs varied from very smooth (Sa = 370 nm) to rather rough (Sa = 1036 nm). According to Wenzel theory [73], hydrophilic surfaces ($\theta < 90º$), with the typical size of roughness details smaller than the size of the interacting droplet and without air pockets, referred to as a homogenous interface with complete wetting, become more hydrophilic with an increase in roughness. According to the reported values in Table 4, increasing the roughness of PVA hydrogel composite membranes by increasing amount of NPs decreased the contact angle (enhanced relatively hydrophilicity) which is in agreement with Wenzel theory.

Table 4 Hydrogel composite membranes and their surface properties

HCM samples	Average roughness(nm)	RMS roughness(nm)	Contact angle
Virgin PP Membrane	3090	3853	137
PVA-PEDGE	301±25	370±20	49±2
PVA-PEDGE- NPs 0.25%-PP	562±63	719±40	45±3
PVA-PEDGE- NPs 1%-PP	811±145	1018±164	43±2
PVA-GA- NPs	361±69	448±90	56±1
PVA-GA- NPs 0.25%-PP	628±111	848±164	50±2
PVA-GA- NPs 1%-PP	821±137	1036±172	48±2

Three-dimensional images of studied surfaces with a scanner size of 0.5×0.5 mm^2 are shown in Figure 27 (a) shows that many hillocks exist on the surfaces of virgin PP membrane. Figure 27 (b) and (e) show that the surfaces of HCMs without NPs are relatively smooth. By introducing NPs, there exist a few plateaus and eddies on the hydrogel surface, which results in larger values of roughness (Figure 27 c, d, f, g). Experimental evidence demonstrated that the roughness of the HCMs can be manipulated by changing the amount of NPs in the hydrogel matrix.
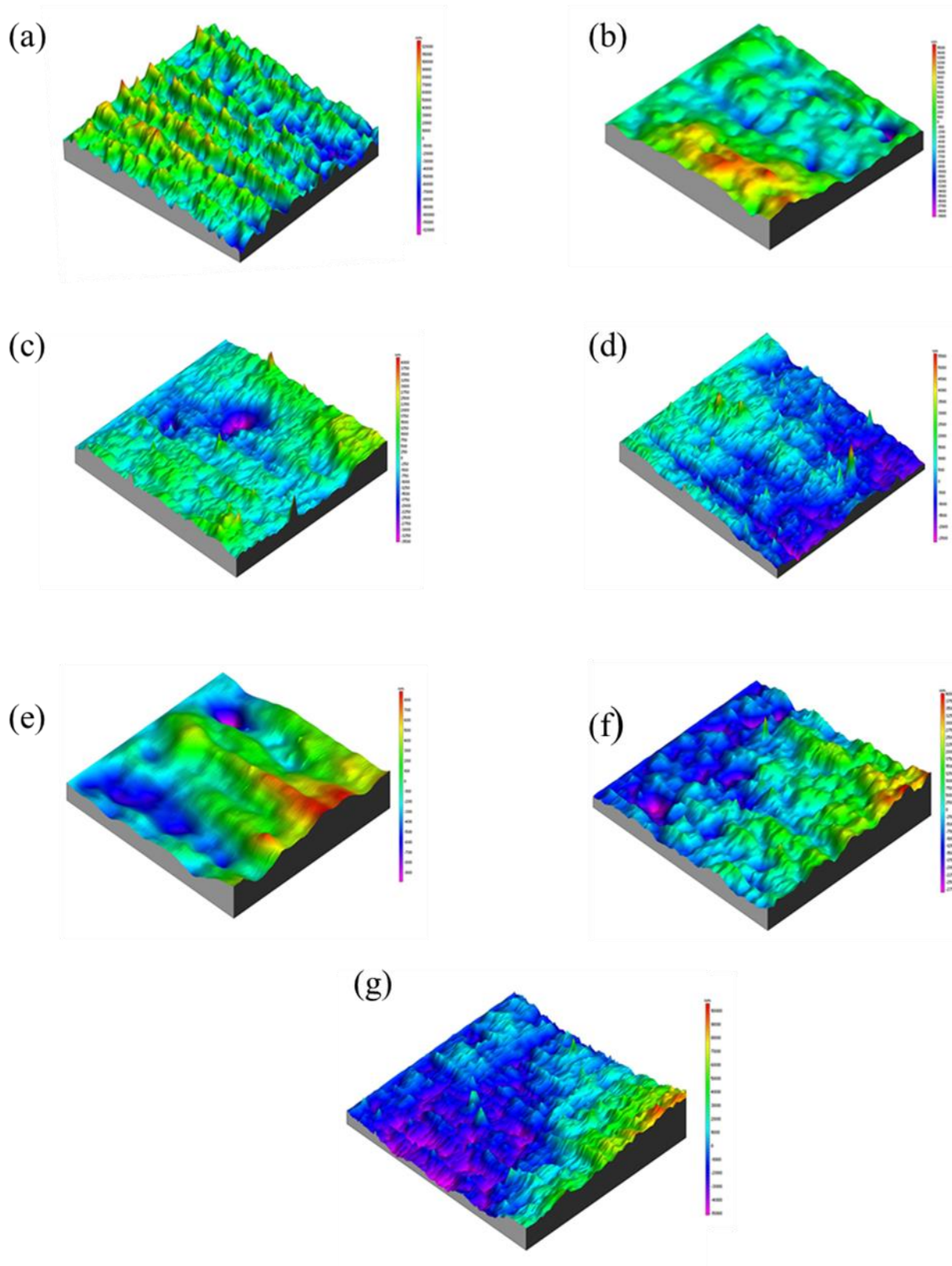
Figure 27 Three-dimensional images of studied surfaces a) PP membrane, b) PVA-PEDGE, c) PVA-PEDGE-NPs 0.25%, d) PVA-PEDGE-NPs 1%, e) PVA-GA, f) PVA-GA-NPs 0.25%, g) PVA-GA-NPs 1%

2.2.7. Conclusions

Functional membranes with tailored surface patterning were designed in attempt to stimulate controlled heterogeneous nucleation while assuring a simultaneous solvent removal in the vapor phase representing a potential application in the field of controlled crystallization processes. The topography of membrane surfaces was adjusted by the amount of nanoparticles within the hydrogel matrix and dispersion quality. We demonstrated that by incorporating the Iron oxide NPs in the polymer matrix, surface roughness and hydrophilicity can be modulated. Water contact angle measurements revealed relatively similar values for all PVA hydrogel composite membranes ranging from 42 to 56º and a further slight increase in hydrophilicity upon incorporation of iron oxide nanoparticles. Also, an increasing trend of the surface roughness of the HCMs with the amount of NPs was observed. The surface roughness of the HCMs varied from very smooth (Sa = 370 nm) to rather rough (Sa = 1036 nm). Since increased surface roughness will positively or negatively affect nucleation induction and density depending on the extent interaction between the crystallizing solution and the surface (wetting properties), in the case of HCMs incorporating NPs (as hydrophilic template) a significant fraction of solute molecules may be likely to accumulate at the solid solution interface and further can concentrate in certain heterogeneous domains by physical entrapment.

Chapter III:

Application of Hydrogel Composite Membranes in Membrane Distillation and Membrane assisted Crystallization Processes

3.1. Membrane Distillation by Stimuli Responsive Hydrogel Composite Membranes

3.1.1. Introduction

Membrane distillation is an emerging thermally driven technology for the recovery of high purity water across a macro porous hydrophobic membrane [74, 75]. Compared to pressurized membrane processes, MD offers a number of potential advantages such as: (i)100% theoretical rejection of non-volatile compounds; (ii) moderately low operating temperatures (50–80 °C); (iii) operation at atmospheric pressure as only tangential solutions circulation is required;(iv) reduced sensitivity to feed concentration; (v) less severe requirement mechanical membrane properties; (vi) large contacting area per volume for mass transfer [76]. Consequently, MD has been receiving increasing attention for sea/brackish-water desalination and wastewater purification [18, 77-79]. However, despite these potential advantages, the wide diffusion of MD technology is still hindered by the unavailability of membranes specifically designed and developed for MD to provide higher flux, enhanced selectivity, and lower fouling tendency than conventionally used membranes. Therefore, many studies have been dedicated in the last years to fabricate innovative MD membranes with increasingly improved performances. Since hydrophobic attraction is the main interaction between protein and membrane in aqueous systems, the most common method to improve antifouling property is the hydrophilization of the membrane surface without compromising membrane wetting resistance. In this regards, several studies have been reported on surface hydrophilization of membrane such as fabrication of dual layer hydrophilic–hydrophobic hollow fiber PVDF membranes, surface hydrophilization of PVDF membranes by plasma and TiO_2 particles deposition, blending PVDF with multi walled carbon nanotubes by the phase inversion method etc. [29, 30, 80, 81]. Besides, another promising approach in this direction is the combination of hydrogel materials and porous membranes used as support [31]. These hydrogel-based hybrid materials could provide novel potentialities to accomplish advanced separations thank to the synergistic combination between the hydrogel and the support [59]. Hydrogel composites display the added advantage of a high-water content in their structure thereby reducing the adsorption of nonspecific binding to the membrane, and thus potentially reducing the effects of fouling. In addition, using a charged/polarizable monomer and/or crosslinker for the hydrogel synthesis (polyelectrolyte hydrogels), a charged layer with a high Donnan potential may be attained, so that transport selectivity would be also associated to the electrical charge properties of

the system. Composite hydrogel membranes have been prepared by different methods for ultrafiltration (UF) [46-48], nanofiltration (NF) [49, 50], reverse osmosis (RO) [51], and pervaporation (PV) [52] in liquid separations, with significant improvements in either selectivity and/or permeability. The only use of hydrogel composites in membrane distillation is related to the covering of commercial Teflon membranes by with a pre-formed agarose hydrogel layers with the aim to mitigate wetting effects in surfactants and dyeing wastewaters treatment which has been recently reported [53]. Here, we developed mechanically stable composites containing a hydrophilic hydrogel layer completely adhered to the hydrophobic support and used as smart gating devices for ion retention and fast water transport in direct contact MD of saline solutions. Acrylic acid (AA) and 2-hydroxyethyl methacrylate (HEMA) were selected as functional monomers. A mixture of acrylic acid and 2-hydroxy-ethyl methacrylate was selected as the building block for ionic strength sensitive hydrogel because such a system has been successfully employed to generate mechanically stable pH and ionic strength sensitive flow control valves on the micrometer scale [60]. Several different compositions of AA and HEMA mixture were chosen to determine possible effects on ionic strength sensitivity. Ethylene glycol dimethacrylate (EGDMA) was used as cross-linking agents in UV-initiated graft polymerization. Polypropylene (PP) flat sheet membranes provided the opportune porous hydrophobic support. The contribution of the polyelectrolyte layer properties, in terms of nature and density of the charged groups at different functional monomers compositions, on the permeability and selectivity of composites in MD treatment of saline solutions was investigated. The presence of ionizable groups make polyelectrolyte hydrogel sensitive to salt ions concentration. The retention property and responsive behavior of hydrogel membranes (swelling/shrinking) to salt solutions, and its dependence on the monomers composition in the gel synthesis, provides the unique opportunity to enhance control over mass transport and selectivity in MD process. The special transport mechanism arises from the synergistic connection between the polyelectrolyte layer and the hydrophobic substrate. Combination of Donnan exclusion effects and the swelling/ shrinking behavior of the hydrogel in response to the salt solution, which leads to strong anisotropic deformation of the soft gel layer anchored to the rigid support, affords tuneable water transport and ion rejection compared to conventional uncharged MD membranes. As a result, enhanced permeability and selectivity of composites, compared to pristine polypropylene membranes, are obtained when using saline solutions as feed.

3.1.2. Materials

Commercial membrane; polypropylene flat sheet membrane was from Membrana GmbH (Wuppertal, Germany), acrylic acid (AA, monomer, cod.101302902), 2-hydroxyethyl methacrylate (HEMA, monomer, cod.101095911), ethylene glycol dimethacrylate (EGDMA, cross-linker, cod.1012880077), 2-hydroxy-2-methylpropiophenone (photo-initiator, cod. 1001451059), were from Sigma Aldrich, sodium chloride (cod.131659.1211) was from Panreac (Nova Chimica), humic acid (HA, cod. 53680) and bovine serum albumin (BSA, cod.05470) were from Sigma Aldrich. All chemicals were used as received and water purified with a Milli-Q system was used for all experiments as condensing fluid on the distillate side in DCMD tests. Hydrogel composite membranes were prepared as described in chapter 2.1.3 and are presented in Table 5.

Table 5 Hydrogel composite membrane samples for membrane distillation test

Sample No.	Sample Cod.	Monomer(s)/Molar ration/Cross-linker/Support
1	AA-HEMA 1-1	AA-HEMA / 1:1 / EDDMA / PP
2	AA-HEMA 1-2	AA-HEMA / 1:2 / EDDMA / PP
3	AA-HEMA 1-3	AA-HEMA / 1:3 / EDDMA / PP
4	AA-HEMA 1-4	AA-HEMA / 1:4 / EDDMA / PP
5	AA-HEMA 1-5	AA-HEMA / 1:5 / EDDMA / PP
6	HEMA	HEMA / EDDMA / PP

3.1.3. Membrane Distillation Test

Hydrogel compote membranes and virgin polypropylene were tested in the direct contact membrane distillation plant shown in Figure 28. Pure water and NaCl solutions at different salt concentrations (1–30 g L^{-1}) were used as feed. The set up used for membrane distillation tests (Figure 29), consisting of a feed reservoir, a distilled reservoir placed on a balance, the membrane distillation module for membrane housing, peristaltic pumps for solutions circulation, heat exchangers to generate the thermal gradient, and electronic controllers. The starting volume of

feed and distilled water were 3 L each. The inlets and outlets of the membrane module were equipped with thermometers, flowmeters, and pressure-meters. The temperature of the warm and the cold solutions were 50 °C and 10 °C, respectively. Solutions were circulated at 18 L h^{-1}. Active membrane area inside the module was 3.5×10^{-3} m^2.
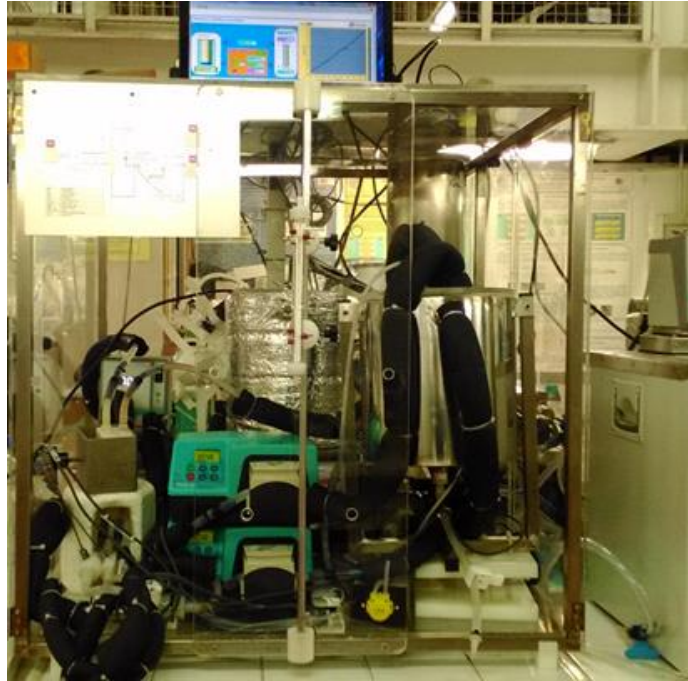
Figure 28 Laboratory plant of direct contact membrane distillation

The rejection of NaCl was determined by an electrical conductivity-meter (Jenway 354-201 pH/conductivity-meter) placed on the cold reservoir. Solute rejection R is defined as:

$$R = \left(1 - \frac{C_{distillate}}{C_{feed}}\right) \times 100 \qquad (7)$$

Where C_{feed} and $C_{distillate}$ are the NaCl concentration in the feed and in the distillate, respectively. $C_{distillate}$ refers to the NaCl concentration in the aliquot of solution that has passed thorough the membrane in the time. It is calculated by measuring the electrical conductivity of the overall distillate volume and, after opportune calibration, by mass balance. Each membrane

distillation test lasted 5 hours. Transmembrane flux J were taken as the average flux in the last hour of operation under steady conditions, and calculated as:

$$J = \frac{M}{\Delta t \cdot A} \tag{8}$$

Where M is the mass of water that has passed through the membrane (as detected by the balance) in the time interval Δt, and A is the effective membrane area.
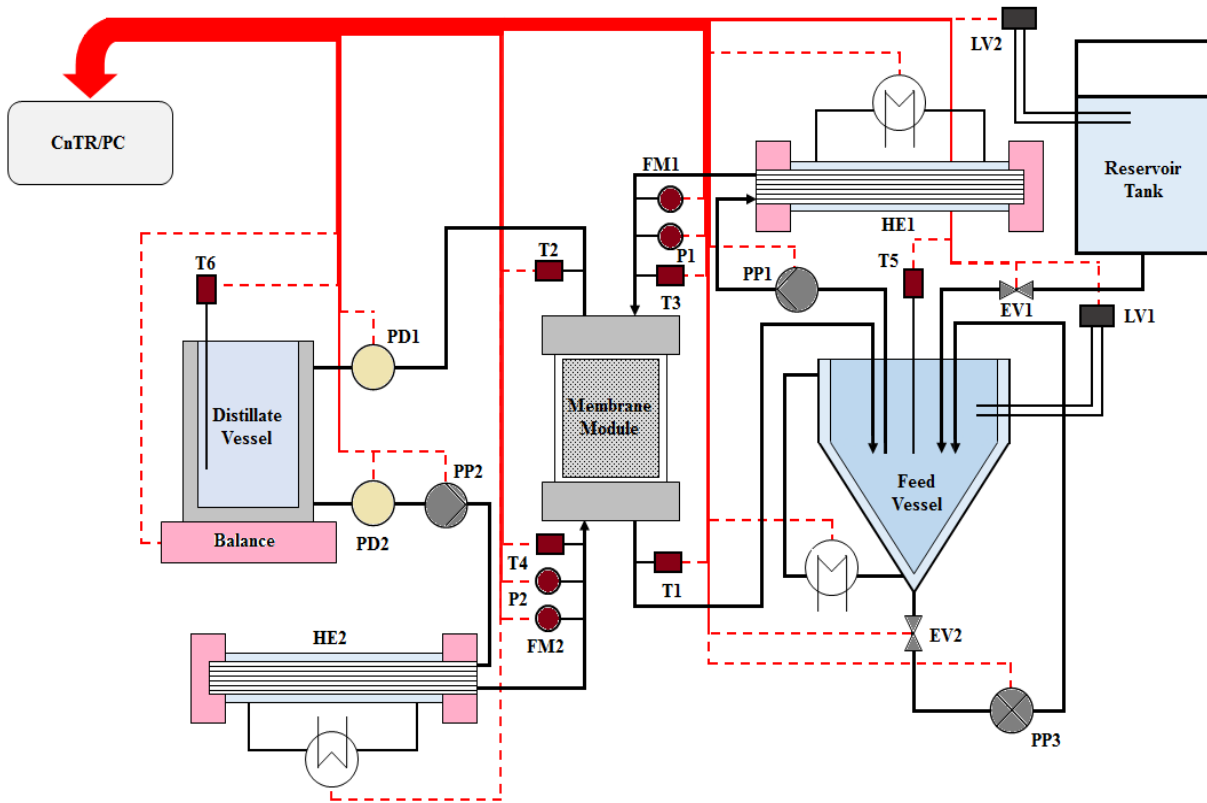
Figure 29 Membrane distillation plant: T1–T6 temperature probes; P1–P2 pressure probes; FM1–FM2 flow-meters; PP1–PP3 peristaltic pumps; EV1–EV2 electro-valves; LV1– LV2 liquid-level probes; HE1–HE2 heat exchangers; PD1–PD2 pulsation dampers; and membrane holder cell (membrane module)

3.1.4. Results and discussion

Figure 30 a, b shows the resulting transmembrane fluxes J and the corresponding salt rejections R for saline solutions. The synthesis of a hydrogel layer on the surface of the support is expected to introduce additional resistance to mass transfer. Therefore, in absence of additional transport mechanism contributes, reduced water transport in MD tests would be observed for hydrogel composites compared to virgin PP membranes. Furthermore, using saline solutions as feed instead of pure water, water vapor pressure drop under the effect of the dissolved solute is commonly observed according to the Raoult's law, and consequently the driving force for mass transfer is reduced [82]. This behavior is observed with bare PP support; which transmembrane flux J is reduced more than 65% with 30 g L^{-1} NaCl solution compared to pure water. Surprisingly, in the case of hydrogel composite membranes, all samples showed enhanced water transport (increase in transmembrane flux J) with NaCl solutions than pure water (Figure 30 a) and the higher water flux is obtained with the higher stating NaCl concentration (Figure 30 b) and there is an asymptotic increasing trend in water flux with increasing NaCl concentration. Figure 30 (a) also reveals that NaCl rejection is somewhat higher for composites (from 98.6% to 99.1% for NaCl 30 gL^{-1} as feed) than PP membrane (98.4%) and the salt retention increases with the amount of AA in the gel structure. Furthermore, salt rejection increases from 99.09% to 99.97% with decreasing the starting NaCl concentration from 30 to1 gL^{-1} (Figure 30 b). On the bases of these results, it appears that although the addition of the hydrogel layer introduces additional resistance to mass transfer to the pristine PP membrane, the presence of ionizable groups in the polyelectrolyte network of HCMs is responsible for the salt concentration dependence of the transmembrane flux and for the enhanced ion retention, which become more important and controllable factors in mass transport and selectivity in the treatment of saline solutions.
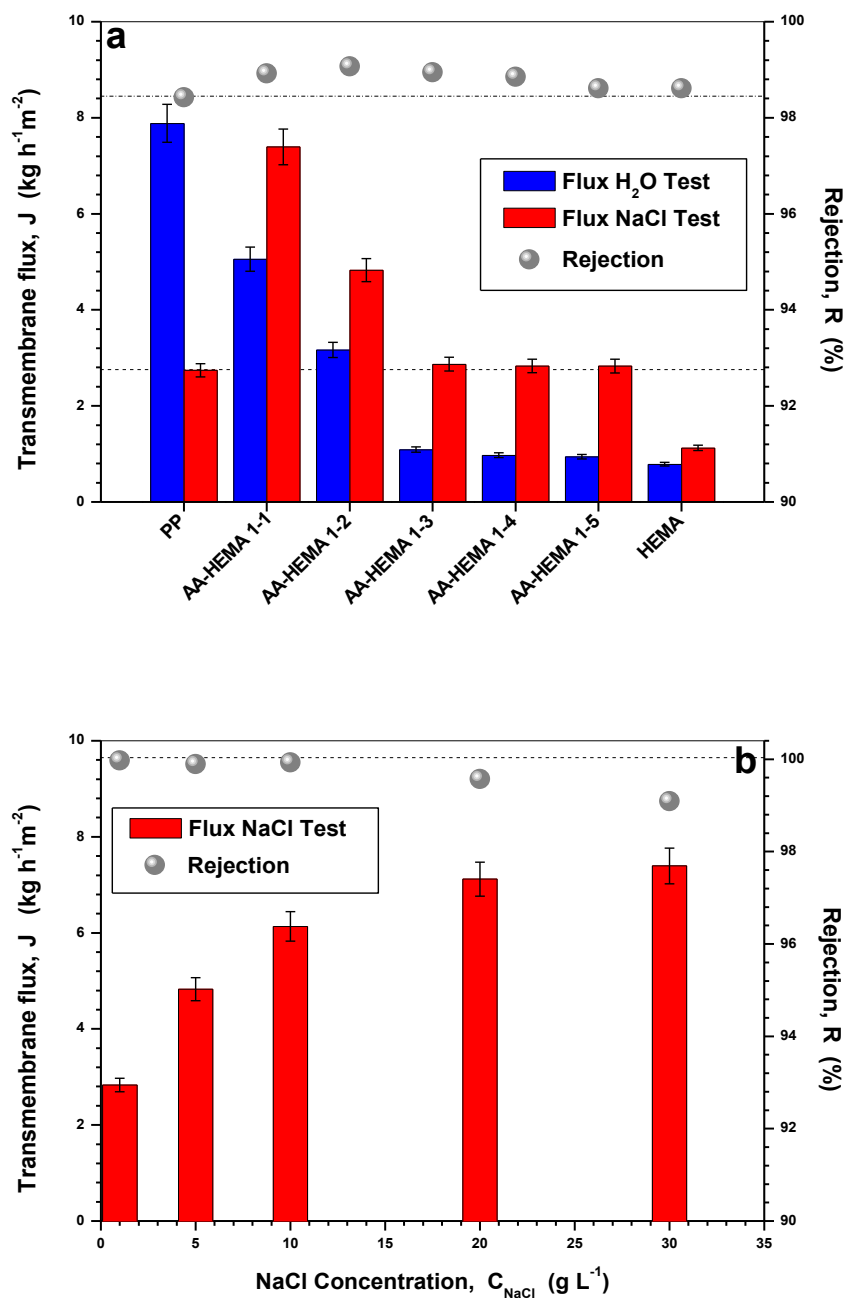
Figure 30 (a) Transmembrane flux J for pure water and NaCl 30 g L-1 solution and related solute rejection R, for virgin PP and composite hydrogel membranes. Horizontal dotted lines are guides for the eyes: they display the average flux with NaCl solution (down) and rejection to NaCl (up) for PP support. (b) Transmembrane flux J for NaCl solutions at different concentration and related solution rejection R, for AA-HEMA 1-1 composite. Horizontal dotted line is a guide for the eyes: it displays 100% rejection to NaCl. Error bars in the rejection points are smaller than the size of the symbols.

Wetting of porous membranes, which leads to the increase in total mass transfer resistance and to a reduction in salt rejection, is considered as a major problem in MD. Even for hydrophobic membranes, aqueous solutions can partially penetrate pores and cause wetting. Here, results showed that the conductivity measurements on the permeate side during MD test did not detect significant changes when testing composite membranes for more than 12 h. The higher salt rejection observed for hydrogel composite membranes indicates that HCMs operate without wetting problems, so that the rejection remained high at the end of the operating period.
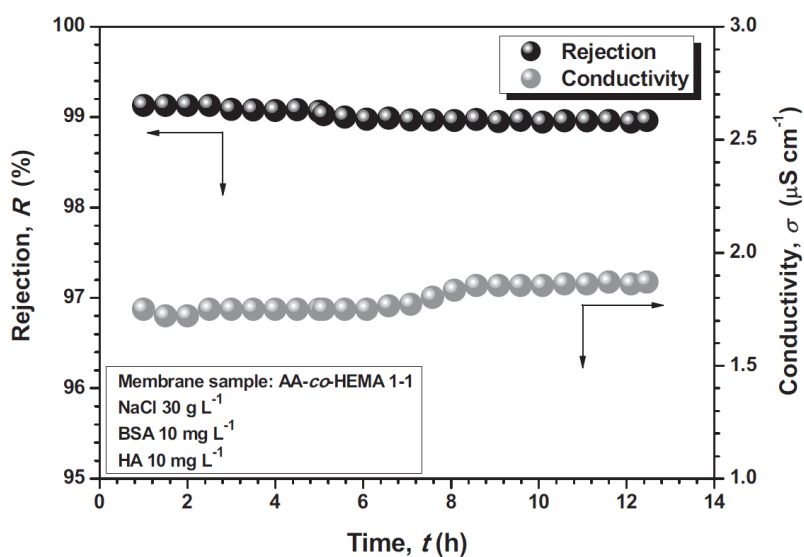
Figure 31 Rejection R and conductivity of the distillates with the time for MD tests with AA-co-HEMA 1-1

This special behavior of HCMs in MD operations in response to the gel layer composition and the feed solution concentration can be explained by the chemical nature of the hydrogel phase and its synergistic interaction with the hydrophobic porous support in the overall multi-stage and multi-phase transport mechanism occurring in composites. As the polyelectrolyte layer rejects ions under the effect of the Donnan potential, almost pure water diffused towards the gel/support interface and reaches gel-support interface; where, the higher vapor pressure of water than bulk salt solution, drives the enhanced evaporation rate because of the increasing driving force.

The term of Donnan potential refers to the distribution of ion species between two ionic solutions separated by a semipermeable membrane or boundary. The boundary layer maintains an unequal distribution of ionic solute concentration by acting as a selective barrier to ionic diffusion. Some species of ions may pass through the barrier while others may not. By increasing charge density in the gel network (increased AA/HEMA molar ratio), higher Donnan potential is generated, so that enhanced driving force stimulates higher flux, according to experimental results shown in Figure 17. At the same time, shrinking of the hydrogel layer under the effect of the salt solutions explains the enhanced transmembrane water flux observed with NaCl solutions compared to pure water. Crosslinked gels anchored to the support are predominantly characterized by uniaxial swelling/shrinking in the direction perpendicular to the substrate [66, 67], leading to strong anisotropic deformation. Because lateral distortion parallel to the surface is suppressed by the covalent binding of the polymer to the PP substrate, generated via during graft polymerization [83]. The less degree of swelling of composites compared to bulk-free hydrogel confirms the overall restriction to swelling imposed by gel anchoring to the support. Under the effect of the salt solutions, uniaxial thinning of the gel layer causes to reduced resistance to mass-transfer. Furthermore, while isotropic shrinking of bulk hydrogels is generally known to reduce mesh size, anisotropic deformation experienced by anchored gel layers is substantially ineffective in modifying mesh sizes compared to the complete swollen state [66]. Therefore, the net effect of hydrogel deswelling on mass transfer is the substantial reduction in the resistance to mass transfer. Consequently, higher transmembrane fluxes with NaCl solutions are explained by the anisotropic shrinking of the gel anchored to the PP support.

A qualitative description of the temperature profile in the system associated to the bulk temperature gradient between the two side of the composite membranes and to the multiphase transport mechanism involving evaporation and condensation at the two PP/solutions interfaces, is shown in Figure 32. The salt solution, with bulk concentration C_S faces the hydrogel layer side of the composites. The hydrophilic gel attracts water molecules so that it swells as function of the external solution concentration (and temperature). As solvent molecules are transferred through the composite membrane, the retained solute tends to accumulate at the solution/hydrogel interface, where its concentration gradually increases giving rise to a concentration polarization layer. Here, solute concentration $C_{S,i}$ is given by:

$$C_{S,I} = C_S \exp\left(\frac{J_W}{k}\right) \tag{9}$$

With J_W the overall water flux and k the mass transfer coefficient. Salt ions are retained by the electrostatic repulsions between the fixed charged groups in the hydrogel network (carboxyl and hydroxyl groups) and the Cl⁻ ions and by the Donnan exclusion potential. Increasing NaCl concentration, the co-ion concentration (i.e. the Cl⁻ moving together with the Na⁺ because of the principle of electrostatic neutrality) in the hydrogel is increased (thus decreasing the perm selectivity). As first approximation for a monovalent salt, the effective concentration of salt inside the polyelectrolyte gel $C_{s,i}$ is given by [84]:

$$C_{S,I}^* = \frac{C_{S,I}^2}{C_{fix}} \tag{10}$$

Where C_{fix} is the density of fixed charges in the polyelectrolyte gel layer. At the stationary condition, the overall water flux J_W through composite need to be the same as in the feed solution (J_W^{Sol}), in the hydrogel layer (J_W^{Hyd}), and in the support (J_W^{Sup}). The flux of water in both feed solution and the hydrogel layer is the result of diffusive transport, so that it can be expressed by the Fick's first law:

$$J_W^{Sol} = J_W^{Hyd} \propto -D \frac{dC}{dx} \tag{11}$$

With D being the diffusion coefficient, that differs in the solution and hydrogel phase. At the hydrogel/support interface water evaporates so that the effective concentration of salt ions increases to $C_{S,I}$. Vapor flux in the dry pores of the support can be described by the Dusty Gas Model (DMG) [85]. In the case of stagnant air-filled pores and direct contact membrane distillation configuration (Knudsen molecular diffusion transition), the following relations are frequently used to describe gaseous molar flux:

$$J_W^{Sup} = -\frac{1}{RT}\left[\frac{1}{D_{i,e}^k} + \frac{p_{air}}{D_{ij,e}^0}\right]^{-1}\frac{dp_i}{dx} \tag{12}$$

$$D_{ij,e}^0 = PD_{ij} \tag{13}$$

$$D_{i,e}^k = K_0\left(\frac{8RT}{\pi M_i}\right)^{1/2} \tag{14}$$

$$K_0 = \frac{2\varepsilon r}{3\tau} \tag{15}$$

Where D_k is the Knudsen diffusion coefficient, D_0 the molecular diffusion coefficient, p_i the partial pressure of water vapor evaluated at the membrane surfaces, p_{air} the partial pressure of air, R is the gas constant, T the absolute temperature, ε the membrane porosity, τ the pore tortuosity, and r the pore radius. Under script e indicates the effective diffusion coefficient calculated by considering the structural parameters of the membrane, while i and j refer to the two gaseous components (vapor and air, respectively).
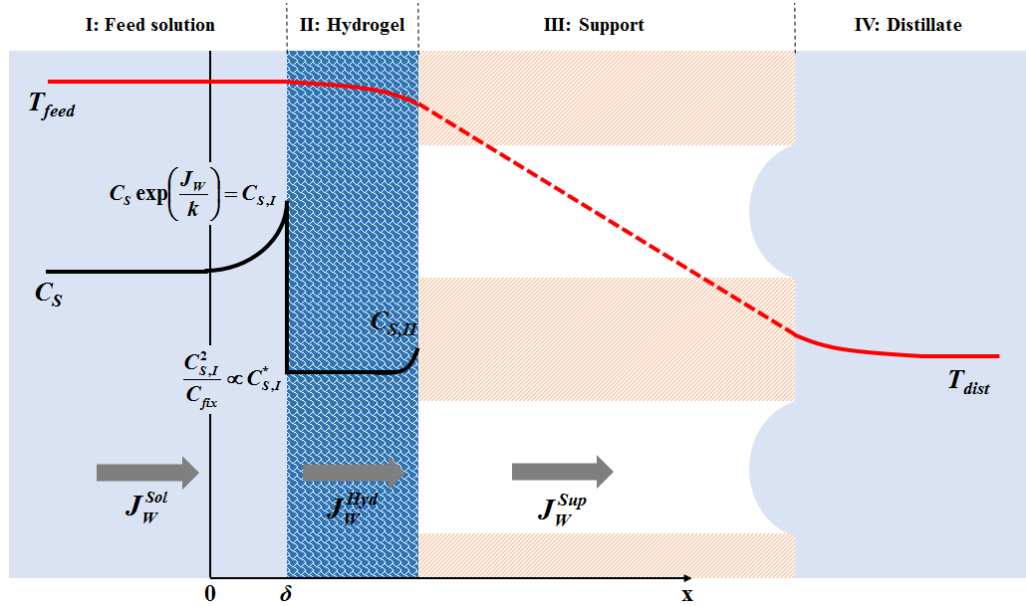
Figure 32 Simplified description of the concentration and temperature profiles in composites [86]

3.1.5. Conclusions

In summary, this work provides a way to achieve both high water permeability and salt rejection in desalination by developing novel ionic-strength responsive hydrogel composites with tailored chemical functionality. Contrary to conventional MD processes, the gating mechanism of composites developed in this study arise from the synergism between the polyelectrolyte nature of the hydrogel and the hydrophobic properties of the support, which controls multi-stage and multi-phase mass transport between two subsystems. The main advantage of such composites, compared to uncharged hydrophobic membranes conventionally used in MD, is the formation of a new interface between the support and the solution which is mediated by the hydrogel layer and offers an additional resistance to mass transport. However, when an electrolyte solution is used as feed, the hydrogel rejects ions by electrostatic repulsion and almost pure water can diffuse through the gel layer and reaches the hydrophilic/hydrophobic interface, where, the higher vapor pressure of water than bulk solution drives the enhanced evaporation and the mass transport. So, charge (donnan) exclusion is the dominant mechanism of salt rejection by polyelectrolyte composite membranes. Additionally, anisotropic deformation of the anchored hydrogel layer under the effect of the salt ions provides reduced resistance to mass transfer by the thinner gel layer (deswelling effect), compared to pure water conditions. This combined mechanism provides higher water-transfer flux and enhanced ion rejection than traditional MD membranes. Potential application of such innovative approach would be in water desalination by MD, where the paradox of increasing flux with the time (up to the limit of the system) as salt solution concentrates (the opposite behavior of RO) could be observed because of the ionic strength-responsive behavior of the gel layer. Furthermore, since hydrophobic attraction is the main interaction mechanism in aqueous systems between fouling particles and membrane, hydrogel composites offer the added advantage to provide a hydrophilic layer thereby reducing nonspecific binding to the membrane surface, thus potentially reducing fouling effects [53, 87]. Although absolute water fluxes in composite hydrogel membranes are not remarkably high, further optimization would be achieved by developing engineered supports to sustain higher fluxes, and tailored hydrogel functionalization for larger ion rejection.

3.2. Biomimetic Synthesis of CaCO₃ Structures by Hydrogel Composite Membranes

3.2.1. Introduction

Biomimetic synthesis is currently considered as the most promising strategy for the design of advanced materials under ambient conditions and low energy requirements [88, 89]. This is because, biogenic materials display a wide range of hierarchically organized and composite organic/inorganic structures that provide them with exceptional physical properties [90-92]. Among biominerals, calcium carbonate is the most abundant in nature which exists in three main crystal polymorphs: calcite, aragonite, vaterite and is considered as one of the standard model systems for studying biomimetic mineralization. With the aim to understand and to reproduce natural processes, a number of efforts have been devoted so far to produce $CaCO_3$ based materials by biomimetic approaches [93]. Several studies demonstrated that most biomineralization processes occur in confined environments within gel like organic matrices [94, 95]. Such natural organic media show features strikingly similar to those of hydrogel systems [95, 96]. The unique aspect of crystal grow in hydrogels drives from the compartmentalization of the solution into small cavities within the three-dimensional porous structure of gels. The microenvironment in a hydrogel differs greatly in diffusion rates, ion activities, and water structure (due to the hydrophobic nature of the gel) as compared to solution condition for crystallization. All these factors have a direct impact on the level of supersaturation and thus a gel is predicated to influence the kinetic of crystallization. Accordingly, crystal growth in gels has become the method of choice to study the crystallization of $CaCO_3$ in vitro as a key to synthesize new materials [97]. Natural gel networks are formed by assemblies of proteins, polysaccharides, and glycoproteins that control nucleation of the inorganic phase by stereo chemical recognition and molecular binding effects [98-100]. Synthetic mimics of these natural templates can be developed with supports having acidic functionalities, such as carboxyl and hydroxyl groups. These functional groups can interact with diffusing solutes (Ca^{2+} and CO_3^{2-}), to change the local concentration of reactants (supersaturation), and can serve as nucleation sites to direct the orientation of crystals within the hydrogel network [101-103]. Over the past decades, different functional groups such as $-COOH$, NH_2, OH, SO_3, SH and PO_4H_2 have been designed into 2D or even 3D models to control $CaCO_3$ biomineralization. These chemical groups represent fundamental components of various substances at molecular level. Therefore, the role of organic substance like collagen, protein and other extracellular matrix

on CaCO$_3$ biomineralization could be mimicked by such functional groups [104]. When using this approach, a wide range of crystals morphologies, most of them displaying a polycrystalline or mesocrystalline structure, was obtained in a great variety of experimental conditions [105]. Despite the widespread variability of the observed external shapes, the role of the organic hydrogel phase in regulating CaCO$_3$ morphogenesis or the selection of specific polymorphs is still poorly understood, in some cases appearing the exclusive effect of the local gradient of supersaturation [106]. However, understanding of how the organic phase influences CaCO$_3$ growth mechanisms is a topic of considerable interest both in biology and materials chemistry. Here we report on the use of hydrogel composite membranes as a novel platform for the biomimetic synthesis of CaCO$_3$ superstructures. Understanding chemistry of the hydrogel affects the local crystallization environment and charged and/or polar functional groups present a number of control variables for the growth of calcium carbonate crystals, different hydrogel materials such as acrylic acid, meth acrylic acid, and 2-hydroxyethyl methacrylate which contains carboxylic and hydroxyl groups were selected for this study. Hydrogel composite membranes were fabricated by the direct synthesis of a tailored gel layer on the surface of a polymeric porous support, according to previously described procedures. This composite provides the opportunity to fine control the delivery of additives to the gel network through the porous structure of both support membrane and hydrogel layer, thus affecting crystallization kinetics. Results demonstrated the crucial role of the organic matters in the formation of complex CaCO$_3$ structures resembling biogenic products. Furthermore, the mechanism of formation of biomimetic CaCO$_3$ spherulites at the gel/solution/ air interface and under reduced crystallization process in hydrogel composite membrane assisted was discussed.

3.2.2. Materials

Two commercial membranes: Polypropylene flat sheet membranes (Accurel PP 2E HF, and poly ether sulfone flat sheet membranes (Micro PES 2F) were from Membrana GmbH (Wuppertal, Germany). Acrylic acid (AA, monomer, cod.101302902), metacrylic acid (MAA, monomer, cod. 155721), 2-hydroxyethyl methacrylate (HEMA, monomer, cod.101095911), ethylene glycol dimethacrylate (EGDMA, cross-linker, cod.1012880077), polyethylene glycol dimethacrylate (PEGDMA, average Mn. 750 Da, cross-linker, cod. 437468), 2-hydroxy-2-methyl propiophenone (photoinitiator, cod.1001451059), were from Sigma Aldrich. Sodium chloride (cod.131659.1211) was from Panreac. Calcium chloride dehydrate (cod. 22317.297) was from VWR. Ammonium carbonate (cod. 11204) and Methanol (HPLC grade, cod. 20864.320) were from Sigma-Aldrich. L-Glutamic acid (cod.131659.1211), D-glutamicacid (cod.131659.1211), and D, L-glutamic acid (cod.131659.1211) were from Sigma Aldrich. All chemicals were used as received and water purified with a Milli-Q system was used for all experiments. Various hydrogel composite membranes Table 6 were prepared as described previously in chapter 2.1.3.

Table 6 Hydrogel composite membranes samples for calcium carbonate crystallization test

Samples No.	Code. Monomer(s)- (molar ratio)/cross linker /membrane support
1	AA/ EGDMA/ PP
2	AA/ EGDMA/ PES
3-7	AA-co-HEMA (1:1-5) / EGDMA/ PP
6-12	AA-co-HEMA (1:1-5) / EGDMA/ PES
13	AA-co-HEMA (1:4) / PEGDMA/ PP
14	AA-co-HEMA (1:4) / PEGDMA/ PES
15	MAA/ EGDMA/ PP
16	MAA/ EGDMA/ PES
17	MAA-co-HEMA (1:4)/ PEGDMA/ PP
18	MAA-co-HEMA (1:4)/ PEGDMA/ PES
19	HEMA/ EGDMA/ PP
20	HEMA/ EGDMA/ PES

3.2.3. Calcium Carbonate Crystallization Test

The performance of the prepared HCMs in $CaCO_3$ crystallization was tested by ammonium carbonate decomposition/CO_2 diffusion technique. This method relies on the decomposition of ammonium carbonate to produce carbon dioxide and ammonia gas and the diffusion of CO_2 into a calcium chloride solution. The chemical reaction can be exemplified as:

$$(NH_4)_2CO_3 \rightarrow CO_2\,(g) + 2\,NH_3\,(g) + H_2O$$

$$CO_2\,(g) + CaCl_2 + 2\,NH_3\,(g) + H_2O \rightarrow CaCO_3\,(s) + 2\,NH_4Cl$$
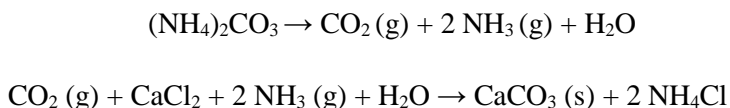
Crystallization tests were carried out in two different configurations: (1) crystallization on the hydrogel surface under the bulk solution and (2) crystallization at the hydrogel/solution/air interface. Calcium chloride solutions at different concentration were prepared by dissolving appropriate amounts of $CaCl_2 \cdot 2H_2O$ in pure water. Specifically, 1 mL of calcium chloride solution was pipetted inside the wells of modified screw top hanging drop plates. A circular HCM sample with a diameter of 1 cm was fixed to contact the $CaCl_2$ solution on the hydrogel side. The back surface of HCM (PP or PES side) was exposed to the stream of CO_2 coming from the decomposition of solid ammonium carbonate for one week (five replication experiments for each condition). Experiments were carried out in a closed desiccator, at room temperature, checking daily for the appearance of particles. By this approach, crystals formed on the hydrogel surface were surrounded by the bulk solution. Crystallization tests at gel/solution/air interface were carried out in a similar way as above by dispersing a droplet (30 µL) of $CaCl_2$ solution on the hydrogel side of HCM samples. Here, the droplet is absorbed by the hydrophilic gel layer so that $CaCO_3$ particles start to form at the gel/solution interface in the swollen hydrogel, but stop their growth in the perpendicular direction to the substrate at the solution/air interface and develop substantially in a bidimensional way. Reference tests were also performed by using virgin PP or PES membranes as substrate. Upon completion of the crystallization test, samples were taken out of the desiccator, carefully rinsed by a droplet of deionized water and dried at room temperature. In this study, the effects of calcium chloride concentration (5, 20 and 50 mM) and the presence L-Glutamic acid, D-glutamicacid, and D, L-glutamic acid as additives at different concentrations in the $CaCl_2$

solution were investigated as well. Glutamic acid contains carboxylic acid functional group and exists almost entirely in its negatively charged deprotonated carboxylate form (Figure 33).

D - glutamic acid   L - (+) - glutamic acid   DL - glutamic acid
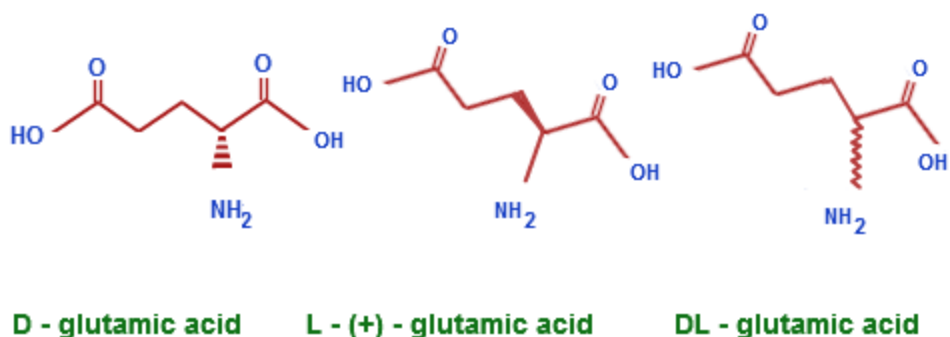
Figure 33 Molecular structure of Glutamic acid

3.2.4. Crystal Characterization

Morphological analysis was performed by a Quanta 200F FEI Philips scanning electron microscope. Chemical analysis of obtained crystals was carried out by a confocal Raman microscope (NRS 5100-Series Raman, from Jasco) equipped with a SHG Nd: YAG laser (532 nm) and a lens based spectrometer, using $1800\ mm^{-1}$ diffraction gratings. A $100\times$ microscope objective was used for the measurements. On the samples, two areas were selected under the microscope and two or three spots were analyzed from each area. The spectra were collected in the range 100–$1200\ cm^{-1}$.

3.2.5. Results and Discussion

As explained above, hydrogel composite membranes were used as dosing device to supply CO_2 (coming from the decomposition of ammonium carbonate) to $CaCl_2$ solution, and as heterogeneous functional support to provide the proper hydrogel environment for $CaCO_3$ crystallization. Figure 34 shows the basic apparatus working as membrane-assisted crystallization device [86]. The use of this system provides a suitable way to control the rate of supply of reagent, thus affecting the crystallization kinetics of the process.
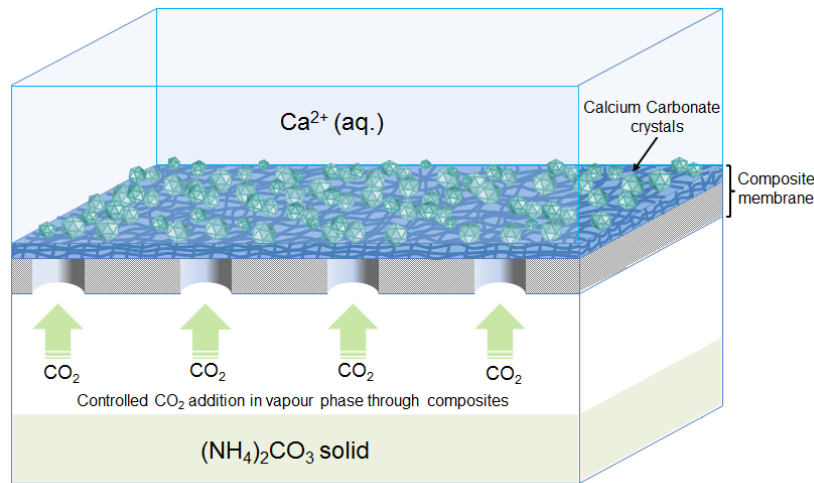
Figure 34 Membrane-assisted crystallization device [86] used for the biomimetic synthesis of CaCO3. Hydrogel composite membrane is used to contact the CaCl2 solution and the compartment containing solid ammonium carbonate. Carbon dioxide comes from the spontaneous decomposition of the solid, goes through the porous composite membrane and reacts with Ca2+ in the gel layer, thus providing the formation of synthetic minerals

Calcium carbonate has three anhydrous crystalline polymorphs, that is, vaterite (the least thermodynamically stable), aragonite, and calcite (the most stable). Reference crystallization tests using virgin PP or PES supports gave invariably rhombohedral crystals over nearly 24 h (Figure 35 a, b). Formation of stable calcite rhombohedra is a common phenomenon when calcium carbonate precipitation is obtained without additives by using a gas diffusion technique. Raman spectra confirmed the calcite nature of crystals obtained with virgin PP and PES supports (Figure 41 a) [107, 108]. Experiments performed with HCM-platform under similar conditions provided a wide range of crystal morphologies after a few days. The delayed induction time for crystals' appearance proved that composites slow down the mineralization kinetics because of the lower diffusion rate of CO_2 through the hydrogel layer compared to the virgin supports. In fact, while the gas transfer rate through macroporous hydrophobic membrane (with average size of 2 µm) is not affected by steric hindrance, the CO_2 transport in composites is significantly limited by mass transfer resistances. Therefore, crystallization kinetics can be potentially controlled by modulating hydrogel composite properties such as thickness, mesh size, swelling degree etc. For HCMs with hydrogel layers containing HEMA as single monomers, no significant changes in morphology were observed as shown in Figure 35 c, this proves that hydroxyl groups have weak interactions with $CaCO_3$ components when taken alone in these kinds of gel, and can be considered as

substantially inert materials in CaCO₃ crystallization. For HCMs with hydrogels synthetized by single monomers bearing carboxylate groups (AA and MAA), experiments resulted in the formation of particles exhibiting "distorted" morphologies (Figure 35 d, e); this confirms the influence of these chemical moieties in the deformation of the native rhombohedra. The interaction between hydrogel and CaCO₃ components triggers different supersaturation regimes through Ca^{2+} ions binding. This interaction is strong enough to disturb the formation of the typical calcite solids and to promote the appearance of new morphologies resulting from flat rhombohedra stacked together to lower their interface energy.
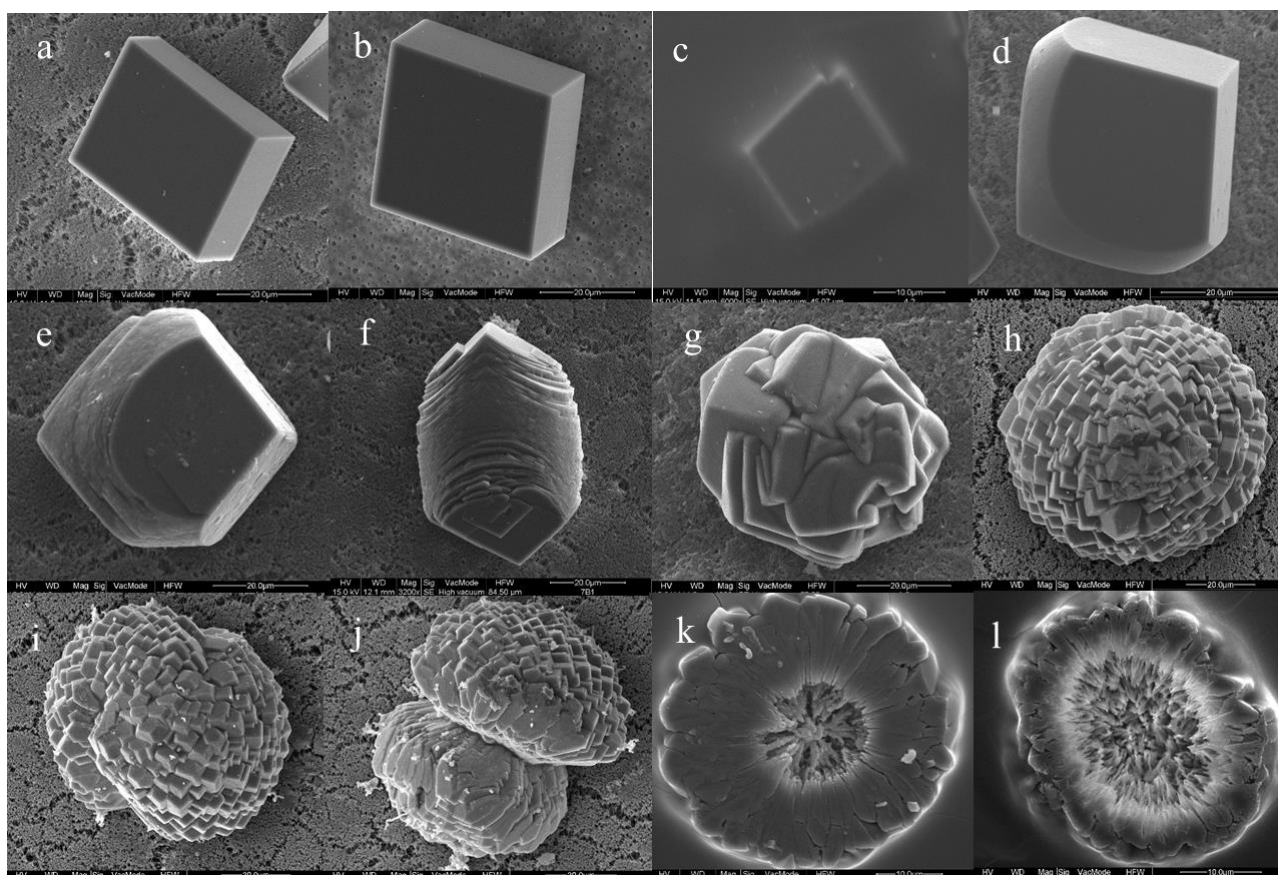
Figure 35 Crystals obtained by using different substrates: (a) virgin PP, (b) virgin PES, (c) HEMA/EGDMA, (d) AA/EGDMA, (e) MAA/EGDMA, (f, g) MAA-co-HEMA/PEGDMA, (h, I, j) AA-co-HEMA/PEGDMA, (k, l) AA-co-HEMA/EGDMA HCMs

Ouhenia et al. [109] observed a similar erosion behavior (distorted morphologies) of calcite rhombs in the presence of poly acrylic acid. The calcite rhombs show less regular faces with more steps and porosities as shown in Figure 34.
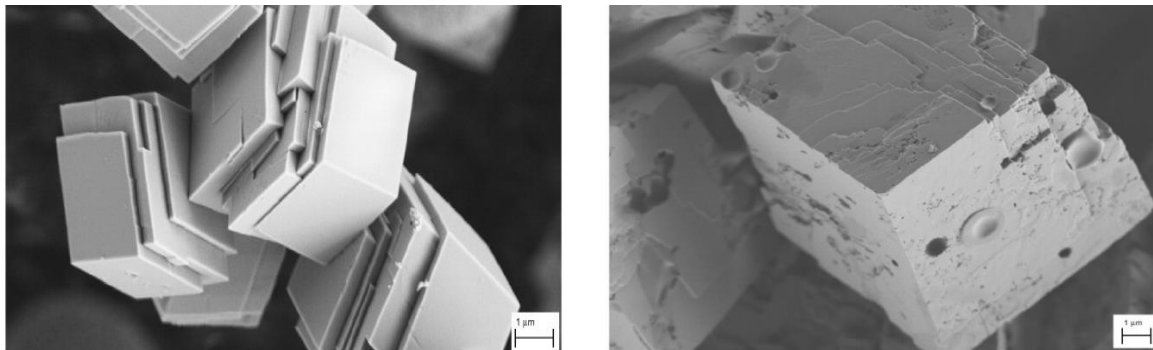
Figure 36 Calcite rhombs obtained in the presence of poly acrylic acid [109]

This means that composites formed by AA or MAA and HEMA give strong selectivity in the crystal products, a feature that is not owned by the other monomers types, or even by the same taken separately. The strong influence of the two combined monomers on calcite crystallization and its morphogenesis can be seen as a cooperative effect. In this framework, the relevant contribution of the monomer ratio resides on the fact that it is different from zero only in the case of copolymerization: it is responsible for the progressive transformation from rhombohedral to spherical crystal shape. Similar morphologies of $CaCO_3$ crystals grown in agarose hydrogel and alginate hydrogel in the presence of poly AA have been observed and formation of large calcite aggregates, which consist of intermediate shape such as small spheres, peanut and dumbbell structures have been obtained due to the interaction between hydroxyl groups and the carboxyl or amino groups [110].
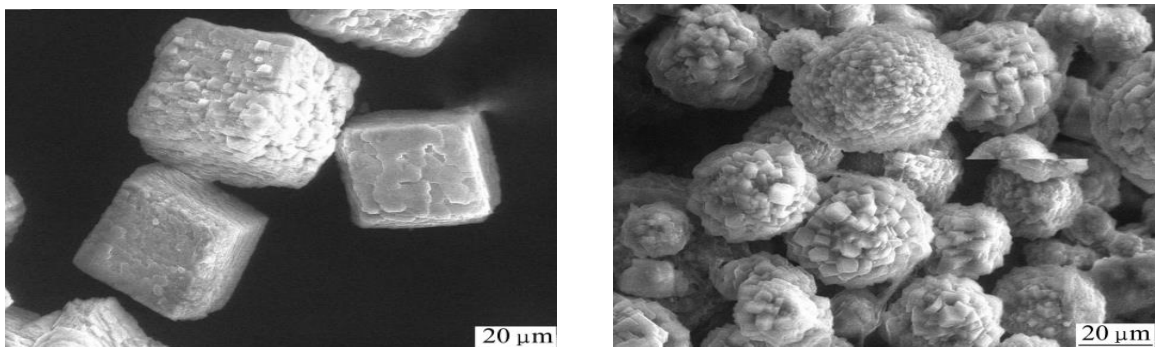
Figure 37 SEM of calcium carbonate crystals grown in (a) agarose gel (b) alginate gel in the presence of AA, different morphology due to the interaction between hydroxyl groups and the carboxyl or amino groups [110]

This result demonstrates the fundamental influence of the carboxylate groups in the formation of complex $CaCO_3$ crystal morphologies. Carboxyl groups are mostly deprotonated, meaning they lose an H^+, and become negatively charged. Ca^{2+} ions can bind to carboxylate groups through an electrostatic effect and induce anionic vesicles aggregation, thus changing the local concentration. The interaction of Ca^{2+} with anionic groups has been studied widely, and large numbers of papers and reviews have been published and demonstrated electrostatic and stereo-chemical interaction between carboxylate groups and $CaCO_3$ dominates nucleation at initial stage and directs the orientation of crystal within the hydrogel network. Experiments performed with glutamic acid (D, L, and DL) as additive in HCMs mineralization resulted in a mixture of spherical-like vaterite crystals and regularly shaped calcite crystals (Figure 38) in the case of L glutamic acid.
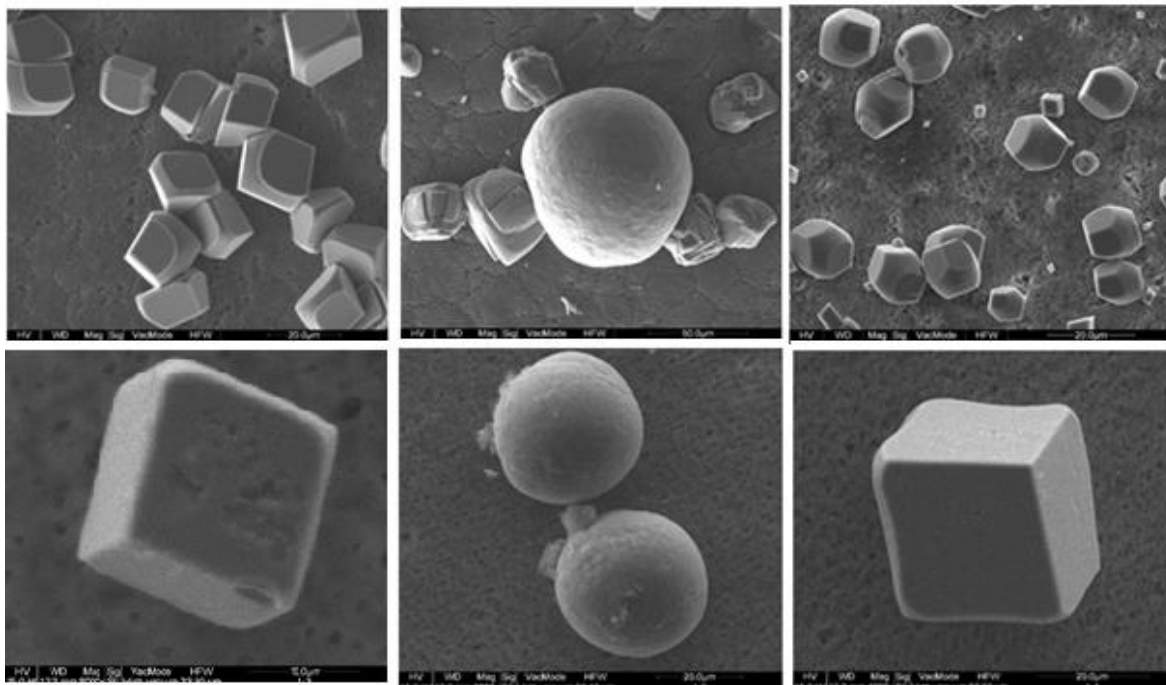
Figure 38 CaCO₃ crystal morphology in the presence of D, L ad DL-glutamic acid: HCMs supported on a) PP, b) PES membranes

As shown by Raman microscopy (Figure 39), in the presence of D and DL-glutamic acid, only the band at 1085 and 712 cm^{-1} corresponding to calcite phase was observed but when L-

glutamic acid was added to the $CaCl_2$ solution, the characteristic 1091 and 1076 cm^{-1} peaks and the band at 745 cm^{-1} corresponding to vaterite were observed and the band at 712cm^{-1} disappeared.
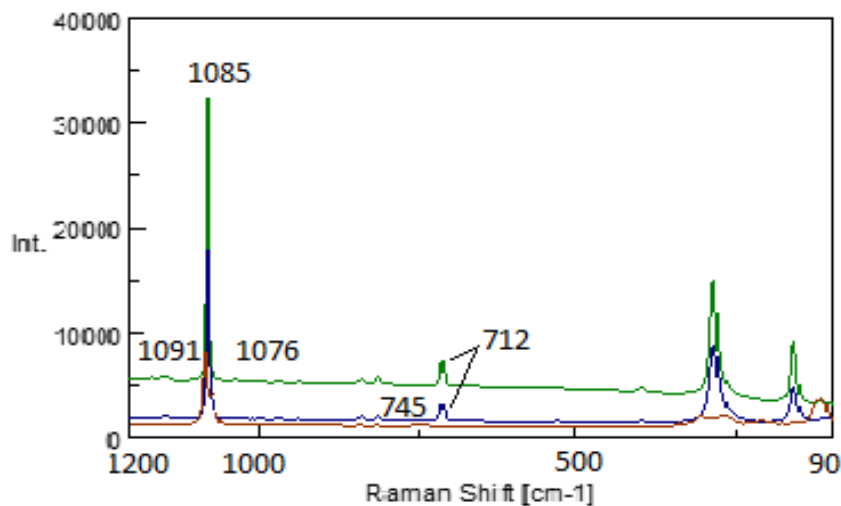
Figure 39 Raman spectra of crystalline samples in the presence of D, L and DL glutamic acid

These observations are coherent with the known effect of glutamic acid to induce the growth of vaterite in some circumstances. In the present of D-glutamic and DL-glutamic acid, the crystals formed were mostly calcite, however SEM studies showed different kinds of rhombic crystals formed, one with smooth surfaces and the others with holes or with secondary crystals on the crystal surface. Analyses of the data showed that, in fact, D and DL-glutamic acid do not affect the output of crystallization to any significant extent, yielding crystals that are very similar to those obtained from experiments without additives. In some cases, they modulate the morphology of calcite crystals in a way that many of the observed rhombohedra do no longer exhibit sharp and defined edges, but have a rounded appearance instead. The introduction of the L-glutamic caused the formation of the vaterite form. Vaterite crystals mostly expressed a spherical morphology for virgin membranes. SEM studies showed the cubes and traces of micro-spherical balls together, which confirms the effect of L-glutamic acid to promote the formation of vaterite, the less thermodynamically stable $CaCO_3$ polymorph. Based on the results of this study, we can conclude that in the presence of L-glutamic acid, the transition between the calcite and calcite + vaterite

precipitation is controlled. Thus, the phase transformation of vaterite to form a more thermodynamic stable polymorph is suppressed by L-glutamic acid.

According to classification criteria [111], three different crystal morphologies can be obtained by using HCMs: (1) single, well-faceted rhombohedral shaped particles with smooth surfaces; (2) single crystals exhibiting flat (104) faces coupled with curved and rough ones, or disturbed by preferential growth along certain directions; and (3) polycrystalline particles resulting from thigh stacking of rhombohedral subunits. In order to interpret coherently the crystal shapes and to relate them to the experimental conditions, partial least square regression (PLSR) [112], a multivariate statistical technique was applied (This work has done in collaboration with ICT). By using this approach, it is possible to build a statistically regression model which can explain crystallization evidences obtained in this study. This model offers two advantages: first, it can be interpreted to investigate the relationships between crystals morphologies and experimental variables (understand how the several conditions combine to determine the crystallization outcome); second, it can be used to as a predictive tool for experimental results. To build the PLSR model, a scanning electron microscopy (SEM) image representative of the most frequently obtained crystal morphology for a given set of experimental conditions is selected. Similar morphologies are clustered also considering the classification criteria for $CaCO_3$ shapes used in analogous studies (see Appendix A). Numerical values (descriptors) are then associated to each cluster of images and related to the experimental conditions by PLSR. The descriptor values estimated by the PLSR model were highly correlated with the predictor values assigned based on the crystal morphology. It means that reliable descriptor values for experimental conditions not actually implemented can be also estimated, thus giving a way to predict the outcome of future crystallization experiments (p=88.6%). The representative points in the scatter plot of Figure 38 a are clearly separated into two groups: crystals with mainly smooth surface and rhombohedral-shaped (clusters 1–5 of Table 1, Appendix A) belong to group A, while segmented crystals with wrinkled surface, oblate or quasi-spherical form (clusters 6–17) belong to group B.
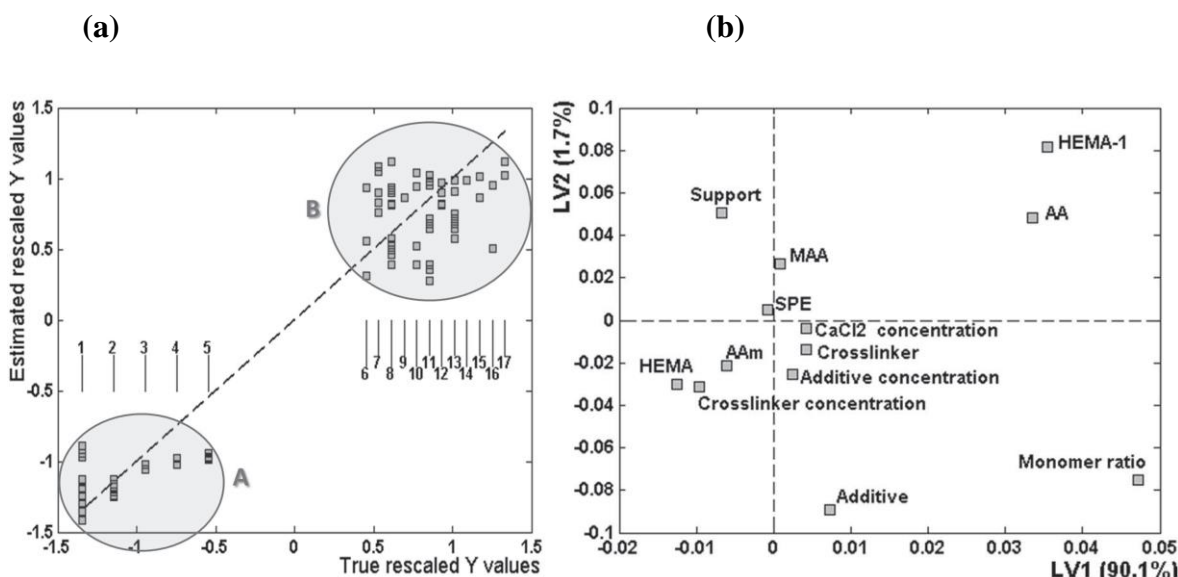
Figure 40 (a) Scatter plot of the response values estimated by the PLSR model (estimated Y values) versus those assigned in Table S3 (true Y values). Two groups of representative samples are highlighted, corresponding to rhombohedra and smooth crystals (group A), spherical and segmented crystals (group B); (b) Scatter plot of the weights of the second (LV2) versus the first (LV1) latent variables of the regression model. The distance of the representative points from the origin, highlighted by the two dashed lines, indicates the importance of the experimental conditions in explaining the data variance [75]

The 91.6% of the overall data variance is explained by the PLSR model, which means that a relationship between the characteristics of the crystals contained in groups A and B and the experimental setup to obtain them is identified. The characteristics of this relationship can be investigated by interpreting the PLSR model. It is possible to point out the role played by the different experimental conditions in determining the outcome of the crystallization experiment. In Figure 38 b, the scatter plot of the weights of the variables which properly describe the data is reported. In this plot, the distance from the origin of the representative points is proportional to the importance of the corresponding experimental conditions in explaining the data, and the distance between points is proportional to the degree of their independence. The most important latent variable (LV1), which explains 90.1% of sample variability, is dominated by the experimental parameters AA, HEMA-1, and Monomer ratio, where HEMA-1 is defined as the monomer HEMA used as co monomer (with AA or MAA) in the hydrogel synthesis. These variables are mainly responsible for the distinction between groups A and B. The residual data variability (1.7%) is explained by the second latent variable (LV2), mainly depending on the support and additive parameters. We found that these variables are in fact responsible for the differentiation of crystals

within group B in terms of both morphology and polymorphic selection. Variables not mentioned before play a negligible or not-unique role in determining the crystal morphology.

A relevant aspect related to the formation of polycrystalline spherulites is related to the formation of ACC at the early stages of crystallization. In this framework, ACC undergoes phase transition and causes the different morphologies to be stabilized. Generally, the formation of $CaCO_3$ superstructures is explained by a deductive approach based on the observation of fractured or etched spherulites [113, 114]. In this study, by using the innovative HCMs platform, the growth of polycrystalline particles is forced at the gel/solution/air interface. Additionally, the slow mineralization process on hydrogel allows to observe simultaneously several individuals at different stage of maturity. Therefore, to directly inspect the morphogenesis of polycrystalline particles through their preferential bidimensional evolution (Figure 42), without any invasive procedures. As revealed by the present investigation, the formation of spherulites occurs by a multistep mechanism in which a hollow core is initially formed by radial growth of needle-like subunits (Figure 42 a). These subunits progressively migrate concentrically towards the centre living the back position as a solid surface. The higher resolution image reveals that radially ordered structures are composed of 200-400 nm blocky nanoparticles, displaying the typical morphology of the ACC phase (Figure 42 g). The nature of these nanoparticles has been confirmed by Raman analysis. In contrast to the spectra of the $CaCO_3$ crystals precipitated with virgin membrane support (Figure 41 a), the Raman spectra collected from location at the center of the particle shows a significant reduction in the intensity of the 1078 cm^{-1} peak and the notable absence of the peak around to 704 cm^{-1} (Figure 41 d) [115-117]. The Raman spectra collected form the solid region on the external side of the polycrystalline particle shows signals which are the characteristic peaks of the calcite phase (Figure 41 c). Therefore, the growth of spherulitics is consistent with a topotactic transformation from ACC nanoparticles, that aggregate and self-organize into amorphous radial structures at an early stage, to calcite with a circular front that concentrically proceeds towards the core of the structure. Only after these nanoparticles grew out to dimensions of several hundreds of nm were they able to develop crystallinity giving rise to calcite crystals.
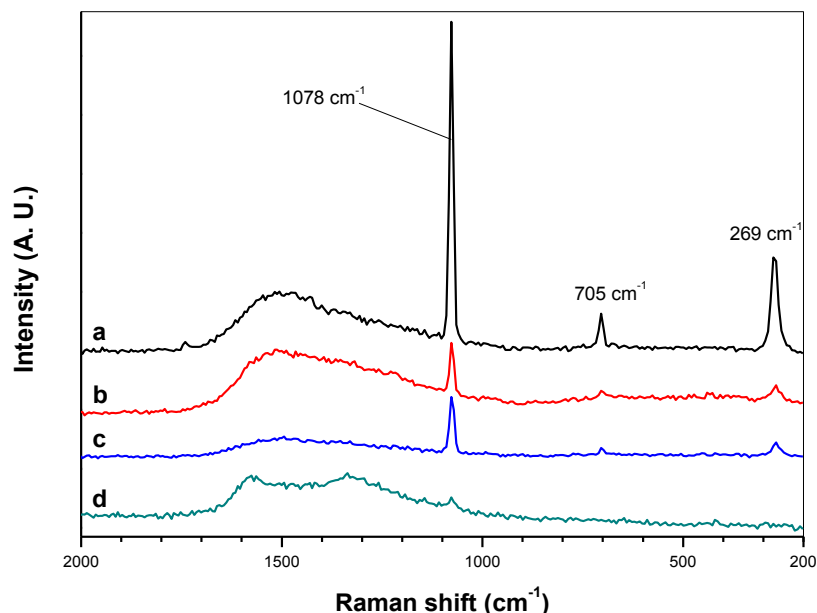
Figure 41. Representative Raman spectra of crystalline samples: (a) rhombohedral well-faceted crystals obtained with virgin PP and PES membranes and with HEMA HCMs; (b) rosette shaped polycrystalline structures; (c) marguerite shaped structures in the outside point; (d) marguerite shaped structures in the central part

In Figure 42 h and i, it is possible to see the transition of nanometric particles to rhomboedral shaped crystals and the solidification stage that occurs by the fusion of blocks formed by several sub-parallel crystals, slightly tilted relative to each other, forming a crystalline twist or vortex converging towards the core of the structure. By this mechanism, ACC behaves as transient precursor (metastable phase) which readily transforms to the more stable crystalline phase of calcium carbonate [118-120] according to the Ostwald's step rule, as found in the onset of biomineralization in a variety of living organisms [116, 120-122]. In biogenic processes, the transformation of ACC is tightly controlled often by acidic proteins and in some cases the amorphous form is permanently stabilized [123-125]. In   vitro the temporary stabilization of ACC must be ascribed to the organic matter in the hydrogel network. Hydroxyl and carboxyl groups in the hydrogel network of HCMs act as a sponge for calcium ions. The highly localized supersaturation provides the temporary stabilization of ACC nanoparticles that grow out of the critical size by several hundreds of nanometers, until they are able to develop crystallinity through solid-state transformation giving rise to more stable phases [126]. This transformation, occurring

under the cooperative effect of weakly interacting hydroxyl groups and strongly interacting carboxyl moieties with the surface of calcite, generates complex crystals textures.
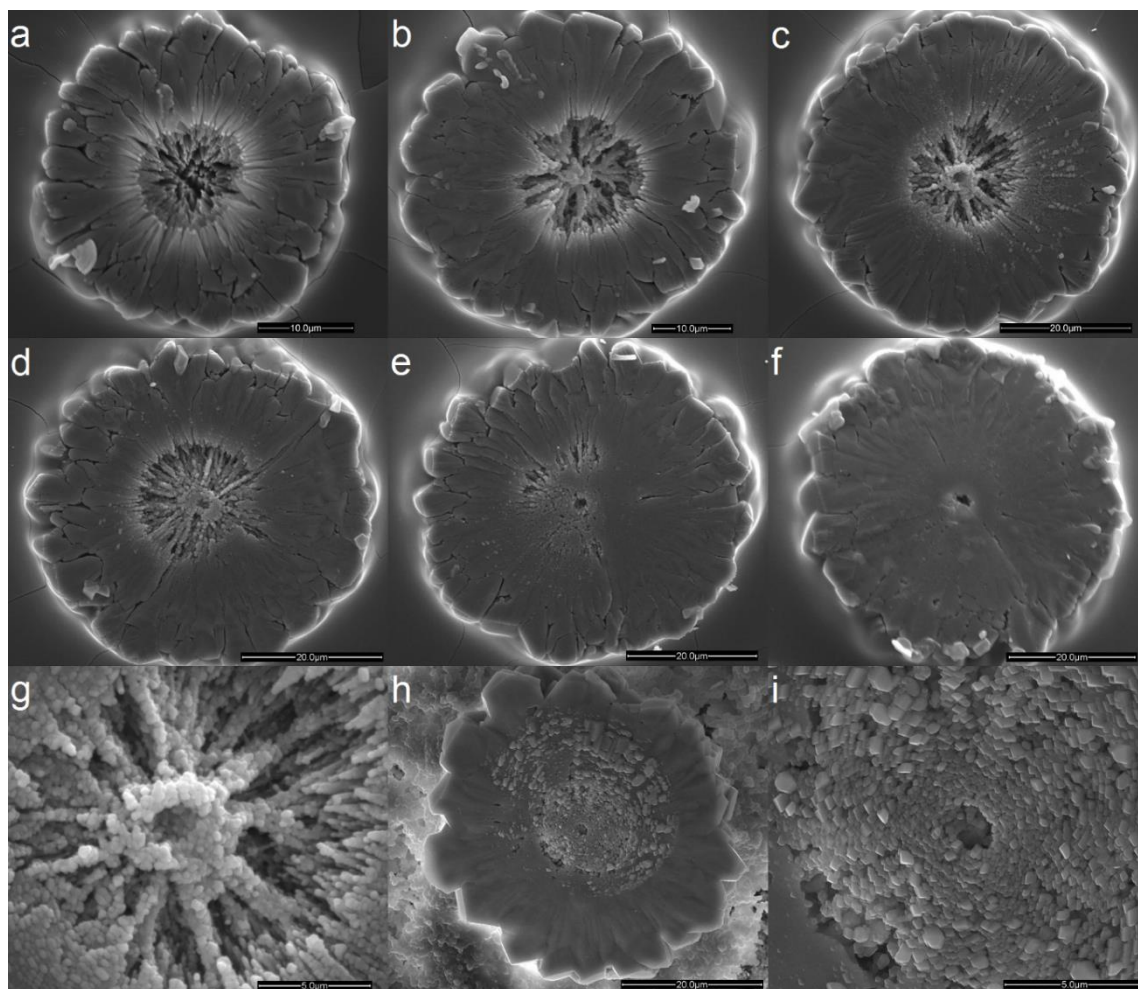
Figure 42 Bidimensional evolution of CaCO3 spherulites grown at the gel/solution/air interface in a HCMs mineralization platform, operated at low supply rate of reactants (poly AA-co-HEMA/EGDMA 1–4 HCMs, PP support). Individuals at different stage of maturity are obtained in the same batch under slow mineralization kinetics.

In our opinion, the combination of these strong/weak interactions provides the system with the necessary degrees of freedom and flexibility to promote the formation of complex architectures.

3.2.6. Conclusions

Understanding chemistry and structure of the hydrogel affects the local crystallization environment and charged and/or polar functional groups present many control variables for the growth of calcium carbonate crystals, different hydrogel materials such as acrylic acid, methacrylic acid and 2-hydroxyethyl methacrylate containing carboxylic and hydroxyl groups, were selected for this study. Various hydrogel composite membranes (HCMs) were synthesized using photo initiated polymerization of functional monomers and cross-linkers on the surface of commercial PP and PES membranes and then used in calcium carbonate crystallization by gas diffusion method. These HCMs were used as dosing device to supply CO_2 (coming from the decomposition of ammonium carbonate) to $CaCl_2$ solution, and as heterogeneous functional support to provide the proper hydrogel environment for $CaCO_3$ crystallization. The novelty of this work was to use membrane-assisted crystallization device for the biomimetic synthesis of $CaCO_3$ by providing a suitable chemical environment for $CaCO_3$ crystallization through the fine control of the diffusion rate of CO_2. Generally, rhombohedral microcrystals were formed on both virgin membranes without hydrogel layer. Experiments performed with HCM-platform under similar conditions provided a wide range of crystal morphologies ranging from those of spherulites (rosettes and flower shape), peanuts spherical and twined superstructures were observed. As for the effect of carboxylic acid groups on the selection of crystal polymorphs, the present results showed that calcite is favored in these hydrogels, while the crystal morphologies are greatly different from each other. The chemical nature of the monomers was the key factor driving the crystal shape from regular well-faceted single crystals to polycrystalline quasi-spherical aggregates. On the basis of this study, HCMs may become a new approach for synthesizing materials with complex morphologies.

3.3. Hydrogel Composite Membranes Containing Iron Oxide Nanoparticles as Suitable Heteronucleant for Protein Crystallization

3.3.1. Introduction

Heterogeneous nucleation has been investigated over the last three decades to determine physico-chemical relationships between nucleant and solute properties, which may be a key factor for controlling nucleation. Nucleation occurs on the surface of the substrate, which creates a higher local concentration of solute molecules, lowers the energy barrier for nucleation and suspends the high kinetic barrier of spontaneous nucleation [127, 128]. It is thought that most of the bio macromolecular crystals such as protein that are supposedly grown homogeneously, in fact, have been nucleated heterogeneously due to insoluble aggregates or microscopic solid impurities [129]. It can be expected that the deliberate and selective control of the number of nuclei and the supersaturation point at which nuclei grow will lead to the formation of high quality crystals. This possibility has prompted a series of studies on the effects of the systematic introduction of heterogeneous nucleants in initial screening trials to identify a suitable crystallization condition that would have otherwise been missed [130, 131]. Some of the novel methods to induce heterogeneous nucleation include the application of porous nucleants [132-134], the lipidic cubic phase [135, 136], novel microfluidic platforms [137, 138], and etc. which have been reported successfully. Importantly, the cavities of this material are of similar sizes to those of protein molecules and are expected to entrap the protein molecules, thus promoting nucleation and crystal growth. The wide range of pore sizes and shapes that are available at the surface of a disordered porous material provide a large repertoire of pores among which the given macromolecule will be likely to find the pore of adequate size and shape to nucleate. Furthermore, materials of diverse chemical nature with irregular, rough surface structures other than pores can be designed to act as heterogeneous nucleants [139-141]. Moreover, surface with charge functional groups have been used to induce protein crystallization at lower protein crystallization compared to untreated surfaces. Studies on surfaces with ionizable functional groups suggests that functionalized surface could promote nucleation. Development of three dimensional nanotemplates with tuned specific surface porosity and surface chemistry to facilitate protein crystallization has been currently reported and the important role of the tuned porosity of the 3D nanotemplate in stabilizing the nuclei within the mesopores, thus, generating local immobilization as shown in Figure 43 has been

described [142]. Physical entrapment of protein molecules inside the cavities allows solute concentration up to the required level of supersaturation able to promote nucleation. Once the nuclei is formed, functional groups on the surface may stabilize the already formed nuclei by interacting with a specific crystal face [24].
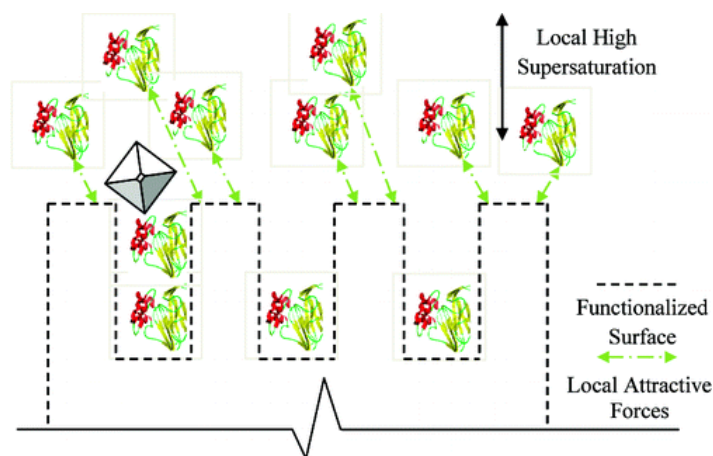
Figure 43 Schematic illustration of protein molecules interaction with the surface of the meso-pores 3D nanotemplates; Some of the pores are expected to entrap the protein molecules, thus promoting nucleation and crystal growth [142]

Polypropylene or polyvinyldene porous hydrophobic membranes are other materials reported to promote heterogeneous nucleation of protein molecules, drastically reducing the time required to induce nucleation [13, 16, 28, 143]. The ability to promote and control heterogeneous nucleation kinetics by modulating the physico-chemical properties of membranes (i.e. surface chemistry, porosity, roughness, and hydrophobicity/hydrophilicity) has been studied and demonstrated that the chemical nature of the surface dictates whether it would act as an effective nucleation active substrate, increased surface roughness can positively or negatively affect nucleation density depending on the surface wettability [12, 14, 26, 69, 144-146]. Hydrophobic surface has more tendency to adsorb molecules from solution, in this case, increase of roughness enhances nucleation. On the other hand, when using hydrophobic supports, an increase of roughness reduces heterogeneous nucleation. Therefore, the ability of a substrate surface to promote or hind heterogeneous nucleation during crystallization depends on an interplay between surface roughness and wettability. Combining the function of tailored membrane surface to

simulate controlled heterogeneous nucleation mechanism, with controlled solvent removal in vapor phase, represents a potential application of membrane assisted crystallization technology in the field of biomolecules crystallization [10, 28, 147]. In this study, functional membranes with tailored surface patterning were designed, in attempt to stimulate controlled heterogeneous nucleation while assuring a simultaneous solvent removal in the vapour phase, which would represent a potential application for protein crystallization. The functional composite membranes prepared in this study, were constituted by a polyvinyl alcohol (PVA) hydrogel layer with embedded Iron oxide nanoparticles (NPs), and supported on a microporous polypropylene membrane. NPs were used as topographical designers providing a good control of membrane surface roughness and patterning. Hen egg white lysozyme (HEWL) was used as protein model and crystallization experiments were carried out using vapor diffusion method. Based on the contact angle and roughness measurements, it was found that surface structural characteristics in addition to chemical and physical interactions between the surfaces and protein molecules have influence on the heterogeneous nucleation of protein crystals to different extents. We demonstrated that surface roughness promotes heterogeneous nucleation, potentially due to the increase of local protein concentration and decreasing the energetic barrier required for the aggregation of critical nuclei at rougher surfaces. Moreover, in contrast to conventional heterogeneous nucleation methods, these functional composite membranes allowed for the formation of a low number of well-shaped crystals with a larger size.

3.3.2. Materials

Commercial polypropylene flat sheet membrane (Accurel PP 2EHF, nominal pore size 200 nm, overall porosity 70%) were from Membrana GmbH (Wuppertal, Germany). Polyvinyl alcohol (PVA, average Mw = 150,000 g/mol; 98.9% hydrolyzed, cod. 101302902), glutaraldehyde (GA, grade II, 25% in H_2O, cross-linker, Lot# MKBG3597V), poly (ethylene glycol) diglycidyl ether (PEDGE, average Mw = 500 g/mol, cross-linker, Lot# MKBL8500V), were from Sigma Aldrich. Iron oxide nanoparticles (average size of 7.403 ± 0.154 nm) were prepared with chemical precipitation technique [49]. Methanol and Hydrochloric acid were from Sigma Aldrich. Chicken hen egg white lysozyme (HEWL, cod. 62970, from Sigma-Aldrich) was dissolved in sodium acetate buffer (0.1 M, pH 4.6) at the initial concentration 40 mg mL^{-1}. Sodium Chloride (NaCl, 3.5.0 wt%, cod. 131659.1211, from Panreac), dissolved in the same buffer, was used as precipitant agent for HEWL. All chemicals were used as received and water purified with a Milli-Q system was used for all experiments. Various hydrogel composite membranes (Table 7) were prepared as described previously in chapter 2.2.4.

Table 7 Hydrogel composite membrane samples for protein crystallization test

Membrane samples	Polymer Concentration (w/v)	Cross linker (Type/amount)	Nanoparticles (amount)
PVA-PEDGE-NPs 0 %	PVA 8 %	PEDGE 3 wt. %	-
PVA-PEDGE-NPs 0.25 %	PVA 8 %	PEDGE 3 wt. %	Iron oxide III, 0.25 wt.%
PVA-PEDGE-NPs 1 %	PVA 8 %	PEDGE 3 wt. %	Iron oxide III, 1 wt.%
PVA-GA-NPs 0 %	PVA 8 %	GA 3 wt. %	-
PVA-GA-NPs 0.25 %	PVA 8 %	GA 3 wt. %	Iron oxide III, 0.25 wt.%
PVA-GA-NPs 1 %	PVA 8 %	GA 3 wt. %	Iron oxide III, 1 wt.%

3.3.3. Protein Crystallization Test

Hen egg white lysozyme is a well-studied and easy to crystallize protein, which is widely used by researchers as a model protein both for testing novel crystallization methods and for improving existing crystal growth approaches, as well as for analytical and theoretical studies on the fundamental principles of crystallization and protein crystals properties. In this study, Lysozyme solution at the initial concentration of 40 mg/mL was prepared in 0.1 M sodium acetate buffer pH 4.6. Reservoir solution of sodium chloride (3.5% w/v) was prepared in the same buffer and used as precipitant. Crystallization tests were carried out in two different configurations: (1) Hanging drop vapor diffusion method (using EasyXtal 15-Well Tools, Qiagen) and (2) Sitting drop (using 24-Well plates designed for membrane assisted crystallization). The setup used consisted of 10 μL (equal volumes of the protein sample and reservoir solution containing) drop placed on a glass cover-slide and membrane surface and stabilized over the reservoir solution of 500 mL. In the classical variant, the initial relation of precipitant concentration in the drop and in reservoir is 1:2, which during the equilibrium leads to the drop shrinking twice (because of water evaporation) and adequate increasing of its supersaturation. The crystallization tests were carried out at 20 °C with five replications for each condition to test the reproductively of the results. The membrane assisted crystallization setup designed by Di. Profio et al. [15] was used for protein crystallization tests. The schematic of experimental setup and mechanism of the crystallization system have been described in Figure 44.
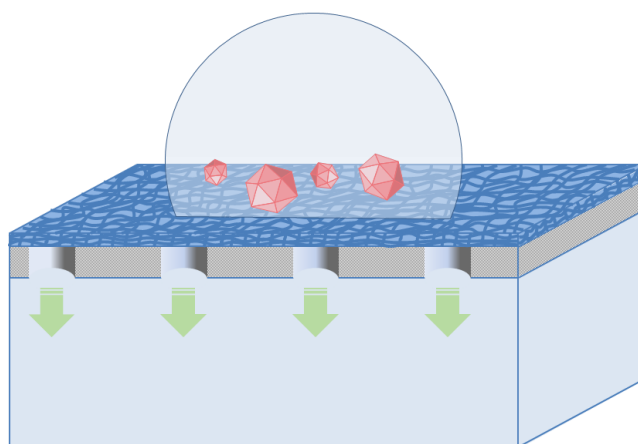
Figure 44 Experimental membrane assisted crystallization set up: a droplet of the protein solution sits on the hydrogel composite membrane, provides the physical contact with the reservoir solution, so only volatile solvent migrates in vapor phase through the pores of the substrate (HCM) from crystallizing solution towards the stripping solution under the action of driving force, as the protein solution concentrates inside the droplet, saturation allows nucleation and crystal growth [15]

3.3.4. Crystal Characterization

Protein crystals were observed under an optical microscope (DM 2500M, Leica Microsystems) equipped with a video camera.

3.3.5. Results and Discussion

Different HCMs have different surface wettability and different topographies as shown in Figure 45. Since different surface characteristics leads to a different heterogeneous crystallization behavior, the different topographies represented by the mean roughness depth leads to different energy barrier for heterogeneous nucleation. Besides the surface roughness of the material, the energy at the interface fluid/surface is a key factor in surface crystallization. With the water evaporation in the protein droplet, the vapor/liquid/solid contact line of the droplet presented different contraction pattern that was strongly dependent on the surface wettability. On HCMs without nanoparticles, the high surface hydrophilicity expressed by a low contact angle of the droplets, caused a wide spreading of solutes across the membrane surface, resulting in the absence of crystal formation. By introducing Iron oxide NPs in the hydrogel matrix, the hexagonal and tetragonal shapes of lysozyme crystals were formed on the surface, both of which were very typical and usual to be found in many lysozyme crystallization cases (Figure 50). An explanation could be that on such flat surface, protein molecules may adsorb onto the surface randomly and migrate over the surface until the first monolayer is established. Then the second layer grows slowly onto the first layer. During that assembling process, a few molecules in the adsorption layer may form small aggregates. When heterogeneous nucleation takes place on a rough surface, the hillocks on the surface may block the lateral migration of the adsorbed protein molecules, thus the protein molecules are trapped between the convex and concaves and are packed into a compact structure [146].

(a)
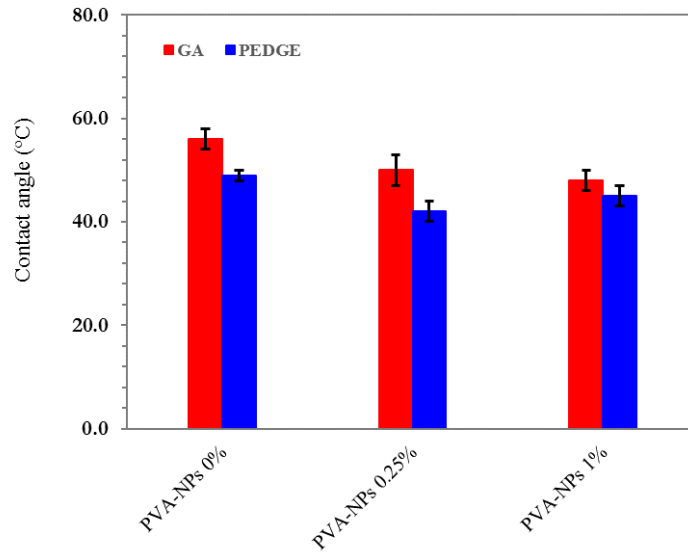
(b)
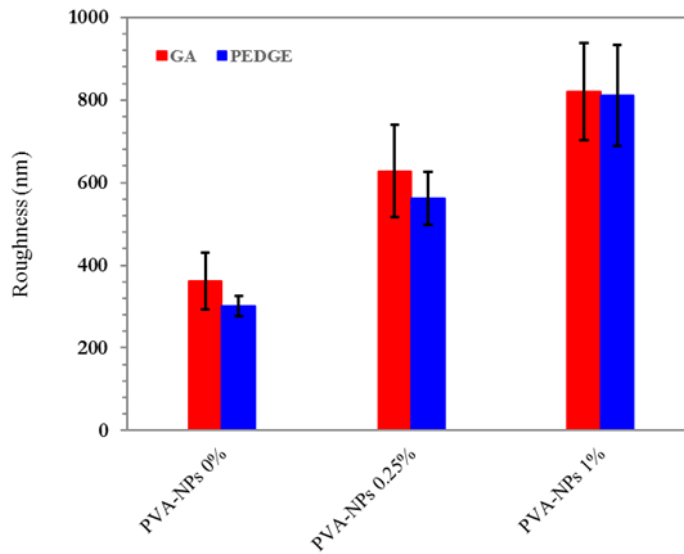
Figure 45 Different HCMs have different surface energies and different topographies: (a) Contact angle and (b) Roughness for different HCMS as a function of the amount of NPs in: PVA/GA HCMs (red) and PVA/PEDGE HCMs (blue).

Here, the probability for a nucleation event to occur within time t, was approximated by the fraction of micro-batch wells in which crystallization occurred within time t and the results have been shown in Figure 46 and demonstrated an increase the probability of nucleation and the

number density of the crystals by increasing the amount of NPs. It suggests that for HCMs, surface roughness promotes the formation of protein aggregates because, nanometric cavities generate the conditions for protein nucleation inside the cavities, as reported elsewhere in the literature, that material with a rough surface can trap protein molecules and encourage them to nucleate and form crystals [70].

(a)
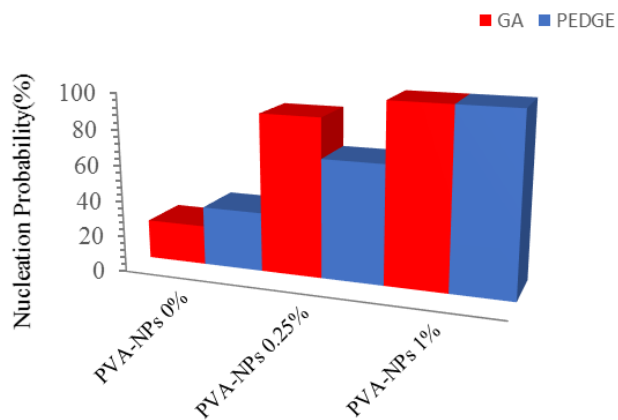
(b)
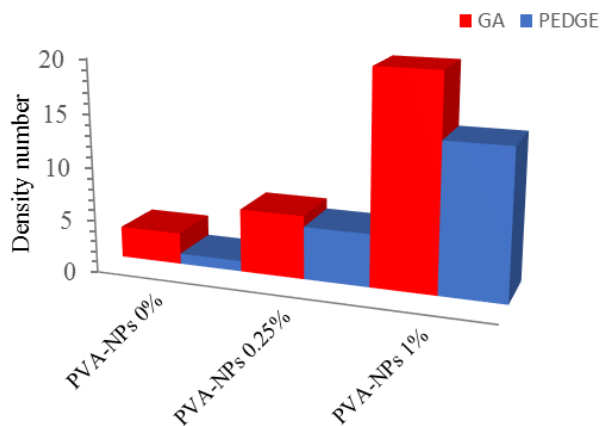
Figure 46 Increasing nucleation probability (a) and number density of the crystals (b) by increasing the amount of NPs

Since, the iron oxide nanoparticles, are randomly dispersed through the gel, they cannot induce the protein molecules to orient themselves in a specific pattern, as observed for randomly

dispersed NPs through the gel [71]. It can offer many different potential patterns of interaction with the crystal nuclei. It seems however, that the nanoparticles can pull together a sufficient number of those molecules in order to overcome the energy barrier for the first step of forming a precursor. It can be supported by the number density of the crystals observed.
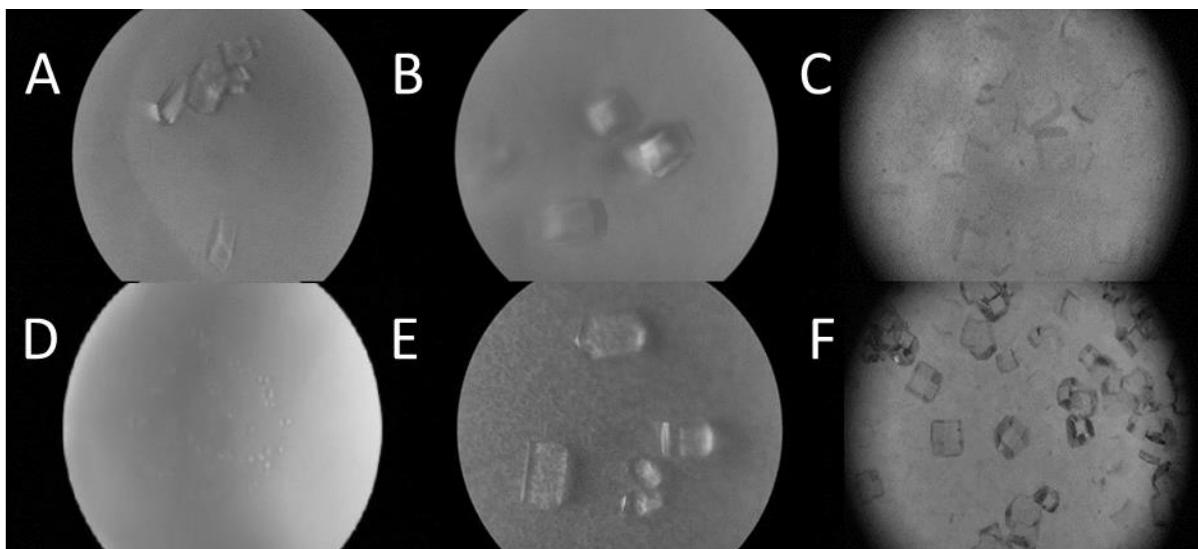
Figure 47 Crystal images: (A) PVA-PEDGE (B) PVA-PEDGE-NPs 0.25% (C) PVA-PEDGE-NPs 1% (D) PVA-GA (E) PVA-GA-NPs 0.25%. (F) PVA-GA-NPs 1%

As a proof of this concept, the results are compared with the theoretical analysis. Liu et al have developed a mathematical model ($\Delta G^*_{Het} / \Delta G^*_{HOM}$ ratio as a function of the contact angle on different roughness) for the rough surface [146]. In this model, the nucleating solution deposited on a rough surface is assumed to have a spherical cap shape as shown in Figure 46. The rough surface is assumed to be composed of a series of uniform cones. R is the main radius of the spherical cap, and r, h, and n are the radius, height, and number of cones, respectively.
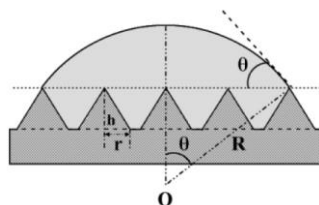
Figure 48 Geometry of a sphere-cap-shaped nucleating solution on a rough surface.

Where the geometrical relation have:

$$\alpha = {}^r/_R \tag{16}$$

$$\beta = {}^h/_R \tag{17}$$

When heterogeneous nucleation takes place on a smooth, perfectly planar and chemically homogeneous surface, the energy barrier to heterogeneous nucleation is given by:

$$\frac{\Delta G^*_{HET}}{\Delta G^*_{HOM}} = \left[\frac{1}{2} - \frac{3}{4}\cos\theta + \frac{1}{4}(\cos\theta)^3\right] \tag{18}$$

Hence, the energy barrier to heterogeneous nucleation taking place on a rough surface depends on the geometric structure and the number of the cones.

$$\frac{\Delta G^*_{HET}}{\Delta G^*_{HOM}}$$
$$= \frac{1}{4}\frac{[2(1 - \cos\theta) - \cos\theta\,(\sin\theta)^2]^3}{[(1 - \cos\theta)^2(2 + \cos\theta)3\beta(\sin\theta)^2 - n\alpha^2\beta]^2} \tag{19}$$

This model shows that the free energy barrier for heterogeneous nucleation increases with the contact angle for nucleating solution on the surface and decreases with increasing surface roughness, as shown in Figure 49.
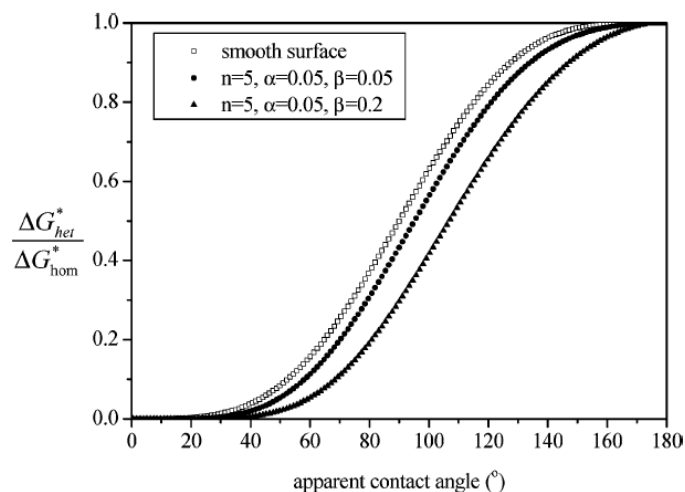
Figure 49 The $\Delta G^{*}_{Het}/\Delta G^{*}_{HOM}$ ratio as a function of the contact angle on different roughness [146]

Our result is consistent with as shown in Equation 19 and Figure 49. It is expected that the surface with irregular topography may pack molecules in different ways, and the resulting diversity in the bond angle for the protein molecules with its neighbours may increase the probability of nucleation as well. The resultant morphology (shape and size) of the lysozyme crystals formed on the rougher surface was also maintained to the same level or even more as that obtained in conventional methods. The crystal size is obviously larger and the number of crystals grown is much lower which is preferable. This is an advantage, because we desire one or few crystals, rather than many.
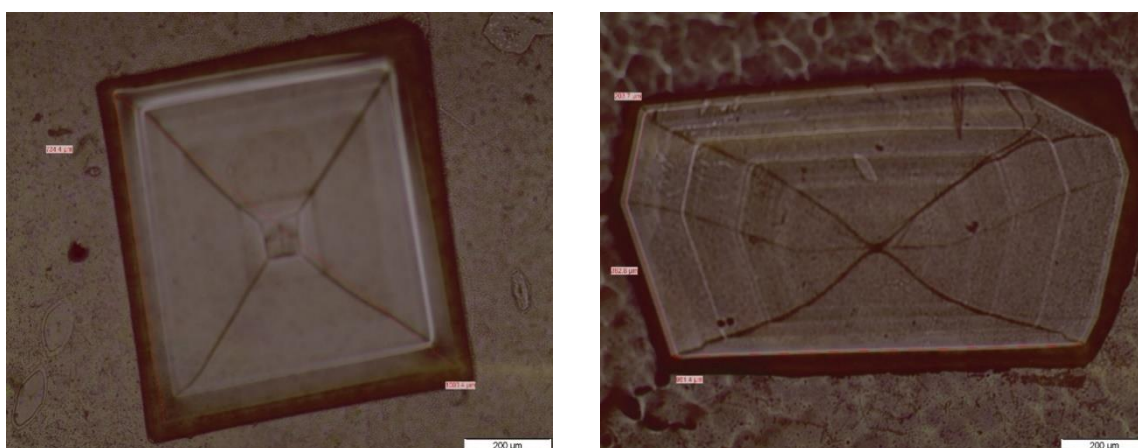
Figure 50 Crystal images: (a) PVA-GA-NPs 1%, (b) PVA-PEDGE-NPs 1%

3.3.6. Conclusions

To create an environment that favours nucleation, the use of nucleation inducing surface has become more common. The presence of a surface microstructure i.e. roughness or porosity might facilitate nucleation. Because physical entrapment of solute molecules inside the cavities allows solute concentration up to the required level of supersaturation able to promote nucleation. Different surface characteristics lead to a different heterogeneous crystallization behaviour. From the theoretical analysis, the energetic barrier to heterogeneous nucleation is found to increase at higher contact angles and to decrease at higher roughness. In the current work, we performed several lysozyme crystallization experiments on a series of functional membranes with tailored surface patterning, with the aim of examining their influences on the heterogeneous nucleation of lysozyme crystals. Based on the contact angle and roughness measurements, it was found that surface structural characteristics in addition to chemical and physical interactions between the surfaces and protein molecules as reported in the literature, have influence on the heterogeneous nucleation of protein crystals to different extents. We demonstrated that surface roughness promotes protein crystallization, potentially due to the increase of local protein concentration at rougher surfaces. It can be supported by the number density of the crystals observed. On hydrogel composite membranes without any NPs, the surface hydrophilicity induced a low contact angle of the droplets and wide spread of the droplets across the surface was observed. By introducing NPs in the hydrogel matrix, the hexagonal and tetragonal shapes of lysozyme crystals were formed. The crystal size was obviously larger and the number of crystals grown was mostly much.

Chapter IV:

Modeling of Membrane Crystallization Process

4.1. Introduction

In membrane crystallization process, the hydrophobic porous membranes present both as a mass transfer apparatus to concentrate crystallizing solutions by solvent removal in vapor phase and as active surfaces to promote heterogeneous nucleation. The transmembrane distillation of solvent from saturated solution is used to reach supersaturation in the crystallizing solution. Direct contact membrane distillation is the simplest MD configuration, and is the most widely used in laboratory research. In this configuration (Figure 51), both the aqueous feed and permeate are in direct contact with the surface of a membrane and the temperature difference across the membrane provides the driving force to generate transmembrane flux. Depending on the chemical and physical properties of the membrane and the process parameters (concentration, temperature, flowrate, etc.) the solvent evaporation, hence, supersaturation degree and supersaturation rate, can be regulated very precisely [9-12].
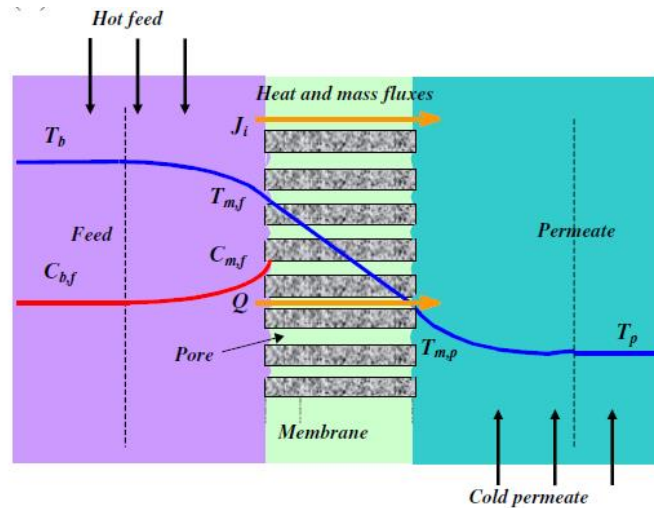
Figure 51 Schema of direct contact membrane distillation: C_{bf}, bulk concentration and C_{mf}, concentration close to the membrane surface in the fid side; T_b, bulk temperature and T_{mf}, temperature close to the membrane surface in the feed side; T_p, bulk temperature and T_{mp}, temperature close to the membrane surface in the permeate side; J, transmembrane flux and Q, heat flux.

Like other membrane process, the temperature and concentration polarization leads the temperature and concentration at the membrane surface to differ from the bulk temperature measured in the feed and in the permeate and performs as the heat and mass transfer resistance in

the conventional membrane distillation. While, the highly concentrated region near the membrane interface is an ideal nucleation promoting circumstance in the crystallization process [8]. The high potential of MCr to control the generation of supersaturation has been reported by many authors, but they have also concluded that fouling of the membrane needs to be prevented for successful operation [148]. Fouling of the membrane induces a decline in flux which is proportional to the blocked membrane surface. Furthermore, excessive fouling has shown to reduce the long-term stability of membranes, and to induce the membrane wetting because of salt deposition inside the pores. Generally, the design of membrane processes is aimed at minimizing scaling and polarization effects. In MCr process, to avoid scaling and crystal deposition on membrane surface, one strategy is to induce nucleation and crystal growth in separate sites, thus reducing the risk of membrane fouling even when the same membrane supports heterogeneous nucleation [9]. However, several studies claim to utilize the membrane as a template to induce heterogeneous nucleation. In this case, the crystallization takes place directly in the membrane module where the supersaturation is generated [13, 149-151]. In recent years, large studies on design of membrane crystallization process reported in the literature, are dedicated to the influence of the operating parameters and membrane properties, on the scaling and fouling. Since simultaneous crystallization and separation occur in MCr, it is important to optimize operating conditions to minimize fouling by scaling and maximize water production. In MCr process, crystallization due to the homogenous nucleation (HOM) occurs in the bulk solution. In addition, the presence of membrane and localized concentration polarization in boundary layer, near to the membrane surface, lowers the energy barrier for nucleation and promotes heterogeneous nucleation (HET). The homogenous nucleation and crystallization in the bulk solution is desirable as heterogeneous nucleation and deposition of crystals on membrane surface due to the blockage of the membrane pores and altering the surface hydrophobicity is undesirable. In the studies that attempted to improve feed agitation near the feed side of the membrane, strategies such as the introduction of baffles and spacer, vibration and aeration have been investigated to overcome temperature polarization, concentration polarization and fouling in membrane [152]. In several studies, the effect of the operating conditions on mechanisms of membrane fouling due to scale formation in MCr was investigated. The effects of feed temperature variation on the MCr performance in terms of membrane flux has shown that increasing feed temperature increases membrane flux but the flux declines rapidly with time at higher feed temperatures due to the occurrences of membrane

scaling and salt oversaturation at the boundary layer facilitated wetting. To prevent salt oversaturation, the critical fluxes have been calculated and by keeping the membrane flux lower than the critical flux, thus a stable membrane performance during a continuous MCr operation has been achieved. In addition, study the effect of flow rate on flux decline and crystallization has demonstrated that the intermediate flow rate results the lowest fouling propensity. At low flow rates, flux decline occurs by both surface and bulk crystallization. At high flow rates, the bulk crystallization becomes more important due to the occurrence of secondary nucleation [23, 153]. But the further application of the membrane crystallization process needs the establishment of process model which describes both processes of membrane distillation and crystallization. This model should involve the evaluation of the influencing mechanism of the operational conditions (feed flow rate and feed concentration, temperature and pressure gradient across the membrane, and so forth) and the influence of polarization phenomenon to the supersaturation distribution on the membrane interface. On the other word, the model should reveal how the membrane property and membrane distillation condition accelerate the heterogeneous nucleation process, and provide the approach to evaluate the impact of membrane promoting nucleation on the final crystal size distribution (CSD) in the bulk solution. The general problem of modeling combining mass transfer by diffusion or convection mechanism, and chemical reaction leading to solid formation is a major challenge. In the studies on the modeling of MCr, the authors presented a comprehensive mathematical model for the design of membrane distillation processes on the base of balance equations [154, 155]. Therefore, a complex relationship between the mass and heat transferred through the membrane must be solved to provide an approximate reference point for the design of a driver module and process. However, important aspects of the MCr process need further consideration for the achievement of an effective design. One aspect concerns the possibility of pore blockage due to crystal deposition on the microporous membrane surface, which is regarded as the main factor to cause permeability deterioration in MCr applications. Also, it should be stressed that the crystal formation phenomena are not included in this equation set, because, the objective was first to evaluate temperature and concentration profiles in the MD, to identify the locations of crystal formation zones. Therefore, another important aspect which should be considered in the mass and heat balance equations, is the interactions between the fluid and crystals in the bulk and membrane surfaces [156].

The main goal of this study was to develop general predictive model of membrane crystallization process. The membrane distillation module (plate and frame arrangement) was implemented to investigate the proposed process. The development of this model involves the fundamental theories and models in membrane process and crystallization engineering, especially the models described the mass and heat transfers in membrane module and the crystal size distribution determined by both nucleation and crystal growth processes. Thus, first, the supersaturate conditions in the membrane module should be simulated on the base of balance equations. Then the promoting nucleation rate is defined by the classic nucleation and growth theories. The relevant kinetic variables are then introduced to the population balance equation and mass balance equation. The methodology contains:

I.   Derivation of mathematical model based on different assumptions, balance equations describing the processes going through the direct contact membrane distillation crystallization in plate and frame configuration;

II.   Program development.

III. Verification of model verification of model

In this work, only the equations were derived and reported (First step). The process is divided into:

i)   The population balance equation and material balance in the membrane module and the feed tank

ii)   The vapor-liquid equilibrium section (Mathematical equations describing this part of the process is developed based on Antoine equation and activity coefficients)

iii) The mass transfer section (Mathematical equations describing this part of the process are developed based on boundary value theory on feed site and permeate site and the dusty gas model for the mass transport through the membrane)

iv)   The heat transfer section (The equations are based on heat transfer coefficients and temperature boundary conditions)

The assumptions are described as:

i)   The composition and temperature of liquid changes with axial coordinate (x)

ii)   The impact of membrane in the model is described by considering the membrane as heterogeneous system (nucleation process in bulk solution is homogenous nucleation and the nucleation process on the membrane surface membrane is heterogeneous)

iii)   The population balance equation to describe the evolution of the crystal size distribution during time in a process of crystallization assumes that neither agglomeration nor breakage occurs and the expression of growth rate is independent of crystal size.

4.2. Population Balance Equation (PBE)

Population balances are used in several branches of modern science, mainly concerning particulate processes such as crystallization, aerosol engineering and polymer technology. PBEs define how populations of separate entities develop in specific properties over time. Consider the average number of particles with particle properties denoted by a particle state vector (L, x) (where L corresponds to particle properties like size, density, etc. also known as internal coordinates and x corresponds to spatial position or external coordinates) dispersed in a continuous phase defined by a phase vector Y (x, t) (which again is a function of all such vectors which denote the phase properties at various locations) is denoted by f (L, x, t). Hence, it gives the particle characteristics in property and space domains. Let h (L, x, Y, t) denote the birth rate of particles per unit volume of particle state space, so the number conservation can be written as

$$\frac{d}{dt} \int dV_L \int dV_x f(L, x, t) = \int dV_L \int dV_x . h(L, x, Y. t)$$

(20)

This is a generalized form of PBE [157].

4.2.1. Population balance equation in a batch crystallizer

The formulation of population balances in the case of crystallization is based on the number density of crystals formed during crystallization, i.e. n (L, t). In the case of a perfectly mixed batch crystallizer, with constant suspension volume and assuming size-independent growth the PBE reads as:

$$\frac{\partial n(L,t)}{\partial t} + G(t)\frac{\partial n(L,t)}{\partial L} = B - D$$

(21)

Where L is the particle size, t is the time, n is the number density of crystals, i.e. its particle size distribution (PSD), and G denotes the crystal growth rate. B and D are the birth and death of particles occur due to breakage and aggregation processes. The solute material balance, which defines the solute concentration, c (t), is written as:

$$\frac{dc}{dt} = -3k_v\rho_p \int_0^\infty G.n.L^2 dL$$

(22)

Where k_v and ρ_p denote the volume shape factor and the particle density, respectively. The following initial and boundary conditions apply to the PBE and to the material balance equation:

$$n(0, L) = n_0(L)$$

$$n(t, 0) = \frac{J}{G}$$

$$c(0) = c_0$$

Where J is the nucleation rate and c_0 and $n_0(L)$ denote the initial solute concentration and the initial particle size distribution, respectively. The supersaturation, $S(t)$ is defined as:

$$S = {}^c/_{c^*}$$

(23)

With c^* being the solubility. Combined with proper nucleation and growth rate expressions, a population balance equation based model allows for the calculation of the solute and solid concentrations and the particle size distribution over time. Several approaches exist to express the nucleation, growth and dissolution rates as a function of the process variables, e.g. the supersaturation, temperature or suspension density. These expressions are often first principle expressions based on a specific mechanism, e.g. the birth-and-spread and screw dislocation mechanisms. In this work however, the objective was not to reveal these mechanisms but to obtain a descriptive process model that could be used to predict the evolution of the solute and solid concentrations and the particle size distribution over time. For this reason, relatively simple empirical expressions have been used in most cases to describe the nucleation, growth and kinetics

Nucleation kinetics: Nucleation phenomena, i.e. the formation of crystals from a liquid phase, can be divided into primary and secondary nucleation phenomena. Primary nucleation takes place in the absence of crystals and can be subdivided into homogeneous, in the absence of any foreign particles such as dust, and heterogeneous, in the presence of facilitating foreign particles, nucleation. According to the classical nucleation theory (CNT), the nucleation rate J $[m^{-3}s^{-1}]$ for homogeneous nucleation can be expressed as [22]

$$J = A \exp(\frac{-B}{\ln S^2})$$

(24)

In this equation, $A[m^{-3}S^{-1}]$ and $B[unitless]$ are kinetic parameters and S is the supersaturation ratio. The pre-exponential kinetic parameter for homogeneous nucleation A_{HOM} can be estimated from the following equations per the mechanism of solute transport in solution: $A_{HOM,D}$ for volume diffusion control and $A_{HOM,I}$ for interface transfer control.

$$A_{HOM,D} = \left(\frac{k_B T}{v_0 \gamma}\right)^{1/2} DC^* N_a \ln S$$

(25)

$$A_{HOM,I} = \left(\frac{4\pi}{3v_0}\right)^{1/3} \left(\frac{\gamma}{k_B T}\right)^{1/2} DC^* N_a$$

(26)

Where, γ $[J\ m^{-2}]$ is the interfacial energy , v_0 $[m^3]$ the molecular volume of the solute, $k_B [J\ K^{-1}]$ the Boltzmann constant, $T[K]$ the absolute Temperature, N_a Avogadro number and D is the diffusion coefficient. The molecular volume of the solute v_0 $[m^3]$ and the interfacial energy are calculated by

$$v_0 = M/\rho_p N_a$$
(27)

$$\gamma = B k_B T \left(\frac{1}{v_0}\right)^{2/3} \ln \frac{1}{v_0 C^* N_a}$$
(28)

According to the equation above, the nucleation rate is thus a function of pre-exponential factor, which depends on the fluid dynamics in the system, the interfacial energy and the supersaturation. In static crystallization equipment, it is assumed that the controlling transport mechanism is the diffusion of solute from the bulk solution to the growing aggregate. In dynamic crystallization equipment, it is considered the dominate transport mechanism is interface transfer control. Typically, $A_{HOM} \sim 10^{35}$ $[m^{-3}s^{-1}]$. Also, the coefficient B can be expressed as follow:

$$B = \frac{16\pi\gamma^3 v_0^2}{3(k_B T)^3}$$
(29)

In the presence of a heterogeneous surface in the supersaturated solution, the apparent interfacial energy γ decreases. In this case, the nucleation barrier is smaller and heterogeneous nucleation will start at lower supersaturation level compared to homogeneous nucleation. For heterogeneous nucleation, the effective interfacial energy becomes, $\gamma_{eff} = \emptyset\gamma$ with $0 < \emptyset < 1$, so that the term of B in eq. 29 can be smaller than for homogeneous nucleation. In the case of an ideal smooth surface, can be evaluated by:

$$\emptyset = \frac{1}{4}(2 + \cos\theta)(1 - \cos\theta)^2$$
(30)

Where, θ is the contact angle between the mother solution and the solid substrate. In the case of heterogeneous nucleation induced by a porous membrane surface, this equation can be used:

$$\emptyset_{por} = \frac{1}{4}(2 + \cos\theta)(1 - \cos\theta)^2 \left[1 - \varepsilon \frac{(1 + \cos\theta)^2}{(1 - \cos\theta)^2}\right]^3$$

(31)

With ε is the surface porosity [23].

Growth kinetics: Crystal growth in a supersaturated solution is a complex process that can be summarized with consecutive diffusion and integration steps following the approach of diffusion and reaction used in chemical reaction engineering. Consequently, crystal growth can be either diffusion limited or integration controlled. In this work, only integration controlled crystal growth will be considered. Generally, the linear growth rate G $[m.s^{-1}]$ is defined as the change of a characteristic crystal dimension per unit time:

$$G = \frac{dL}{dt}$$

(32)

Where L denotes the characteristic length of the crystal and t is the time. The kinetics of crystal growth is expressed by:

$$G = k_g S^g$$

(33)

Where k_g and g are kinetic parameters to be identified and S is the supersaturation ratio [22].

4.2.2. Population balance equation in membrane module

Unlike a perfectly mixed batch crystallizer, in direct contact membrane distillation module, there is the concentration and temperature distribution inside the module and the variation in T, C and CSD, should be considered as a function of spatial position or external coordinates (x, y and z). In this work, we assume the concentration, temperature and the crystal size distribution change with axial coordinate (x) only.

4.2.2.1. Population balance equation on feed side:

By considering a differential volume element, ΔV_R along the length of the module on the feed side, there will be three sections: liquid ΔV, solid particles in the liquid ΔV_p and solid particles on the surface of the membrane ΔV_s as illustrated in Figure 52.
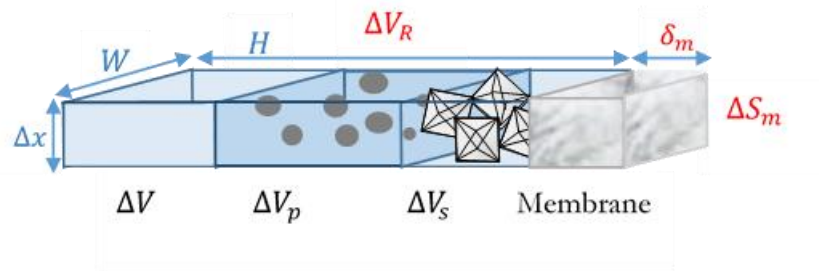

Figure 52 Differential volume element ΔV_R along the length of the module on the feed side and surface element ΔS_m on the membrane surface

For the balanced element in external and internal coordinates (x, L) as shown in Figure 53, the PBE, $n(x, L, t)$ can be written as
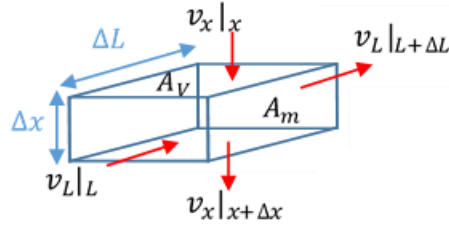
Figure 53 Balanced element on the feed site

$n. A_F. \Delta x. \Delta L|_{\tau+\Delta\tau}$

$$= n. A_F. \Delta x. \Delta L|_\tau + v_x. n. A_F. \Delta L|_x. \Delta\tau - v_x. n. A_F. \Delta L|_{x+\Delta x}. \Delta\tau$$

$$+ v_L. n. A_F. \Delta x|_L. \Delta\tau - v_L. n. A_F. \Delta x|_{L+\Delta L} + A_F. \Delta x. \Delta L. \Delta\tau(r_{v,B} - r_{v,D})$$

$$+ {A_m}/{L_m}. \Delta x. \Delta L. \Delta\tau. r_{s,D}^*$$

Where $r_{v,B}$ and $r_{v,D}$ are the birth rate and the death rate of particles respectively, $r_{s,D}^*$ is the transfer rate of non-sticking particles from the membrane surface to the interface. Rewrite the equation and divide by $\Delta x. \Delta L. \Delta\tau$:

$$\frac{n. A_F. \Delta x. \Delta L|_{\tau+\Delta\tau} - n. A_F. \Delta x. \Delta L|_\tau}{\Delta\tau}$$

$$= -\frac{v_x. n. A_F. \Delta L|_{x+\Delta x}. \Delta\tau - v_x. n. A_F. \Delta L|_x. \Delta\tau}{\Delta x}$$

$$-\frac{v_L. n. A_F. \Delta x|_{L+\Delta L}. \Delta\tau - v_L. n. A_F. \Delta x|_L. \Delta\tau}{\Delta L} + A_F. (r_{v,B} - r_{v,D}) + {A_m}/{L_m}. r_{s,D}^*$$

And finally, it can be written

$$\frac{\partial(A_F. n)}{\partial\tau} + \frac{\partial(v_x. n. A_F)}{\partial x} + \frac{\partial(v_L. n. A_F)}{\partial L} = A_F. (r_{v,B} - r_{v,D}) + {A_m}/{L_m}. r_{s,D}^*$$

A_R is the cross section of the element ΔV_R and A_m is the membrane surface area, A_F is described as the cross section of the element ΔV_R for liquid phase and can be calculated,

$$A_F = A_R\left(1 - \varepsilon_p - \varepsilon_s\right)$$

And

$$\Delta V_F = \Delta V_R\left(1 - \varepsilon_p - \varepsilon_s\right)$$

Here, ε_p and ε_s are particles volume fraction in the mother liquid (interface) and on the surface of the membrane respectively

$$\varepsilon_p = \frac{\Delta V_{P,R}}{\Delta V_R}$$

$$\varepsilon_s = \frac{\Delta V_{P,S}}{\Delta V_R}$$

And they can be driven as follow

$$\varepsilon_p = \frac{\Delta V_{P,R}}{\Delta V_R} = \frac{\Delta V_F \cdot k_v \cdot \int_0^\infty n \cdot L^3 \, dL}{\Delta V_R} =$$

$$\frac{\Delta V_R\left(1 - \varepsilon_p - \varepsilon_s\right) \cdot k_v \cdot \int_0^\infty n \cdot L^3 \, dL}{\Delta V_R} =$$

$$\left(1 - \varepsilon_p - \varepsilon_s\right) \cdot k_v \cdot \int_0^\infty n \cdot L^3 \, dL$$

Therefore ε_p is obtained as

$$\varepsilon_p = \frac{\left(1 - \varepsilon_s\right) \cdot k_v \cdot \int_0^\infty n \cdot L^3 \, dL}{1 + k_v \cdot \int_0^\infty n \cdot L^3 \, dL}$$

And ε_s is obtained

$$\varepsilon_s = \frac{\Delta V_{P,S}}{\Delta V_R} = \frac{{A_m}/{V_R} \cdot \Delta V_R \cdot k_v \cdot \int_0^\infty n.\,L^3\,dL}{\Delta V_R} = {A_m}/{V_R} \cdot k_v \cdot \int_0^\infty n.\,L^3\,dL$$

In the PBE, v_L is the linear velocity of crystal growth and can be replaced by the general term of growth rate G and v_x is the velocity of the feed flow that is calculated by

$$v_x = \frac{\dot{v}}{A_R\left(1 - \varepsilon_p - \varepsilon_s\right)}$$

Rewrite and substitution the terms of v_L and v_x by G and $\dot{v}$, the PBE on feed side in the solution is driven

$$\frac{\partial\left(\left(1 - \varepsilon_p - \varepsilon_s\right).n\right)}{\partial \tau} + \frac{1}{A_R} \cdot \frac{\partial(\dot{v}.n)}{\partial x} + \frac{\partial\left(G.n.\left(1 - \varepsilon_p - \varepsilon_s\right)\right)}{\partial L}$$
$$= \left(1 - \varepsilon_p - \varepsilon_s\right).\left(r_{v,B} - r_{v,D}\right) + {A_m}/{A_R.L_m} \cdot r_{s,D}^*$$

4.2.2.2. Population balance equation on membrane surface

By considering a differential element of surface, ΔS_m on the membrane surface shown in Figure 54, the PBE $n_s(x, L, t)$ for a balanced element on the membrane surface in external and internal coordinates as illustrated in Figure 54 will be written as
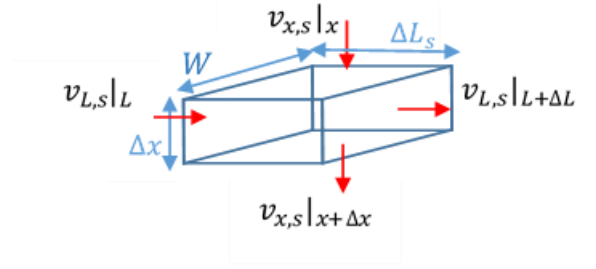
Figure 54 Balanced element on the membrane surface

$$n_s.W.\Delta x.\Delta L_s|_{\tau+\Delta\tau}$$

$$= n_s.W.\Delta x.\Delta L_s|_\tau + v_{x,s}.n_s.W.\Delta L_s|_x.\Delta\tau - v_{x,s}.n_s.W.\Delta L_s|_{x+\Delta x}.\Delta\tau$$

$$+ v_{L,s}.n_s.W.\Delta x|_L.\Delta\tau - v_{L,s}.n_s.W.\Delta x|_{L+\Delta L}.\Delta\tau + W.\Delta x.\Delta L_s.\Delta\tau.(r_{s,B} - r_{s,D})$$

$$- W.\Delta x.\Delta L_x.\Delta\tau.r_{s,D}^*$$

Rewrite the equation and divide by $W.\Delta x.\Delta L_s.\Delta\tau$:

$$\frac{n_s|_{\tau+\Delta\tau} - n_s|_\tau}{\Delta\tau} = -\frac{v_{x,s}.n_s|_{x+\Delta x} - v_{x,s}.n_s|_x}{\Delta x} - \frac{v_{L,s}.n_s|_{L+\Delta L} - v_{L,s}.n_s|_L}{\Delta L} + r_{s,B} - r_{s,D} - r_{s,D}^*$$

And finally, it can be written

$$\frac{\partial n_s}{\partial\tau} = -\frac{\partial(v_x.n_s)}{\partial x} - \frac{\partial(v_{L,s}.n_s)}{\partial L} + r_{s,B} - r_{s,D} - r_{s,D}^*$$

In the PBE, $v_{L,s}$ is the linear velocity of crystal growth on the membrane surface and can be replaced by the general term of growth rate G_s and $v_{x,s}$ is zero because on the surface because there is no transfer for sticking particles to the membrane surface, therefore the PBE is driven as

$$\frac{\partial n_s}{\partial\tau} = -\frac{\partial(G_s.n_s)}{\partial L} + r_{s,B} - r_{s,D} - r_{s,D}^*$$

102

4.3. Mass Balance Equations

4.3.1. Component mass balance on feed side (element ΔV_R)

For the differential element ΔV_R along the length of the membrane module on the feed side, we consider three sections: liquid ΔV, solid particles in the liquid ΔV_p and solid particles on the surface of the membrane ΔV_s as illustrated in Figure 55 and the mass balance of component i for the element ΔV_R is written as
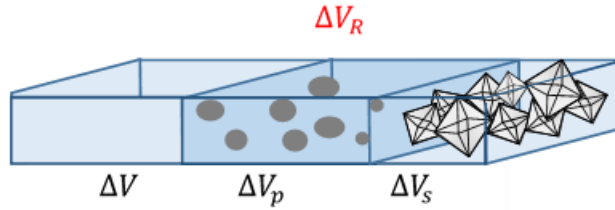

Figure 55 Differential element ΔV_R along the length of the membrane module on the feed side

$$A_F.\Delta x.C_i|_{\tau+\Delta\tau} + A_F.\Delta x.m_{i,p}|_{\tau+\Delta\tau} + {^{A_m}}\!/_{V_R}.A_R.\Delta x.m_{i,s}|_{\tau+\Delta\tau}$$

$$= A_F.\Delta x.C_i|_{\tau} + A_F.\Delta x.m_{i,p}|_{\tau} + {^{A_m}}\!/_{V_R}.A_R.\Delta x.m_{i,s}|_{\tau} + \dot{v}.C_i.\Delta\tau|_x$$

$$- \dot{v}.C_i.\Delta\tau|_{x+\Delta x} + \dot{v}.m_{i,p}.\Delta\tau|_x - \dot{v}.m_{i,p}.\Delta\tau|_{x+\Delta x} + M_i \sum_j \tilde{r}_j \tilde{v}_{i,j}.A_F.\Delta x.\Delta\tau$$

$$- J_{i,m}.{^{A_m}}\!/_{V_R}.A_R.\Delta x.\Delta\tau$$

Where $m_{i,p}$ and $m_{i,s}$ are the concentration of component i present in solid phase and expressed as kg of component i in m^3 of solid free liquid. A_R , and A_m are the cross section of the membrane module and the membrane surface respectively. A_F, is the cross section for liquid phase as described before. Rewrite the equation and divide by $\Delta x.\Delta\tau$:

$$\frac{A_F.C_i|_{\tau+\Delta\tau} - A_F.C_i|_\tau}{\Delta\tau} + \frac{A_F.m_{i,p}|_{\tau+\Delta\tau} - A_F.m_{i,p}|_\tau}{\Delta\tau} + {^{A_m}/_{V_R}}.A_R.\frac{m_{i,s}|_{\tau+\Delta\tau} - m_{i,s}|_\tau}{\Delta\tau}$$

$$= \frac{\dot{v}.C_i|_x - \dot{v}.C_i|_{x+\Delta x}}{\Delta x} + \frac{\dot{v}.m_{i,p}|_x - \dot{v}.m_{i,p}|_{x+\Delta x}}{\Delta x} + M_i \sum_j \tilde{r}_j \tilde{v}_{i,j}.A_F$$

$$- J_{i,m}.{^{A_m}/_{V_R}}.A_R$$

And finally, the equation for the mass balance of component i is obtained as

$$\frac{\partial(A_F.C_i)}{\partial\tau} + \frac{\partial(A_F.m_{i,p})}{\partial\tau} + {^{A_m}/_{V_R}}.A_R.\frac{\partial(A_F.m_{i,s})}{\partial\tau}$$

$$= -\frac{\partial(\dot{v}.C_i)}{\partial x} - \frac{\partial(\dot{v}.m_{i,p})}{\partial x} + M_i \sum_j \tilde{r}_j \tilde{v}_{i,j}.A_F - J_{i,m}.{^{A_m}/_{V_R}}.A_R$$

4.3.1.1. Component mass balance for element ΔV_p (solid particles in the liquid)

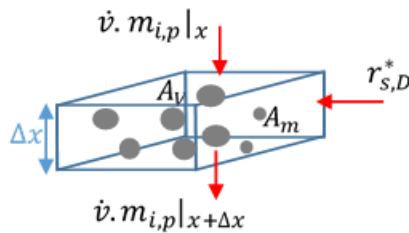The mass balance of component i for the element ΔV_p shown in Figure 56 can be written

Figure 56 Component mass balance on the element ΔV_p

$$A_F . \Delta x . m_{i,p}|_{\tau+\Delta\tau} = A_F . \Delta x . m_{i,p}|_\tau + \dot{v}. m_{i,p}. \Delta\tau|_x - \dot{v}. m_{i,p}. \Delta\tau|_{x+\Delta x} +$$

$$A_F . \Delta x . \Delta\tau . w_{i,p}. \rho_p. k_v \int_0^\infty (r_{v,B} - r_{v,D}) L^3 dL + {A_m}/{V_R} . A_R . \Delta x . \Delta\tau . w_{i,p}. \rho_p. k_v \int_0^\infty r_{s,D}^* L^3 dL +$$

$$3 A_F . \Delta x . \Delta\tau . w_{i,p}. \rho_p. k_v \int_0^\infty G. n . L^2 dL$$

Where $r_{v,B}$ and $r_{v,D}$ are the birth rate and the death rate of particles respectively, $r_{s,D}^*$ is the transfer rate of non-sticking particles from the membrane surface to the interface and G is the growth rate of the particles. Then, the equation can be written

$$\frac{\partial(A_F . m_{i,p})}{\partial\tau} = -\frac{\partial(\dot{v}. m_{i,p})}{\partial x} + A_F . w_{i,p}. \rho_p. k_v \int_0^\infty (r_{v,B} - r_{v,D}) L^3 dL$$

$$+ {A_m}/{V_R} . A_R . w_{i,p}. \rho_p. k_v \int_0^\infty r_{s,D}^* L^3 dL + A_F . w_{i,p}. \rho_p. 3 k_v \int_0^\infty G. n . L^2 dL$$

4.3.1.2. Component mass balance for element ΔV_s (solid particles sticking to the surface of the membrane)

The mass balance of component i for the element ΔV_s solid particles sticking to the surface of the membrane) as shown in Figure 57 can be written
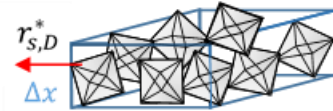

Figure 57 Component mass balance on the element ΔV_s

$$^{A_m}/_{V_R}.A_R.\Delta x.m_{i,s}|_{\tau+\Delta\tau}$$

$$= {^{A_m}/_{V_R}}.A_R.\Delta x.m_{i,s}|_\tau + {^{A_m}/_{V_R}}.A_R.\Delta x.\Delta\tau.w_{i,p}.\rho_p.k_v \int_0^\infty (r_{s,B} - r_{s,D})L^3 dL$$

$$- {^{A_m}/_{V_R}}.A_R.\Delta x.\Delta\tau.w_{i,p}.\rho_p.k_v \int_0^\infty r_{s,D}^* L^3 dL$$

$$+ {^{A_m}/_{V_R}}.A_R.\Delta x.\Delta\tau.w_{i,p}.\rho_p.3k_v \int_0^\infty G_s.n_s.L^2 dL$$

Where $r_{s,B}$ and $r_{s,D}$ are the birth rate and the death rate of particles on the membrane surface respectively (heterogeneous nucleation), $r_{s,D}^*$ is the transfer rate of non-sticking particles from the membrane surface to the interface and G_s is the growth rate of the particles on the surface. Then, the equation cab be written as

$$\frac{\partial(A_F.m_{i,s})}{\partial\tau} = w_{i,p}.\rho_p.k_v \left[\int_0^\infty (r_{s,B} - r_{s,D} - r_{s,D}^*)L^3 dL + 3\int_0^\infty G_s.n_s.L^2 dL \right]$$

4.3.2. Mass transfer through the membrane

The "Dusty Gas Model (DGM)" can be used to model multicomponent gaseous transport through porous media. Based on the DGM, the mass transfer resistances are represented with the electric analogy in Figure 58.
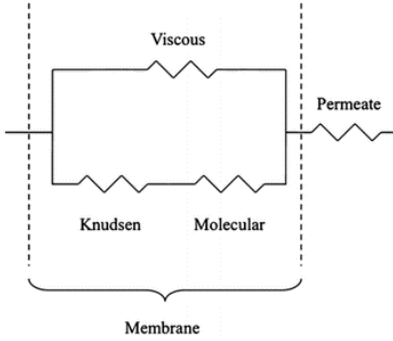
Figure 58 The electric analogy the mass transfer resistances

The DGM equation is given,

$$-\frac{1}{RT}\nabla p_i = \sum_{j=1,j\neq i}^{n} \frac{y_j.N_i - y_i.N_j}{D_{i,j}^e} + \frac{N_i}{D_{k,i}^e} + \frac{y_i.B.P}{k,i.\mu_g.RT}\nabla P$$

Appropriate contributions to mass transfer coefficient are deducted from Knudsen number analysis: $D_k = \lambda/d$, where λ is the mean free path of molecules and d the pore diameter.

4.3.3. Mass balance at liquid membrane interface to identify $j_{i,m}$

Mass transfer through the membrane is calculated as mass transfer through the interface (boundary layer, Figure 59) plus change of the weight on the membrane surface due to the birth and death of new particles as well as particle growth on the membrane surface and the transfer of non-sticking particles from the membrane surface to the bulk as follow:
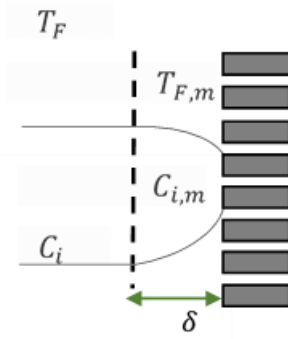
Figure 59 boundary layer on feed site

$$j_{i,m} = j_i - w_{i,p}.\rho_p.k_v \left[\int_0^\infty (r_{v,B} - r_{v,D} + r_{s,D}^*)L^3 dL + 3 \int_0^\infty G_s.n_s.L^2 dL \right]$$

First it is needed to calculate mass transfer through the interface (boundary layer). Per film theory, the mass flux through the interface is described by convection-diffusion equation;

$$j_i = -D_i \left. \frac{dc_i}{dz} \right/ + v_z.c_i$$

The pseudo-steady state flow analysis can be applied,

$$\frac{dj_i}{dz} = 0$$

Assuming the diffusion coefficient and velocity to be a constant, the equation will be rewrite as following

$$-D_i \frac{d^2 c_i}{dz^2} + v_z \frac{dc_i}{dz} = 0$$

The boundary conditions at the interface are

$$z = 0, \quad c_i(0) = c_i$$

$$z = \delta, \quad c_i(\delta) = c_{i,m}$$

The solution of the equation will be

$$c_i(z) = \frac{c_i - c_{i,m}}{1 - e^{v_z/k_i}} e^{(v_z/D_i)z} + \frac{c_{i.m} - c_i e^{v_z/k_i}}{1 - e^{v_z/k_i}}$$

Where $k_i = D_i/\delta$, and the flux through the interface will be obtained as

$$j_i = \frac{v_z}{1 - e^{v_z/k_i}} \cdot \left(c_{i,m} - c_i e^{v_z/k_i} \right)$$

After substituting, mass transfer (flux) through the membrane will be driven as below:

$$J_{i,m} = \frac{v_z}{1 - e^{v_z/k_i}} \cdot \left(c_{i,m} - c_i e^{v_z/k_i} \right)$$

$$- w_{i,p} . \rho_p . k_v \left[\int_0^\infty (r_{v,B} - r_{v,D} + r_{S,D}^*) L^3 dL + 3 \int_0^\infty G_s . n_s . L^2 dL \right]$$

If we assume that $r_{v,B}$ and $r_{v,D}$ give only birth and breaking of particles from already existing particles, then

$$\int_0^\infty (r_{v,B} - r_{v,D}) L^3 dL = 0$$

And the flux through the membrane will be obtained as

$$J_{i,m} = \frac{v_z}{1 - e^{v_z/k_i}} \cdot \left(c_{i,m} - c_i e^{v_z/k_i} \right) - w_{i,p} . \rho_p . k_v \left[\int_0^\infty r_{S,D}^* L^3 \, dL + 3 \int_0^\infty G_s . n_s . L^2 dL \right]$$

Also, if we relate a part related to non-sticking particles to growth rate as the fraction of changed mass as follow

$$\int_0^\infty r_{S,D}^* L^3 \, dL = 3k_v \int_0^\infty k_{sv}(L) . G_s . n_s . L^2 dL$$

Here, $k_{sv}(L)$ is described which part of the particles fall to the solution. Then rewrite the equation using this definition,

$$j_{i,m} = \frac{v_z}{1 - e^{v_z/k_i}} \cdot \left(c_{i,m} - c_i e^{v_z/k_i} \right) - w_{i,p}. \rho_p. k_v \left[3 \int_0^\infty k_{sv}(L). G_s. n_s. L^2 dL + 3 \int_0^\infty G_s. n_s. L^2 dL \right]$$

If we use this definition and rewrite the equations of the component mass balance at the interface and on the membrane surface, the equations will be as follow

$$\frac{\partial (A_F. m_{i,p})}{\partial \tau} = -\frac{\partial (\dot{v}. m_{i,p})}{\partial x} + \frac{A_m}{V_R}. A_R. w_{i,p}. \rho_p. k_v. 3 \int_0^\infty k_{sv}(L). G_s. n_s. L^2 dL$$

$$+ A_F. w_{i,p}. \rho_p. 3k_v \int_0^\infty G. n. L^2 dL$$

And on the membrane surface

$$\frac{\partial (A_F. m_{i,s})}{\partial \tau} = w_{i,p}. \rho_p. k_v \left[3 \int_0^\infty k_{sv}(L). G_s. n_s. L^2 dL + 3 \int_0^\infty G_s. n_s. L^2 dL \right]$$

Therefore, component mass balance the element ΔV_R, after substitution the terms of mass balance of component i at the interface and on the membrane surface, will be obtained

$$\frac{\partial(A_F.C_i)}{\partial\tau} - \frac{\partial(\dot{v}.m_{i,p})}{\partial x} + {^{A_m}\!/_{V_R}}.A_R.w_{i,p}.\rho_p.k_v.3\int_0^\infty k_{sv}(L).G_s.n_s.L^2 dL$$

$$+ \; A_F.w_{i,p}.\rho_p.3k_v\int_0^\infty G.n.L^2 dL$$

$$+ \; {^{A_m}\!/_{V_R}}.A_R.w_{i,p}.\rho_p.k_v\left[3\int_0^\infty k_{sv}(L).G_s.n_s.L^2 dL + 3\int_0^\infty G_s.n_s.L^2 dL\right]$$

$$= -\frac{\partial(\dot{v}.C_i)}{\partial x} - \frac{\partial(\dot{v}.m_{i,p})}{\partial x} + M_i\sum_j \tilde{r}_j\tilde{v}_{i,j}.A_F - {^{A_m}\!/_{V_R}}.A_R.J_{i,m}$$

And finally, we will obtain

$$\frac{\partial(A_F.C_i)}{\partial\tau} + A_F.w_{i,p}.\rho_p.3k_v\int_0^\infty G.n.L^2 dL + {^{A_m}\!/_{V_R}}.A_R.w_{i,p}.\rho_p.3k_v\int_0^\infty G_s.n_s.L^2 dL$$

$$= -\frac{\partial(\dot{v}.C_i)}{\partial x} + M_i\sum_j \tilde{r}_j\tilde{v}_{i,j}.A_F - {^{A_m}\!/_{V_R}}.A_R.J_{i,m}$$

4.3.4. Mass balance on permeate site

4.3.4.1. Mass transfer in boundary layer: The mass transport throught the bandary layer on the permeate site, acording to film theory (Figure 60) is writen as

$$N_{i,m,P} = K_{i,P}(C_{i,m,P} - C_{i,P})$$
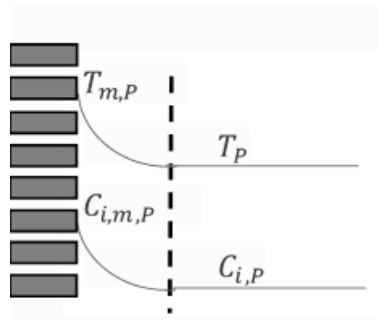
Figure 60 Boundary layer on permeate site

Where $C_{i,m,P}$ and $C_{i,P}$ are the concentration of the component i in the bulk and at the membrane surface on the permeate site.

4.3.4.2. Mass transfer in bulk solution on permeate site:

In the bulk solution on the permeate site, similar to the feed site, the component mass balance for a differential element of volume ΔV as illustrated in Figure 61 is given by
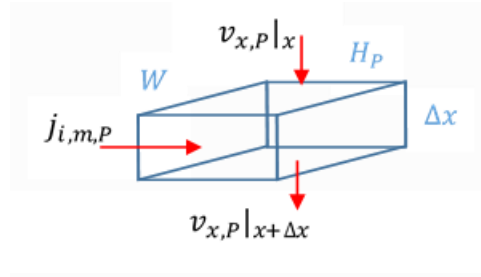
Figure 61 Component mass balance for the element ΔV on permeate site

$$W.H_P.\Delta x.C_{i,P}|_{\tau+\Delta\tau}$$
$$= W.H_P.\Delta x.C_{i,P}|_\tau + W.H_P.v_{x,P}.C_{i,P}.\Delta\tau|_x - W.H_P.v_{x,P}.C_{i,P}.\Delta\tau|_{x+\Delta x}$$
$$+ j_{i,m,P}.W.\Delta x.\Delta\tau + M_i \sum_j \tilde{r}_{j,P}\tilde{v}_{i,j}.W.H_P.\Delta x.\Delta\tau$$

After dividing by $W.H_P.\Delta x.\Delta\tau$, the equation is rewritten

$$\frac{\partial C_{i,P}}{\partial \tau} = -\frac{\partial(v_{x,P}.C_{i,P})}{\partial x} + \frac{j_{i,m,P}}{H_P} + M_i \sum_j \tilde{r}_{j,P}\tilde{v}_{i,j}$$

Where, the flow velocity in x-direction, $v_{x,P}$ is the solution flow rate per unit of cross section on permeate site, A_P

$$v_{x,P} = \frac{\dot{v}_P}{A_P}$$

Also, it can be expressed as by considering that $\rho_P = f(w_{i,P}, T_P)$

$$\dot{m}_P = \dot{v}_P \cdot \rho_P$$

The total mass balance equation can be written

$$\frac{\partial \rho_P}{\partial \tau} = -\frac{1}{A_P}\frac{\partial(\dot{v}_P \cdot \rho_P)}{\partial x} + \sum_i^n \frac{j_{i,m,P}}{H_P} + \frac{1}{A_P}\sum_i^n \sum_j \tilde{r}_{j,P}\tilde{v}_{i,j} \cdot M_i$$

Since the last term is zero (only pure water on permeate site), the equation will be obtained as following

$$\frac{\partial \rho_P}{\partial \tau} = -\frac{1}{A_P}\frac{\partial(\dot{v}_P \cdot \rho_P)}{\partial x} + \sum_i \frac{j_{i,m,P}}{H_P}$$

4.4. Heat Balance Equations

In MD module, the intermediate region of the membrane pores between the hot feed and the cold permeate, establishes thermal boundary layers at the surface of both sides of the membrane. By increasing crystal formation on the surface of the membrane, a new heat resistance layer is created in the boundary layer (Figure 62) on the feed side. Three regions of heat transfer can be distinguished in the membrane module:

i. The convective heat transfers through the feed boundary layer and crystallization heat

ii. The heat transfer through the membrane by conduction and latent heat of vaporization

iii. The convective heat transfer through the permeate boundary layer

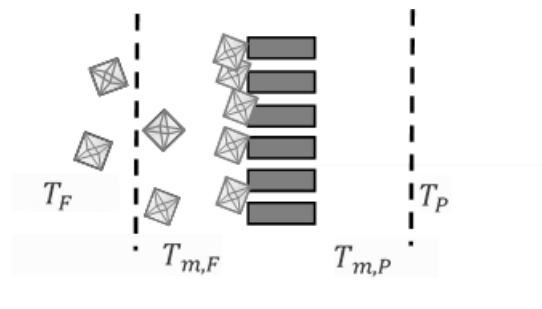

Figure 62 Heat boundary layers: T_f, bulk temperature and T_{mf}, temperature close to the membrane surface in the feed side; T_p, bulk temperature and T_{mp}, temperature close to the membrane surface in the permeate side

4.4.1. Heat balance on feed side (element ΔV_R)

For the differential element ΔV_R along the length of the membrane module on the feed side, we consider three sections: liquid ΔV, solid particles in the liquid ΔV_p and solid particles on the surface of the membrane ΔV_s as illustrated in Figure 55 and the heat balance is given

$$
\rho_l . A_F . \Delta x \sum_i h_{i,l} . w_{i,l} \mid_{\tau+\Delta\tau} + A_F . \Delta x \sum_i h_{i,P} . m_{i,p} \mid_{\tau+\Delta\tau} + {A_m}/{V_R} . A_R . \Delta x \sum_i h_{i,s} . m_{i,s} \mid_{\tau+\Delta\tau}
$$

$$
= \rho_l . A_F . \Delta x \sum_i h_{i,l} . w_{i,l} \mid_{\tau} + A_F . \Delta x \sum_i h_{i,P} . m_{i,p} \mid_{\tau}
$$

$$
+ {A_m}/{V_R} . A_R . \Delta x \sum_i h_{i,s} . m_{i,s} \mid_{\tau} + \rho_l . \dot{v} \sum_i h_{i,l} . w_{i,l} . \Delta\tau \mid_x
$$

$$
- \rho_l . \dot{v} \sum_i h_{i,l} . w_{i,l} . \Delta\tau \mid_{x+\Delta x} + \dot{v} \sum_i h_{i,P} . m_{i,p} . \Delta\tau \mid_x - \dot{v} \sum_i h_{i,P} . m_{i,p} . \Delta\tau \mid_{x+\Delta x}
$$

$$
+ A_F . \Delta x . \Delta\tau \sum_j \tilde{r}_j . (-\Delta H_r)_j - {A_m}/{V_R} . A_R . \Delta x . \Delta\tau \sum_i J_{i,m} . h_{i,v}
$$

$$
+ \dot{Q} . \Delta x . \Delta\tau . {A_{REF}}/{V_R} . A_R - {A_m}/{V_R} . A_R . \Delta x . \Delta\tau . \lambda_m . \frac{\partial T}{\partial z} \mid_{z_0}
$$

Rewrite the equation

$$
\frac{\partial (\rho_l . A_F \sum_i h_{i,l} . w_{i,l})}{\partial \tau} + \frac{\partial (A_F \sum_i h_{i,P} . m_{i,p})}{\partial \tau} + {A_m}/{V_R} . A_R . \frac{\partial (\sum_i h_{i,s} . m_{i,s})}{\partial \tau}
$$

$$
= - \frac{\partial (\rho_l . \dot{v} \sum_i h_{i,l} . w_{i,l})}{\partial x} - \frac{\partial (\dot{v} \sum_i h_{i,P} . m_{i,p})}{\partial x} + A_F \sum_j \tilde{r}_j . (-\Delta H_r)_j
$$

$$
- {A_m}/{V_R} . A_R \sum_i J_{i,m} . h_{i,v} + \dot{Q} . {A_{REF}}/{V_R} . A_R - {A_m}/{V_R} . A_R . \lambda_m . \frac{\partial T}{\partial z} \mid_{z_0}
$$

4.4.1.1. Heat balance for element ΔV_p (solid particles in the liquid)

For the differential element ΔV_p along the length of the membrane module, heat balance is given as

$$A_F.\Delta x \sum_i h_{i,P}.m_{i,p} \mid_{\tau+\Delta\tau}$$

$$= A_F.\Delta x \sum_i h_{i,P}.m_{i,p} \mid_\tau + \dot{v} \sum_i h_{i,P}.m_{i,p}.\Delta\tau \mid_x$$

$$- \dot{v} \sum_i h_{i,P}.m_{i,p}.\Delta\tau \mid_{x+\Delta x} + A_F.\Delta x.\Delta\tau.\rho_p.k_v \int_0^\infty [r_{v,B}.(-\Delta H_B)$$

$$- r_{v,D}.(\Delta H_D)].L^3 dL + {}^{A_m}/_{V_R}.A_R.\Delta x.\Delta\tau.\rho_{p,s}.k_v \int_0^\infty r_{s,D}^*.h_{p,s}.L^3 dL$$

$$+ A_F.\Delta x.\Delta\tau.\rho_p.3k_v \int_0^\infty G.n.(-\Delta H_{crys}).L^2 dL$$

Rewrite the equation

$$\frac{\partial(A_F \sum h_{i,p}.m_{i,p})}{\partial\tau}$$

$$= -\frac{\partial(\dot{v} \sum h_{i,p}.m_{i,p})}{\partial x} + A_F.\rho_p.(-\Delta H_B).k_v \int_0^\infty [r_{v,B} - r_{v,D}].L^3 dL$$

$$+ {}^{A_m}/_{V_R}.A_R.\rho_{p,s}.h_{p,s}.k_v \int_0^\infty r_{s,D}^*.L^3 dL$$

$$+ A_F.\Delta x.\Delta\tau.\rho_p.(-\Delta H_{crys}).3k_v \int_0^\infty G.n.L^2 dL$$

4.4.1.2. Heat balance for element ΔV_s (solid particles sticking to the membrane)

For the differential element ΔV_s along the length of the membrane module, heat balance is given as

$$
A_m/V_R . A_R . \Delta x . \sum h_{i,s} . m_{i,s}|_{\tau+\Delta\tau}
$$

$$
= A_m/V_R . A_R . \Delta x . \sum h_{i,s} . m_{i,s}|_{\tau}
$$

$$
+ A_m/V_R . A_R . \Delta x . \Delta\tau . \rho_{p,s} . k_v \int_0^\infty (-\Delta H_{B,s})(r_{s,B} - r_{s,D}) L^3 dL
$$

$$
- A_m/V_R . A_R . \Delta x . \Delta\tau . \rho_{p,} . k_v \int_0^\infty h_{p,s} . r_{s,D}^* L^3 dL
$$

$$
+ A_m/V_R . A_R . \Delta x . \Delta\tau . \rho_{p,s} . 3k_v \int_0^\infty (-\Delta H_{crys,s}) . G_s . n_s . L^2 dL
$$

Rewrite the equation

$$
\frac{\partial(\sum h_{i,s} . m_{i,s})}{\partial\tau} = \rho_{p,s} . k_v \int_0^\infty [(-\Delta H_{B,s})(r_{s,B} - r_{s,D}) - h_{p,s} . r_{s,D}^*] L^3 dL
$$

$$
+ \rho_{p,s} . (-\Delta H_{crys,s}) . 3k_v \int_0^\infty G_s . n_s . L^2 dL
$$

We can write,

$$
m_{p,s} . h_{p,s} = \sum m_{i,s} . h_{i,s} = \sum w_{i,p,s} . m_{p,s} . h_{i,s} = m_{p,s} \sum w_{i,p,s} . h_{i,s} = m_{p,s} \sum h_{i,p}
$$

4.4.2. Heat balance on boundary layer (interface) for feed side

Here, on boundary layer for feed side (Figure 63), we consider some assumptions as following

    i.   Pseudo-stationary state

    ii.   Heat transfer is due to conduction and convection in the interface

    iii.   Parameters $\lambda, \nu, \rho_l, c_p$ are constant
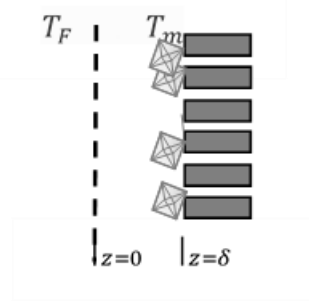
Figure 63 Boundary layer for feed side

$$\frac{dQ}{dz} = 0 \qquad \text{(is called as Eq.H1)}$$

$$Q = -\lambda \frac{dT}{dz} + \nu . H . \rho_l$$

$$\rho_l . H = \rho_l \sum w_{i,l} . h_{i,l} = \rho_l \sum w_{i,l} . h_{i,l} = \rho_l \sum w_{i,l} \int c_{p,i}(T) dT = \rho_l . \bar{c}_p (T - T_{ref})$$

$$= \bar{c}_{pv}(T - T_{ref})$$

By considering

$$w_i = \frac{m_i}{m} = \frac{c_i}{\sum c_i}$$

$$\rho_l = \sum c_i$$

118

Rewrite the equation

$$Q = -\lambda\frac{dT}{dz} + \nu.\rho_l \sum \frac{c_i}{\rho_l} \int c_{p,i}(T)dT = -\lambda\frac{dT}{dz} + \nu.\bar{c}_{pv}(T - T_{ref})$$

If c_{pi} is defined as

$$c_{pi} = a_i + b_iT + c_iT^2 + d_iT^{-2} + \frac{e_i}{T}$$

Eq.H1 is given as

$$\frac{dQ}{dz} = 0$$

$$-\lambda\frac{d^2T}{dz^2} + \nu.\bar{c}_{pv} = 0$$

$$-\lambda\frac{d^2T}{dz^2} + \nu \sum \frac{dc_i}{dz} \int_{T_{ref}}^{T} c_{p,i}(T)dT = 0$$

$$-\lambda\frac{d^2T}{dz^2} + \nu \sum (c_1.e^{\lambda_1.z} + c_2) \int_{T_{ref}}^{T} (a_i + b_iT + c_iT^2 + d_iT^{-2} + \frac{e_i}{T}) \, dT$$

$$-\lambda\frac{d^2T}{dz^2} + \nu \sum \{(c_1.e^{\lambda_1.z} + c_2)\left[a_i.T + b_i.\frac{T^2}{2} + c_i.\frac{T^3}{3} - d_i.\frac{1}{T} + e_i \ln T\right]_{T_{ref}}^{T}$$

$$+ (c_1.e^{\lambda_1.z} + c_2).(a_i + b_iT + c_iT^2 + d_iT^{-2} + \frac{e_i}{T})$$

The solution of the equation (Eq.H1) will be obtained

$$T(z) = c_1.e^{\lambda_1.z} + c_2.e^{\lambda_2.z}$$

$$T(z) = c_1.e^{z.\sqrt{k_x}} + c_2.e^{-z.\sqrt{k_x}}$$

119

Situation on boundary layer: Heat transfer through the boundary layer is given as

i. The conduction across the membrane material is in part due to the bulk membrane material conduction $Q_{\lambda,s}$ and the other is due to the vapor-filled pores $Q_{\lambda,g}$

ii. The heat of crystals transferred to the liquid

iii. The heat of crystallization

iv. The transmembrane heat flux Q_j
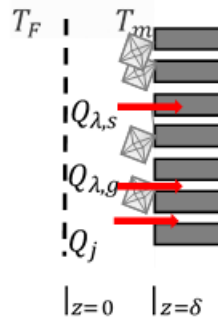
Figure 64 boundary layer for feed side

Eq. H2 is given as

$$Q|_{z=0} = -\lambda_{m,s}.(1-\varepsilon_m).\frac{dT_{m,s}}{dz_m}|_{z=0} - \lambda_{m,g}.\varepsilon_m.\frac{dT_{m,g}}{dz_m}|_{z=0}$$

$$+ \rho_{p,s}.k_v \int_0^\infty \left[(\Delta H_{B,s}).(r_{s,B}-r_{s,D}) - h_{p,s}.r_{s,D}^*\right].L^3 dL$$

$$+ \rho_{p,s}.3k_v \int_0^\infty (-\Delta H_{crys,s}).G_s.n_s.L^2 dL + \sum j_{i,m}.h_{i,g}$$

According to the boundary conditions:

$$T(z=0) = T_f$$

$$T(z=\delta) = T_m$$

If $T_f = C_1 + C_2$

$$T_m = C_1 e^{\lambda_1 \delta} + C_2 e^{-\lambda_1 \delta}$$

$$T_m = (T_f - C_2)e^{\lambda_1 \delta} + C_2 e^{-\lambda_1 \delta}$$

$$C_2 = \frac{T_m - T_f e^{\lambda_1 \delta}}{e^{-\lambda_1 \delta} - e^{\lambda_1 \delta}}$$

$$C_1 = T_f - \frac{T_m - T_f e^{\lambda_1 \delta}}{e^{-\lambda_1 \delta} - e^{\lambda_1 \delta}}$$

$$C_1 = \frac{T_f(e^{-\lambda_1 \delta} - e^{\lambda_1 \delta}) - T_m - T_f e^{\lambda_1 \delta}}{e^{-\lambda_1 \delta} - e^{\lambda_1 \delta}}$$

$$C_1 = \frac{T_f \cdot e^{-\lambda_1 \delta} - T_m}{e^{-\lambda_1 \delta} - e^{\lambda_1 \delta}}$$

$$\lambda_1 = \sqrt{\frac{v \cdot \bar{c}_{pv}}{\lambda}}$$

The solution of the equation (Eq.H1) is obtained as

$$T(z) = \frac{T_f e^{-\lambda_1 \delta} - T_m}{e^{-\lambda_1 \delta} - e^{\lambda_1 \delta}} \cdot e^{\lambda_1 z} + \frac{T_m - T_f e^{\lambda_1 \delta}}{e^{-\lambda_1 \delta} - e^{\lambda_1 \delta}} \cdot e^{-\lambda_1 z}$$

Eq. 3H is given as

$$Q|_{z=0} = (-\lambda \frac{dT}{dz} + v \sum c_i \int_{T_{ref}}^{T} c_{p,i}(T)dT)|_{z=0}$$

$$Q|_{z=0} = -\lambda(c_1 \lambda_1 - c_2 \lambda_2) + v \sum c_i \int_{T_{ref}}^{T} c_{p,i}(T)dT$$

If we know δ , the equation (Eq. H3) can be subset to Eq. H2 or we can use

$$Q_{z=\delta} = \alpha_f(T_f - T_m)$$

4.4.3. Heat transfer in Membrane

Separated equations for solid and gas phases: $T_{m,s}$: Temperature of bulk membrane material (solid phase) and $T_{m,s}$: Temperature of vapor-filled pores (gas phase) shown in Figure 65
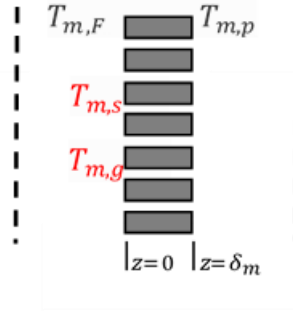
Figure 65 Membrane layer

Heat balance of solid phase is written as

$$(1 - \varepsilon_m). \rho_{m,s}. \Delta V_m \int_{T_{ref}}^{T_{m,s}} c_{p,m,s}(T)dT \mid_{\tau+\Delta\tau}$$

$$= (1 - \varepsilon_m). \rho_{m,s}. \Delta V_m \int_{T_{ref}}^{T_{m,s}} c_{p,m,s}(T)dT \mid_{\tau} - \lambda_{m,s} \frac{dT_{m,s}}{dz}. (1 - \varepsilon_m). A_m \mid_{z=z}$$

$$+ \lambda_{m,s} \frac{dT_{m,s}}{dz}. (1 - \varepsilon_m). A_m \mid_{z=z+\Delta z} + \alpha_{m,g,s}. (T_{m,g}$$

$$- T_{m,s)}. (1 - \varepsilon_m). \rho_{m,s}. A_m. \Delta\tau. \Delta z. S_m$$

Rewrite the equation

$$\rho_{m,s}. \frac{\partial(\int_{T_{ref}}^{T_{m,s}} c_{p,m,s}(T)dT)}{\partial\tau} = \frac{\partial(\lambda_{m,s} \frac{dT_{m,s}}{dz})}{\partial z} + \alpha_{m,g,s}. \rho_{m,s}. S_m. (T_{m,g} - T_{m,s)}$$

$$\rho_{m,s}. \frac{\partial(\int_{T_{ref}}^{T_{m,s}} c_{p,s}(T)dT)}{\partial\tau} = \frac{\partial(\lambda_{m,s} \frac{dT_{m,s}}{dz})}{\partial z} + \alpha_{m,g,s}. \rho_{m,s}. S_m. (T_{m,g} - T_{m,s)}$$

$$\rho_{m,s}.\frac{\partial(\int_{T_{ref}}^{T_{m,s}} c_{p,m,s}(T)dT)}{\partial\tau} = \rho_{m,s}.\frac{\partial H_s}{\partial\tau} = \frac{\partial(\lambda_{m,s}.\partial T_{m,s})}{\partial z^2} + \alpha_{m,g,s}.\rho_{m,s}.S_m.(T_{m,g} - T_{m,s})$$

Heat balance of gas phase is written as:

$$\rho_{m,g}.\varepsilon_m.\Delta V_m.\sum h_{i,g}.w_{i,g}\,|_{\tau+\Delta\tau}$$

$$= \rho_{m,g}.\varepsilon_m.\Delta V_m.\sum h_{i,g}.w_{i,g}\,|_\tau + \sum j_{i,m}.h_i.A_m\,|_{z=z} - \sum j_{i,m}.h_i.A_m\,|_{z=z+\Delta z}$$

$$- \lambda_{m,g}\frac{dT_{m,g}}{dz}\,|_{z=z} + \lambda_{m,g}\frac{dT_{m,g}}{dz}\,|_{z=z+\Delta z} - \alpha_{m,g,s}.(T_{m,g}$$

$$- T_{m,s)}.\varepsilon_m.\rho_{m,s}.A_m.\Delta\tau.\Delta z.S_m$$

Rewrite the equation

$$\rho_{m,g}.\frac{\partial(\sum h_{i,g}.w_{i,g})}{\partial\tau} = -\frac{\partial\sum j_{i,m}.h_i}{\partial z} + \frac{\partial\lambda_{m,g}\dfrac{dT_{m,g}}{dz}}{\partial z} - \alpha_{m,g,s}.\rho_{m,s}.S_m.(T_{m,g} - T_{m,s})$$

If we consider the average temperature for membrane and vapor filled pores, and we assume that $T_{m,s} = T_{m,g} = T_m$, therefore, the heat balance in the membrane layer is similar only the calculation of c_p, h, H is averaged from both phases.

$$\Delta V_m \left[(1 - \varepsilon_m). \rho_{m,s}. H_s + \varepsilon_m. \rho_{m,g}. H_g \right] |_{\tau + \Delta \tau}$$

$$= \Delta V_m \left[(1 - \varepsilon_m). \rho_{m,s}. H_s + \varepsilon_m. \rho_{m,g}. H_g \right] |_\tau - \lambda_{m,s}. (1 - \varepsilon_m). \frac{dT_m}{dz} . A_m. \Delta \tau |_z$$

$$- \lambda_{m,g}. \varepsilon_m. \frac{dT_m}{dz} . A_m. \Delta \tau |_z + \lambda_{m,s}. (1 - \varepsilon_m). \frac{dT_m}{dz} . A_m. \Delta \tau |_{z + \Delta z}$$

$$+ \lambda_{m,g}. \varepsilon_m. \frac{dT_m}{dz} . A_m. \Delta \tau |_{z + \Delta z} + \sum j_{i,m}. h_i. A_m . \Delta \tau |_{z = z}$$

$$- \sum j_{i,m}. h_i. A_m . \Delta \tau |_{z = z + \Delta z}$$

Therefore, we will obtain,

$$\frac{\partial H_{s,g}}{\partial \tau} = \frac{\partial (\lambda_{m,g,s}. \partial T_m)}{\partial z^2} - \frac{\partial \sum j_{i,m}. h_i}{\partial z}$$

Where $\lambda_{m,g,s}$, $H_{s,g}$, H_g are obtained as:

$$\lambda_{m,g,s} = (1 - \varepsilon_m). \lambda_{m,s} + \varepsilon_m. \lambda_{m,g}$$

$$H_{s,g} = (1 - \varepsilon_m). \rho_{m,s}. H_s + \varepsilon_m. \rho_{m,g}. H_g$$

$$H_g = \sum h_{i,g}. w_{i,g}$$

4.4.4. Heat Balance for Permeate side

Heat transfer through the permeate boundary layer as shown in Figure 66 is given as

$$Q_{z=\delta_m} = \alpha_p (T_{m,p} - T_p)$$
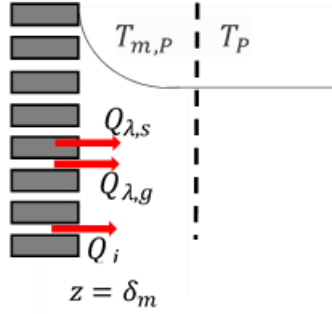
Figure 66 Boundary layer for permeate side

The conduction across the membrane material is in part due to the bulk membrane material conduction $Q_{\lambda,s}$ and the other is due to the vapor-filled pores $Q_{\lambda,g}$

$$Q_{\lambda,s} = -\lambda_{m,s} \cdot \frac{\partial T_{m,s}}{\partial z_m} \mid_{z_{m=\delta_m}} (1 - \varepsilon_m)$$

$$Q_{\lambda,g} = -\lambda_{m,g} \cdot \frac{\partial T_{m,g}}{\partial z_m} \mid_{z_{m=\delta_m}} \cdot \varepsilon_m$$

The transmembrane heat flux is written as

$$Q_j = \sum j_{i,m} \cdot h_{i,g} \mid_{z_{m=\delta_m}}$$

The total heat transfer through the permeate boundary layer can be described as

$$Q_{z=\delta_m} = Q_{\lambda,s} + Q_{\lambda,g} + Q_j$$

Therefore, the heat balance equation for permeate side is obtained as

$$l,p. A_p. \Delta x. \sum h_{i,p}. w_{i,l,p} |_{\tau + \Delta \tau}$$

$$= \rho_{l,g}. A_p. \Delta x. \sum h_{i,p}. w_{i,l,p} |_\tau + \rho_{l,p}. A_p. v \sum h_{i,p}. w_{i,l,p} |_x. \Delta \tau$$

$$- \rho_{l,p}. A_p. v \sum h_{i,p}. w_{i,l,p} |_{x+\Delta x}. \Delta \tau + Q_{z=\delta_m}. \Delta \tau. \Delta x. \frac{A_m. A_p}{V_p}$$

Rewrite the equation

$$\frac{\partial(\rho_{l,p}. \Sigma \; h_{i,p}. w_{i,l,p})}{\partial \tau} = - \frac{\partial(\rho_{l,p}. v \Sigma \; h_{i,p}. w_{i,l,p})}{\partial z^2} + Q_{z=\delta_m}. \frac{A_m}{V_p}$$

4.5. Discussion and Conclusion

In this work, a mathematical model was developed in the terms of MD performance and deposited crystal characteristics (size and number) and combining crystallization kinetic expressions with MD transport equations, the model was proposed to investigate the crystal formation along time. The balance equations were driven by considering the effect of crystal nucleation and growth in the bulk solution and on the surface of the membranes. We attempted to include the effect of crystal deposited on the surface, also the transport of no sticking crystals from the membrane surface to the interface in the population and mass balance equations. Also, in heat balance equations, we consider a new heat resistance layer created in boundary layer, due to crystal formation on the surface of membrane. Other balance equations, e.g. mass and population balance equations for the tank and the support information has been reported in appendix B. The next step will be programming which is not included in the thesis.

Chapter V:

Conclusions and Outlook

5.   Conclusions and Outlook

In this work, the design and development of novel hydrogel composite membranes for application in membrane distillation and membrane crystallization processes was investigated. To fabricate tailored HCMs with proper properties and novel functionality, two methods: surface photoinitiated polymerization and surface coating by incorporating iron oxide nanoparticles within the hydrogel matrix were applied. First, various polyelectrolyte hydrogel composite membranes were prepared by using UV initiated polymerization of functional monomers and cross-linkers on the surface of commercial PP and PES flat sheet membranes and then characterized by different techniques. Developed composites membranes demonstrated good mechanical stability under static and convective flow conditions. Changing the molar ratio between monomers in hydrogel synthesis allowed dosing the overall dissociation degree and fixed charge density in polyelectrolyte hydrogel network, thus influencing the local distribution of mobile ions at the interface with the interacting solution. The ionic-strength-responsive behavior of the developed composites provided the unique opportunity to control over mass transport and ion retention of the composites. When, such hydrogel composite membranes were used in membrane distillation experiments, higher water-transfer flux and enhanced ion rejection than traditional MD membranes was observed in MD treatment of saline solutions. By using such HCMs, in membrane crystallization of carbonate calcium, a wide range of crystals morphologies, most of them displaying a polycrystalline or mesocrystalline structure, was obtained in a great variety of experimental conditions. We demonstrated that this composite provides the opportunity to fine control the delivery of additives to the gel network through the porous structure of both support membrane and hydrogel layer, thus affecting crystallization kinetics, and crystal morphologies. In a case study, to examine the influence of the topography of hydrogel composite membranes on protein crystallization, HCMs with tailored surface roughness and patterning were designed. Iron oxide nanoparticles (NPs) were used as topographical designers providing a good control of membrane surface roughness and patterning. Surface morphology and topography of the prepared membranes were characterized using electron scanning microscopy, profilometry analysis and contact angle measurements. Thereafter, their performance was evaluated in the crystallization of Lysozyme used as a model protein. Besides the other advantages of hydrogels as suitable environment for bio (macromolecules) crystallization, the important point, was the versatility of hydrogel surfaces since they allow an easy tuning of surface patterning/roughness. We

demonstrated, roughness influences crystallization, but we also show that excessive roughness may be deleterious, since it increases the number of crystals formed at the expenses of crystal size. Therefore, there is an optimum value of roughness for the formation of a low number of well-faced crystals with a larger size. The experimental results of this study, allows to achieve new insight to fabricate and develop the novel hydrogel composite membranes with proper properties and novel functionality for application in membrane distillation and membrane crystallization processes. Lastly, in this study, the theoretical description of membrane crystallization process was investigated with the aim to better understanding of the membrane process and crystallization process. The equations for mass and heat transfers in membrane module and the crystal size distribution were derived based on different assumptions, balance equations describing the processes going through the membrane crystallization system.

References

1.   Drioli, E., E. Curcio, and G. Di Profio, *State of the art and recent progresses in membrane contactors.* Chemical Engineering Research and Design, 2005. **83**(3): p. 223-233.

2.   Stanojević, M., B. Lazarević, and D. Radić, *Review of membrane contactors designs and applications of different modules in industry.* FME Transactions, 2003. **31**(2): p. 91-98.

3.   Gabelman, A. and S.-T. Hwang, *Hollow fiber membrane contactors.* Journal of Membrane Science, 1999. **159**(1): p. 61-106.

4.   Drioli, E., A. Criscuoli, and E. Curcio, *Membrane contactors: fundamentals, applications and potentialities*. Vol. 11. 2011: Elsevier.

5.   Alkhudhiri, A., N. Darwish, and N. Hilal, *Membrane distillation: a comprehensive review.* Desalination, 2012. **287**: p. 2-18.

6.   Drioli, E., A. Ali, and F. Macedonio, *Membrane distillation: Recent developments and perspectives.* Desalination, 2015. **356**: p. 56-84.

7.   Khayet, M., *Membranes and theoretical modeling of membrane distillation: a review.* Advances in Colloid and Interface science, 2011. **164**(1): p. 56-88.

8.   Jiang, X., et al., *Membrane assisted cooling crystallization: Process model, nucleation, metastable zone, and crystal size distribution.* AIChE Journal, 2016. **62**(3): p. 829-841.

9.   Curcio, E., A. Criscuoli, and E. Drioli, *Membrane crystallizers.* Industrial & Engineering Chemistry Research, 2001. **40**(12): p. 2679-2684.

10.   Di Profio, G., E. Curcio, and E. Drioli, *4.02-Membrane Crystallization Technology.* 2010.

11.   Drioli, E., G. Di Profio, and E. Curcio, *Progress in membrane crystallization.* Current opinion in chemical engineering, 2012. **1**(2): p. 178-182.

12.   Di Profio, G., E. Curcio, and E. Drioli, *Supersaturation control and heterogeneous nucleation in membrane crystallizers: facts and perspectives.* Industrial & Engineering Chemistry Research, 2010. **49**(23): p. 11878-11889.

13.   Di Profio, G., et al., *Membrane crystallization of lysozyme: kinetic aspects.* Journal of Crystal Growth, 2003. **257**(3): p. 359-369.

14.   Di Profio, G., et al., *From tailored supports to controlled nucleation: exploring material chemistry, surface nanostructure, and wetting regime effects in heterogeneous nucleation of organic molecules.* Crystal Growth & Design, 2012. **12**(7): p. 3749-3757.

15.   Profio, G.D., et al., *Tailored hydrogel membranes for efficient protein crystallization.* Advanced Functional Materials, 2014. **24**(11): p. 1582-1590.

16.   Simone, S., et al., *Polymeric hydrophobic membranes as a tool to control polymorphism and protein–ligand interactions.* Journal of Membrane Science, 2006. **283**(1): p. 123-132.

17.   Guan, G., et al., *Analysis of membrane distillation crystallization system for high salinity brine treatment with zero discharge using Aspen flowsheet simulation.* Industrial & Engineering Chemistry Research, 2012. **51**(41): p. 13405-13413.

18.   Alklaibi, A. and N. Lior, *Membrane-distillation desalination: status and potential.* Desalination, 2005. **171**(2): p. 111-131.

19.   Drioli, E., et al., *Integrating membrane contactors technology and pressure-driven membrane operations for seawater desalination: energy, exergy and costs analysis.* Chemical Engineering Research and Design, 2006. **84**(3): p. 209-220.

20.   Ali, A., et al., *Application of Membrane Crystallization for Minerals' Recovery from Produced Water.* Membranes, 2015. **5**(4): p. 772-792.

21.   Quist-Jensen, C.A., et al., *A study of membrane distillation and crystallization for lithium recovery from high-concentrated aqueous solutions.* Journal of Membrane Science, 2016. **505**: p. 167-173.

22.   De Yoreo, J.J. and P.G. Vekilov, *Principles of crystal nucleation and growth.* Reviews in Mineralogy and Geochemistry, 2003. **54**(1): p. 57-93.

23.   Ji, X., et al., *Membrane distillation-crystallization of seawater reverse osmosis brines.* Separation and Purification Technology, 2010. **71**(1): p. 76-82.

24.   Baumgartner, J., et al., *Nucleation and growth of magnetite from solution.* Nature materials, 2013. **12**(4): p. 310-314.

25.   Weckesser, D. and A. König, *Particle shape and purity in membrane based crystallization.* Chemical Engineering & Technology, 2008. **31**(1): p. 157-162.

26.   Diao, Y., et al., *The role of nanopore shape in surface-induced crystallization.* Nature Materials, 2011. **10**(11): p. 867-871.

27.   Mullin, J.W., *Crystallization*. 2001: Butterworth-Heinemann.

28.   Di Profio, G., et al., *Selective glycine polymorph crystallization by using microporous membranes.* Crystal Growth & Design, 2007. **7**(3): p. 526-530.

29.   Bonyadi, S. and T.S. Chung, *Flux enhancement in membrane distillation by fabrication of dual layer hydrophilic–hydrophobic hollow fiber membranes.* Journal of Membrane Science, 2007. **306**(1): p. 134-146.

30.   Qtaishat, M., M. Khayet, and T. Matsuura, *Novel porous composite hydrophobic/hydrophilic polysulfone membranes for desalination by direct contact membrane distillation.* Journal of Membrane Science, 2009. **341**(1): p. 139-148.

31.   Yang, Q., et al., *Composites of functional polymeric hydrogels and porous membranes.* Journal of Materials Chemistry, 2011. **21**(9): p. 2783-2811.

32.   Montoro, S.R., S. de Fátima Medeiros, and G.M. Alves, *Nanostructured Polymer Blends: Chapter 10. Nanostructured Hydrogels*. Vol. 1. 2013: Elsevier Inc. Chapters.

33.   Peppas, N.A., et al., *Hydrogels in biology and medicine: from molecular principles to bionanotechnology.* Advanced Materials, 2006. **18**(11): p. 1345-1360.

34.   Varaprasad, K., et al., *Significances of Nanostructured Hydrogels for Valuable Applications-Chapter 8.*

35.   Hirokawa, Y. and T. Tanaka, *Volume phase transition in a nonionic gel.* The Journal of Chemical Physics, 1984. **81**(12): p. 6379-6380.

36.   Polotsky, A.A., F.A. Plamper, and O.V. Borisov, *Collapse-to-swelling transitions in pH-and thermoresponsive microgels in aqueous dispersions: The thermodynamic theory.* Macromolecules, 2013. **46**(21): p. 8702-8709.

37.   Beebe, D.J., et al., *Functional hydrogel structures for autonomous flow control inside microfluidic channels.* Nature, 2000. **404**(6778): p. 588-590.

38.   Tanaka, T., et al., *Collapse of gels in an electric field.* Science, 1982. **218**(4571): p. 467-469.

39.	Suzuki, A. and T. Tanaka, *Phase transition in polymer gels induced by visible light.* Nature, 1990. **346**(6282): p. 345-347.

40.	Kumar, A., et al., *Smart polymers: physical forms and bioengineering applications.* Progress in Polymer Science, 2007. **32**(10): p. 1205-1237.

41.	Tong, J. and J.L. Anderson, *Partitioning and diffusion of proteins and linear polymers in polyacrylamide gels.* Biophysical Journal, 1996. **70**(3): p. 1505.

42.	Tenhaeff, W.E. and K.K. Gleason, *Surface-tethered pH-responsive hydrogel thin films as size-selective layers on nanoporous asymmetric membranes.* Chemistry of Materials, 2009. **21**(18): p. 4323-4331.

43.	Yusof, A.H.M. and M. Ulbricht, *Structure variations of the grafted functional polymer brush enhance membrane adsorber performance.* Desalination, 2009. **236**(1): p. 16-22.

44.	Yang, Y.-F., et al., *Surface hydrophilization of microporous polypropylene membrane by grafting zwitterionic polymer for anti-biofouling.* Journal of Membrane Science, 2010. **362**(1): p. 255-264.

45.	Bernstein, R., E. Antón, and M. Ulbricht, *Tuning the nanofiltration performance of thin film strong polyelectrolyte hydrogel composite membranes by photo-grafting conditions.* Journal of Membrane Science, 2013. **427**: p. 129-138.

46.	Ulbricht, M., et al., *Photo-induced graft polymerization surface modifications for the preparation of hydrophilic and low-proten-adsorbing ultrafiltration membranes.* Journal of Membrane Science, 1996. **115**(1): p. 31-47.

47.	Susanto, H. and M. Ulbricht, *Photografted thin polymer hydrogel layers on PES ultrafiltration membranes: characterization, stability, and influence on separation performance.* Langmuir, 2007. **23**(14): p. 7818-7830.

48.	Peeva, P.D., N. Million, and M. Ulbricht, *Factors affecting the sieving behavior of anti-fouling thin-layer cross-linked hydrogel polyethersulfone composite ultrafiltration membranes.* Journal of Membrane Science, 2012. **390**: p. 99-112.

49.	Stanton, B.W., et al., *Ultrathin, multilayered polyelectrolyte films as nanofiltration membranes.* Langmuir, 2003. **19**(17): p. 7038-7042.

50.	Ouyang, L., R. Malaisamy, and M.L. Bruening, *Multilayer polyelectrolyte films as nanofiltration membranes for separating monovalent and divalent cations.* Journal of Membrane Science, 2008. **310**(1): p. 76-84.

51.	Herzberg, M., et al., *Surface properties and reduced biofouling of graft-copolymers that possess oppositely charged groups.* Biomacromolecules, 2011. **12**(4): p. 1169-1177.

52.	Ulbricht, M. and H.-H. Schwarz, *Novel high performance photo-graft composite membranes for separation of organic liquids by pervaporation.* Journal of Membrane Science, 1997. **136**(1): p. 25-33.

53.	Lin, P.-J., et al., *Prevention of surfactant wetting with agarose hydrogel layer for direct contact membrane distillation used in dyeing wastewater treatment.* Journal of Membrane Science, 2015. **475**: p. 511-520.

54.	Lin, X., R. Huang, and M. Ulbricht, *Novel magneto-responsive membrane for remote control switchable molecular sieving.* Journal of Materials Chemistry B, 2016. **4**(5): p. 867-879.

55.	Frey, W., D.E. Meyer, and A. Chilkoti, *Dynamic addressing of a surface pattern by a stimuli-responsive fusion protein.* Advanced Materials, 2003. **15**(3): p. 248-251.

56.   Mart, R.J., et al., *Peptide-based stimuli-responsive biomaterials.* Soft Matter, 2006. **2**(10): p. 822-835.

57.   Jiang, W., et al., *Pore-filled cation-exchange membranes containing poly (styrenesulfonic acid) gels.* Desalination, 2003. **159**(3): p. 253-266.

58.   Bernstein, R., E. Antón, and M. Ulbricht, *UV-photo graft functionalization of polyethersulfone membrane with strong polyelectrolyte hydrogel and its application for nanofiltration.* ACS applied Materials & Interfaces, 2012. **4**(7): p. 3438-3446.

59.   Kopeček, J. and J. Yang, *Smart Self-Assembled Hybrid Hydrogel Biomaterials.* Angewandte Chemie International Edition, 2012. **51**(30): p. 7396-7417.

60.   Yu, Q., et al., *Responsive biomimetic hydrogel valve for microfluidics.* Applied Physics Letters, 2001. **78**(17): p. 2589-2591.

61.   Longo, G.S., M. Olvera de La Cruz, and I. Szleifer, *Molecular theory of weak polyelectrolyte gels: the role of pH and salt concentration.* Macromolecules, 2010. **44**(1): p. 147-158.

62.   Li, J., Z. Suo, and J.J. Vlassak, *A model of ideal elastomeric gels for polyelectrolyte gels.* Soft Matter, 2014. **10**(15): p. 2582-2590.

63.   Gianneli, M., et al., *Dynamic Response of Anchored Poly (N-isopropylacrylamide-co-methacrylic acid-co-benzophenone methacrylate) Terpolymer Hydrogel Layers to Physicochemical Stimuli.* Macromolecular Chemistry and Physics, 2015. **216**(3): p. 277-286.

64.   Biesalski, M., D. Johannsmann, and J. Rühe, *Synthesis and swelling behavior of a weak polyacid brush.* The Journal of Chemical Physics, 2002. **117**(10): p. 4988-4994.

65.   Junk, M.J., et al., *Analysis of optical gradient profiles during temperature-and salt-dependent swelling of thin responsive hydrogel films.* Langmuir, 2010. **26**(14): p. 12253-12259.

66.   Gianneli, M., et al., *Dynamics of swollen gel layers anchored to solid surfaces.* Soft Matter, 2008. **4**(7): p. 1443-1447.

67.   DuPont Jr, S.J., et al., *Swelling-induced instabilities in microscale, surface-confined poly (N-isopropylacryamide) hydrogels.* Soft Matter, 2010. **6**(16): p. 3876-3882.

68.   Khurshid, S., et al., *Porous nucleating agents for protein crystallization.* Nature protocols, 2014. **9**(7): p. 1621-1633.

69.   Diao, Y., et al., *Surface design for controlled crystallization: The role of surface chemistry and nanoscale pores in heterogeneous nucleation.* Langmuir, 2011. **27**(9): p. 5324-5334.

70.   Shah, U.V., D.R. Williams, and J.Y. Heng, *Selective crystallization of proteins using engineered nanonucleants.* Crystal Growth & Design, 2012. **12**(3): p. 1362-1369.

71.   Saridakis, E., et al., *Protein crystallization facilitated by molecularly imprinted polymers.* Proceedings of the National Academy of Sciences, 2011. **108**(27): p. 11081-11086.

72.   Olle, B., et al., *Enhancement of oxygen mass transfer using functionalized magnetic nanoparticles.* Industrial & Engineering Chemistry Research, 2006. **45**(12): p. 4355-4363.

73.   Wenzel, R.N., *Resistance of solid surfaces to wetting by water.* Industrial & Engineering Chemistry, 1936. **28**(8): p. 988-994.

74.   Lawson, K.W. and D.R. Lloyd, *Membrane distillation.* Journal of Membrane Science, 1997. **124**(1): p. 1-25.

75.   Schofield, R., A. Fane, and C. Fell, *Heat and mass transfer in membrane distillation.* Journal of Membrane Science, 1987. **33**(3): p. 299-313.

76.   Song, L., et al., *Pilot plant studies of novel membranes and devices for direct contact membrane distillation-based desalination.* Journal of Membrane Science, 2008. **323**(2): p. 257-270.

77.   Gryta, M., M. Tomaszewska, and K. Karakulski, *Wastewater treatment by membrane distillation.* Desalination, 2006. **198**(1): p. 67-73.

78.   Camacho, L.M., et al., *Advances in membrane distillation for water desalination and purification applications.* Water, 2013. **5**(1): p. 94-196.

79.   Singh, D., P. Prakash, and K.K. Sirkar, *Deoiled produced water treatment using direct-contact membrane distillation.* Industrial & Engineering Chemistry Research, 2013. **52**(37): p. 13439-13448.

80.   Razmjou, A., et al., *Superhydrophobic modification of TiO 2 nanocomposite PVDF membranes for applications in membrane distillation.* Journal of membrane Science, 2012. **415**: p. 850-863.

81.   Silva, T.L., et al., *Multi-walled carbon nanotube/PVDF blended membranes with sponge-and finger-like pores for direct contact membrane distillation.* Desalination, 2015. **357**: p. 233-245.

82.   Peng, P., A. Fane, and X. Li, *Desalination by membrane distillation adopting a hydrophilic membrane.* Desalination, 2005. **173**(1): p. 45-54.

83.   Ulbricht, M. and H. Yang, *Porous polypropylene membranes with different carboxyl polymer brush layers for reversible protein binding via surface-initiated graft copolymerization.* Chemistry of Materials, 2005. **17**(10): p. 2622-2631.

84.   Drioli, E. and L. Giorno, *Comprehensive membrane science and engineering*. Vol. 1. 2010: Newnes.

85.   Mason, E.A. and A. Malinauskas, *Gas transport in porous media: the dusty-gas model*. Vol. 17. 1983: Elsevier Science Ltd.

86.   Di Profio, G., et al., *Bioinspired Synthesis of CaCO3 Superstructures through a Novel Hydrogel Composite Membranes Mineralization Platform: A Comprehensive View.* Advanced Materials, 2016. **28**(4): p. 610-616.

87.   Liu, F., et al., *Progress in the production and modification of PVDF membranes.* Journal of Membrane Science, 2011. **375**(1): p. 1-27.

88.   Aizenberg, J., et al., *Direct fabrication of large micropatterned single crystals.* Science, 2003. **299**(5610): p. 1205-1208.

89.   Tang, Z., et al., *Nanostructured artificial nacre.* Nature Materials, 2003. **2**(6): p. 413-418.

90.   Politi, Y., et al., *Sea urchin spine calcite forms via a transient amorphous calcium carbonate phase.* Science, 2004. **306**(5699): p. 1161-1164.

91.   Aizenberg, J., et al., *Calcitic microlenses as part of the photoreceptor system in brittlestars.* Nature, 2001. **412**(6849): p. 819-822.

92.   Berman, A., et al., *Biological control of crystal texture: a widespread strategy for adapting crystal properties to function.* Science, 1993. **259**(5096): p. 776-779.

93.   Sommerdijk, N.A. and G.d. With, *Biomimetic CaCO3 mineralization using designer molecules and interfaces.* Chemical Reviews, 2008. **108**(11): p. 4499-4550.

94.   Griesshaber, E., et al., *Crystallographic texture and microstructure of terebratulide brachiopod shell calcite: An optimized materials design with hierarchical architecture.* American Mineralogist, 2007. **92**(5-6): p. 722-734.

95.   Levi-Kalisman, Y., et al., *Structure of the nacreous organic matrix of a bivalve mollusk shell examined in the hydrated state using cryo-TEM.* Journal of Structural Biology, 2001. **135**(1): p. 8-17.

96.   Falini, G., et al., *Control of aragonite or calcite polymorphism by mollusk shell macromolecules.* Science, 1996. **271**(5245): p. 67.

97.   Asenath-Smith, E., et al., *Crystal growth of calcium carbonate in hydrogels as a model of biomineralization.* Advanced Functional Materials, 2012. **22**(14): p. 2891-2914.

98.   Levi, Y., et al., *Control over aragonite crystal nucleation and growth: an in vitro study of biomineralization.* Chemistry-A European Journal, 1998. **4**(3): p. 389-396.

99.   Nudelman, F., *Lessons from Biomineralization: Comparing the Growth Strategies of Mollusk Shell Prismatic and Nacreous Layers*. 2007, WEIZMANN INSTITUTE OF SCIENCE.

100.   Orme, C., et al., *Formation of chiral morphologies through selective binding of amino acids to calcite surface steps.* Nature, 2001. **411**(6839): p. 775-779.

101.   Grassmann, O. and P. Löbmann, *Biomimetic nucleation and growth of CaCO 3 in hydrogels incorporating carboxylate groups.* Biomaterials, 2004. **25**(2): p. 277-282.

102.   Filmon, R., et al., *Effects of negatively charged groups (carboxymethyl) on the calcification of poly (2-hydroxyethyl methacrylate).* Biomaterials, 2002. **23**(14): p. 3053-3059.

103.   Perkin, K.K., et al., *Fabrication of hybrid nanocapsules by calcium phosphate mineralization of shell cross-linked polymer micelles and nanocages.* Nano Letters, 2005. **5**(7): p. 1457-1461.

104.   Deng, H., et al., *Calcium carbonate crystallization controlled by functional groups: A mini-review.* Frontiers of Materials Science, 2013. **7**(1): p. 62-68.

105.   Kim, Y.-Y., et al., *A critical analysis of calcium carbonate mesocrystals.* Nature Communications, 2014. **5**.

106.   Andreassen, J.-P., R. Beck, and M. Nergaard, *Biomimetic type morphologies of calcium carbonate grown in absence of additives.* Faraday Discussions, 2012. **159**(1): p. 247-261.

107.   Prencipe, M., et al., *The vibrational spectrum of calcite (CaCO3): an ab initio quantum-mechanical calculation.* Physics and Chemistry of Minerals, 2004. **31**(8): p. 559-564.

108.   Alcoutlabi, M. and G.B. McKenna, *Effects of confinement on material behaviour at the nanometre size scale.* Journal of Physics: Condensed Matter, 2005. **17**(15): p. R461.

109.   Ouhenia, S., et al., *Synthesis of calcium carbonate polymorphs in the presence of polyacrylic acid.* Journal of Crystal Growth, 2008. **310**(11): p. 2832-2841.

110.   Zhang, F.-j., et al., *Crystallization of calcium carbonate in hydrogels in presence of meso-tetrakis (4-hydroxylphenyl) porphyrin.* Journal of Central South University, 2012. **19**(7): p. 1802-1807.

111.   Nindiyasari, F., et al., *Agregados biomiméticos de calcita crecidos en hidrogel de gelatina: efecto combinado del Mg y la concentración de sólido en el gel.* Macla, 2015(20): p. 105-106.

112.   Geladi, P. and B.R. Kowalski, *Partial least-squares regression: a tutorial.* Analytica chimica acta, 1986. **185**: p. 1-17.

113.   Tracy, S., D. Williams, and H. Jennings, *The growth of calcite spherulites from solution: II. Kinetics of formation.* Journal of Crystal Growth, 1998. **193**(3): p. 382-388.

114.   Wang, G., et al., *Biomimetic crystallization of calcium carbonate spherules controlled by hyperbranched polyglycerols.* Journal of Materials Chemistry, 2008. **18**(24): p. 2789-2797.
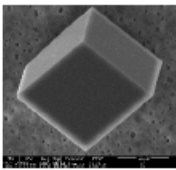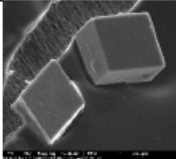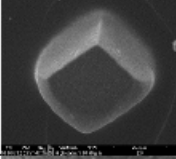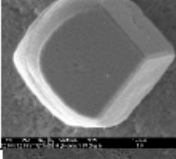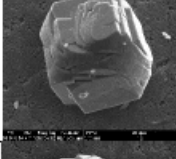
115. Tlili, M., et al., *Characterization of CaCO3 hydrates by micro-Raman spectroscopy.* Journal of Raman spectroscopy, 2002. **33**(1): p. 10-16.

116. Addadi, L., S. Raz, and S. Weiner, *Taking advantage of disorder: amorphous calcium carbonate and its roles in biomineralization.* Advanced Materials, 2003. **15**(12): p. 959-970.

117. Bentov, S., et al., *Stabilization of amorphous calcium carbonate by phosphate rich organic matrix proteins and by single phosphoamino acids.* Journal of Structural Biology, 2010. **171**(2): p. 207-215.

118. Radha, A., et al., *Transformation and crystallization energetics of synthetic and biogenic amorphous calcium carbonate.* Proceedings of the National Academy of Sciences, 2010. **107**(38): p. 16438-16443.

119. Rodriguez-Blanco, J.D., S. Shaw, and L.G. Benning, *The kinetics and mechanisms of amorphous calcium carbonate (ACC) crystallization to calcite, via vaterite.* Nanoscale, 2011. **3**(1): p. 265-271.

120. Bolze, J., et al., *Formation and growth of amorphous colloidal CaCO3 precursor particles as detected by time-resolved SAXS.* Langmuir, 2002. **18**(22): p. 8364-8369.

121. Gower, L.B., *Biomimetic model systems for investigating the amorphous precursor pathway and its role in biomineralization.* Chemical Reviews, 2008. **108**(11): p. 4551-4627.

122. Gebauer, D., A. Völkel, and H. Cölfen, *Stable prenucleation calcium carbonate clusters.* Science, 2008. **322**(5909): p. 1819-1822.

123. Pouget, E.M., et al., *The development of morphology and structure in hexagonal vaterite.* Journal of the American Chemical Society, 2010. **132**(33): p. 11560-11565.

124. Zhang, T.H. and X.Y. Liu, *How does a transient amorphous precursor template crystallization.* Journal of the American Chemical Society, 2007. **129**(44): p. 13520-13526.

125. Pichon, B.P., et al., *A quasi-time-resolved cryoTEM study of the nucleation of CaCO3 under Langmuir monolayers.* Journal of the American Chemical Society, 2008. **130**(12): p. 4034-4040.

126. Nudelman, F. and N.A. Sommerdijk, *Biomineralization as an inspiration for materials chemistry.* Angewandte Chemie International Edition, 2012. **51**(27): p. 6582-6596.

127. Benvenuti, M. and S. Mangani, *Crystallization of soluble proteins in vapor diffusion for x-ray crystallography.* Nature Protocols, 2007. **2**(7): p. 1633-1651.

128. Bolanos-Garcia, V.M. and N.E. Chayen, *New directions in conventional methods of protein crystallization.* Progress in biophysics and Molecular Biology, 2009. **101**(1): p. 3-12.

129. Nanev, C.N., *Protein crystal nucleation: Recent notions.* Crystal Research and Technology, 2007. **42**(1): p. 4-12.

130. D'Arcy, A., A. Mac Sweeney, and A. Haber, *Using natural seeding material to generate nucleation in protein crystallization experiments.* Acta Crystallographica Section D: Biological Crystallography, 2003. **59**(7): p. 1343-1346.

131. Thakur, A.S., et al., *Improved success of sparse matrix protein crystallization screening with heterogeneous nucleating agents.* PLoS One, 2007. **2**(10): p. e1091.

132. Chayen, N., et al., *Porous silicon: an effective nucleation-inducing material for protein crystallization.* Journal of Molecular Biology, 2001. **312**(4): p. 591-595.

133. Chayen, N.E., E. Saridakis, and R.P. Sear, *Experiment and theory for heterogeneous nucleation of protein crystals in a porous medium.* Proceedings of the National Academy of Sciences of the United States of America, 2006. **103**(3): p. 597-601.
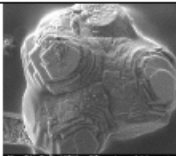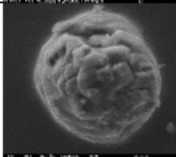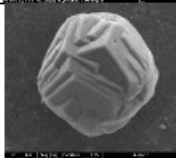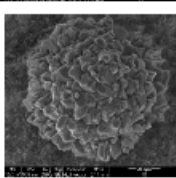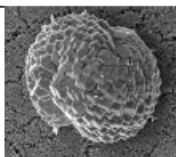
134. Rong, L., H. Komatsu, and S. Yoda, *Control of heterogeneous nucleation of lysozyme crystals by using Poly-L-Lysine modified substrate.* Journal of Crystal Growth, 2002. **235**(1): p. 489-493.

135. Nollert, P., *Lipidic cubic phases as matrices for membrane protein crystallization.* Methods, 2004. **34**(3): p. 348-353.

136. Caffrey, M. and V. Cherezov, *Crystallizing membrane proteins using lipidic mesophases.* Nature Protocols, 2009. **4**(5): p. 706-731.

137. Zheng, B., L.S. Roach, and R.F. Ismagilov, *Screening of protein crystallization conditions on a microfluidic chip using nanoliter-size droplets.* Journal of the American Chemical Society, 2003. **125**(37): p. 11170-11171.
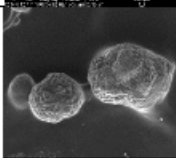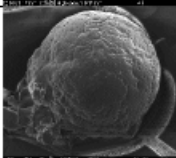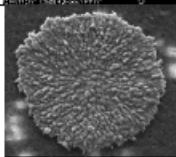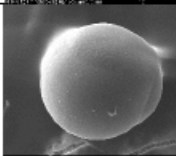
138. Shim, J.-u., et al., *Using microfluidics to decouple nucleation and growth of protein crystals.* Crystal Growth and Design, 2007. **7**(11): p. 2192-2194.

139. Asanithi, P., et al., *Carbon-nanotube-based materials for protein crystallization.* ACS Applied Materials & Interfaces, 2009. **1**(6): p. 1203-1210.

140. Sugahara, M., et al., *Nucleant-mediated protein crystallization with the application of microporous synthetic zeolites.* Acta Crystallographica Section D: Biological Crystallography, 2008. **64**(6): p. 686-695.

141. Tosi, G., et al., *Crystallization of proteins on functionalized surfaces.* Acta Crystallographica Section D: Biological Crystallography, 2008. **64**(10): p. 1054-1061.

142. Shah, U.V., et al., *Crystallization of proteins at ultralow supersaturations using novel three-dimensional nanotemplates.* Crystal Growth & Design, 2012. **12**(4): p. 1772-1777.

143. Curcio, E., G. Di Profio, and E. Drioli, *Membrane crystallization of macromolecular solutions.* Desalination, 2002. **145**(1): p. 173-177.

144. Gugliuzza, A., et al., *Novel functional per-fluorinated membranes: suitable nucleating systems for protein crystallization.* Desalination, 2006. **199**(1-3): p. 200-203.

145. Curcio, E., et al., *Energetics of protein nucleation on rough polymeric surfaces.* The Journal of Physical Chemistry B, 2010. **114**(43): p. 13650-13655.

146. Liu, Y.-X., et al., *Influence of the roughness, topography, and physicochemical properties of chemically modified surfaces on the heterogeneous nucleation of protein crystals.* The Journal of Physical Chemistry B, 2007. **111**(50): p. 13971-13978.

147. Di Profio, G., et al., *Controlling polymorphism with membrane-based crystallizers: Application to form I and II of paracetamol.* Chemistry of Materials, 2007. **19**(10): p. 2386-2388.

148. Kuhn, J., et al., *Characterization and dynamic optimization of membrane-assisted crystallization of adipic acid.* Industrial & Engineering Chemistry Research, 2009. **48**(11): p. 5360-5369.

149. Kieffer, R., et al., *Precipitation of barium sulphate in a hollow fiber membrane contactor, Part I: Investigation of particulate fouling.* Chemical Engineering Science, 2009. **64**(8): p. 1759-1767.

150. Kieffer, R., et al., *Precipitation of barium sulphate in a hollow fiber membrane contactor: Part II The influence of process parameters.* Chemical Engineering Science, 2009. **64**(8): p. 1885-1891.

151. Curcio, E., et al., *Membrane crystallization of lysozyme under forced solution flow.* Journal of Membrane Science, 2005. **257**(1): p. 134-143.

152. Julian, H., et al., *Effect of operation parameters on the mass transfer and fouling in submerged vacuum membrane distillation crystallization (VMDC) for inland brine water treatment.* Journal of Membrane Science, 2016. **520**: p. 679-692.
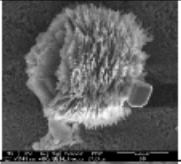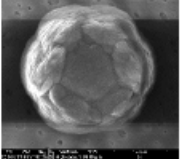
153. Shin, Y. and J. Sohn, *Mechanisms for scale formation in simultaneous membrane distillation crystallization: Effect of flow rate.* Journal of Industrial and Engineering Chemistry, 2016. **35**: p. 318-324.

154. Pantoja, C.E., Y.N. Nariyoshi, and M.M. Seckler, *Membrane distillation crystallization applied to brine desalination: A hierarchical design procedure.* Industrial & Engineering Chemistry Research, 2015. **54**(10): p. 2776-2793.

155. Pantoja, C.E., Y.N. Nariyoshi, and M.M. Seckler, *Membrane distillation crystallization applied to brine desalination: additional design criteria.* Industrial & Engineering Chemistry Research, 2016. **55**(4): p. 1004-1012.

156. Chabanon, E., D. Mangin, and C. Charcosset, *Membranes and crystallization processes: State of the art and prospects.* Journal of Membrane Science, 2016. **509**: p. 57-67.

157. Ramkrishna, D., *Population balances: Theory and applications to particulate systems in engineering*. 2000: Academic press.

Appendix A

- **Classification of SEM images of the obtained crystals**

Cluster ID	Representative image	Description	Image ID	N. of representatives	Descriptor value
1		Characteristic rhombohedral morphology of calcite expressed by six {104} symmetry-equivalent faces	34, 62, 64, 68, 69, 70, 71, 72, 73, 77, 88, 97, 101, 103, 104, 108, 109, 110, 111, 116, 119, 120, 121, 122, 124, 126	26	1
2		Rhombohedral crystals with soft appearance	54, 55, 75, 76, 78, 79, 80, 81, 82 83, 84, 85, 86, 87	14	2
3		Rhombohedral crystals with round edges, originated from the formation of {-441} and {48-1} faces	44, 99, 113, 114, 137	5	3
4		Three flat {104} faces converging to the threefold axis. Rounded {-441} and {48-1} faces on the opposite side	53, 133, 135, 136	4	4
5		{104} faces grown by the spiral mechanism at [-441] kink sites	33, 112, 117, 123, 127	5	5
6		Flat {104} faces: 2 on the top, 3 on the bottom. Several {hk0} faces determining the rounded shape along the c axis	10, 39, 40, 98, 105, 128	6	10

7		Aggregates of crystals packed along their {104} faces, grown by the spiral mechanism at [-441] kink sites	21, 52, 56, 65, 66, 118	6	10.4
8		Disordered aggregates	7, 13, 14, 15, 16, 41, 42, 45, 47, 58, 61, 89, 94	13	10.8
9		Aggregates of slightly misoriented rhombohedral crystal	36, 129, 130	3	11.2
10		Spherical aggregates, formed by crystallites having habit elongated along c axis and controlled by both {104} and {02-1} faces.	6, 50, 51, 63, 91, 93, 95	8	11.6
11		Spherical aggregates formed by rhombohedral crystals misoriented one respect to the other	8, 9, 11, 22, 23, 24, 29, 31, 37, 38, 90, 92, 96, 131	14	12.0
12		Sheaf-like aggregates formed by flat {401} faces	27, 43, 46, 57	4	12.4
13		Spherical aggregate, with rounded surface	59	1	12.8
14		Vaterite, circular shape	12, 17, 18, 19, 20, 48, 49	7	13.2
15		Vaterite, smooth and spherical shape	35, 67, 132	3	13.6

16		Aragonite	30, 100, 115, 125	4	14.0
17		Vaterite	32, 60, 134	3	14.4

- **The Partial Least Square Regression**

Let us consider N SEM images of $CaCO_3$ crystals and M experimental variables describing the experimental conditions set up during the crystallization experiments. Let us call **Y** the vector containing the N descriptor values (of size $Nx1$), and **X** the NxM matrix containing the values of the M experimental variables related to each of the N images. The Y values represent the response of the crystallization experiments, while the X values are the predictors. A linear multivariate regression is a model that tries to interpret possible linear relationship between X and Y. Formally, it can be represented by the matrix relation:

Y=XB+F (S1)

Where B is, the vector containing the M regression coefficients and says how the variables combine to form the quantitative relation between predictors and responses (of size Mx1), and F is the vector containing the N residuals (of size Nx1), expressing the deviations between observed (Y) and modelled (XB) responses. The values of Y and X have been previously properly rescaled to null mean and properly scaled standard deviation, so that they are equivalent each other and independent of their absolute values. Partial Least Square Regression (PLSR) has been used to generate the regression model. In PLS the linear regression model between predictors and response is found by projecting the 10 predicted variables and the observable variables in a new space (usually of lower dimension) where their cross-correlation is maximized. The new space is described in terms of latent variables (LV). In using this dimensionality reduction, PLSR can extract a linear relationship between predictors and responses even in case of strongly correlated variables (the so-called *collinearity*, which prevents other models, as the multiple linear regression, to be used). The experimental conditions are described in this new space by new variables, called **X**-scores (**T**), which are estimated as linear combinations of the original variables with coefficients called weights (**W**), per the following equation:

T=**XW** (S2)

Where **T** is a Nxp matrix, **W** is a Mxp matrix, and p is the (reduced) number of LV chosen to set up the regression model. The X-scores contain information about the images and their similarities/dissimilarities

with respect to the specific model, the weights give information about the relative importance of each experimental condition for the output, as well as their possible relation. Thus, for the interpretation of the PLSR model, the weights and the regression coefficients are essential for the understanding of which experimental variables is important in determining the response and which X variables provides the same information. In this view, the scores can be interpreted to represent X through proper loadings:

$\mathbf{X} = \mathbf{TP} + \mathbf{E}$ (S3)

Where $\mathbf{P}$ is the loading matrix (of size *pxM*), i.e. the weight by which each original variable should be multiplied to get the score and $\mathbf{E}$ is the unexplained residual of size *NxM*. In the same way, the scores can be used to represent the output $\mathbf{Y}$:

$\mathbf{Y} = \mathbf{TC} + \mathbf{F}$ (S4)

Through the loadings $\mathbf{C}$ (a vector of size *px1*) and the residual $\mathbf{F}$. From **Equation S4**, since the scores are function of $\mathbf{X}$, the linear relation between $\mathbf{X}$ and $\mathbf{Y}$ is inferred:

$\mathbf{Y} = \mathbf{XWC} + \mathbf{F}$, which is **Equation S1** if we put $\mathbf{B} = \mathbf{WC}$.

Two figures of merit are computed to assess the reliability of the PLSR model, which are both based on the comparison between the predictor values ($\mathbf{Y}$) and those estimated by the model

($\mathbf{XB}$): R2=1-RSS/SS and Q2=1-PRESS/SS (S5)

Where SS is the sum of squares of $\mathbf{Y}$ corrected for the mean, RSS is the fitted residual sum of squares, and PRESS is the predictive residual sum of squares that is the residual sum of squares between the model and the true values of the descriptor for those samples not included in the model estimation. The two figures of merit both range between 0 and 1, with 1 the best value. The former measures the correlation between true and estimated values by using the fitted images, the latter measures the same correlation by using images removed from the model, through a procedure called cross-validation. High R2 values indicate that the model explains most of the variance in data, while high Q2 values ensure that data is not over-fitted and have a good predicting power towards new samples. The quantities 1-R2 and 1-Q2 give an estimate of the relative mean square error made on fitted and predicted $\mathbf{Y}$ values, respectively, so giving an indication of the magnitude of the residuals contained in $\mathbf{F}$.

Predictions with the PLSR model

In the framework of multivariate statistical analysis and regression analysis, prediction is a term that refers to the capability of a model to estimate an output like the observed (experimental) one, provided a set of input. The similarity is measured per metric. It is intended that there is a sort of relation between input and output and that such relation is caught by the model up to a given level of accuracy.

Limited to such shared definitions, our PLSR model has predictive power. First, we identify the input of the model, i.e. the experimental conditions, as the cause of the output (the crystal appearance). Then, a limited set of SEM images are used to build the model, leaving out a number of images, achieved with other combinations of the experimental conditions, to make model validation. In this context, the prediction ability of the PLSR model is tested by comparing the morphology predicted by the model for the left-out experiments, once their experimental conditions are given as input, with those observed for such experiments. The similarity between the estimated and real morphology is measured using the L2 norm (see for example http://www.jstor.org/stable/1391469) and the prediction ability is quantified by the figure of merit Q2. However, we should not confer to the model recognition capabilities, and in particular the model is not able to: (i) make good predictions if the categorical variables (monomers, crosslinker, support) are not properly transformed into suitable real numbers; (ii) predict the outcome of an experiment when new experimental variables are given in input (for example a new type of monomer).

Model 1

Images more suited for the PLSR model have been selected by performing a leave-one-out (LOO) procedure: one image in turn is removed by the set and a new PLSR model is calculated on the remaining images. The values of R2 obtained by all the PLSR models can be used as a criterion for the selection of the images. Images corresponding to higher R2 values can be discarded, since by removing them the PLSR model improves as they were outliers that disturb the model itself, the contrary holds for lower R2 values. The LOO procedure has been applied on the 125 selected images, and a subset of 99 images has been selected to be included in the regression model after the application of a threshold. The correct complexity of the model, i.e. the number of latent variables to retain, has been assessed by monitoring the trends of R2 and Q2 as a function of the number of PLS components. It can be noted that both R2 and Q2 increases and they always have comparable values, which means that the model well fits the data, while maintaining a good predictive power. We considered that 2 LV adequately describe the data obtaining a model with R2= 0.870 and Q2= 0.831. The data variance explained by the first (LV1) and second (LV2) latent variables are reported in the first row of Table S1.

| Models	R^2	Q^2	Explained **X** variance (%)		Explained **Y** variance (%)	
			LV1	LV2	LV1	LV2
Model 1	0.870	0.831	35.2	15.8	84.4	2.6

.

The regressors are shown in Figure S1: Monomer 2 and Monomer ratio are by far the most important variables to set up Equation S1. They indicate a positive correlation between the experimental values used and the values of the descriptor of the related SEM images. Crosslinker concentration, Monomer 1, Support and Additive variables are also important, but their values are anti-correlated with the descriptor values. Crosslinker, $CaCl_2$ concentration and Additive concentration have a negligible role.
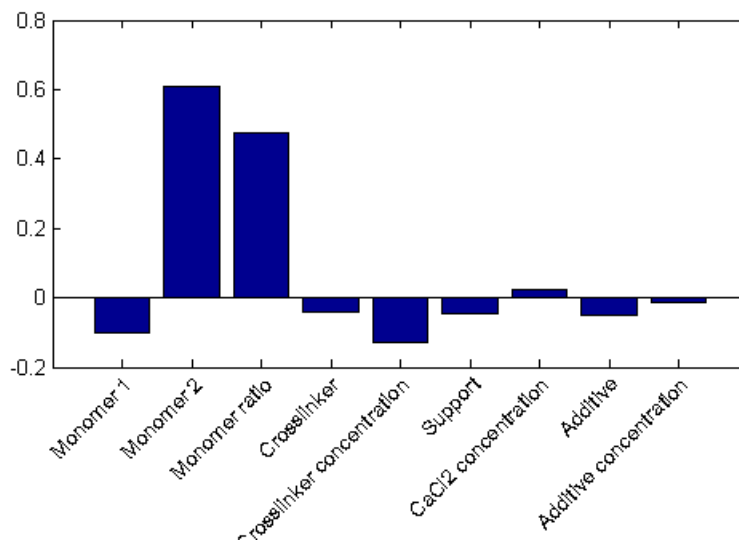
Additional interpretation can be gained by analyzing the weights of the PLSR model.Tthe weights are plotted in the space defined by the first and second latent variables. Points in the scatter plot are representative of the experimental conditions, and their distance from the origin indicates their importance in describing data variability. The major role played by Monomer 2 and Monomer ratio variables, both characterizing LV1, is confirmed. LV2 is instead mainly characterized by Additive and Support. The remaining variables have a negligible role. It is worth noting that the representative points of Monomer 1 and Crosslinker concentration are almost superimposed, indicating that they are highly correlated and achieve the same effect on the response. The same occurs for Additive and $CaCl_2$ concentrations.

Appendix B

- **Crystallization reaction:** Stoichiometry between components in solid and component in liquid is related by stoichiometry of reactions producing solid phase

$$aA_{(l)} + bB_{(l)} + cC_{(s)} \rightarrow dD_{(s)} + eE_{(s)} + fF_{(l)}$$
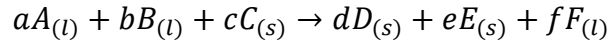
In general,

$$v_{i,j}^{(l)} A_i^{(l)} + v_{i,j}^{(s)} A_i^{(s)} = 0$$

Where, i is the component index, j is the number of reactions:

$$\begin{bmatrix} v_{1,1}^{(l)} & \cdots & v_{1,n_c}^{(l)} \\ \vdots & \ddots & \vdots \\ v_{n_r,1}^{(l)} & \cdots & v_{n_r,n_c}^{(l)} \end{bmatrix} \begin{bmatrix} n_1^{(l)} \\ \vdots \\ n_c^{(l)} \end{bmatrix} + \begin{bmatrix} v_{1,1}^{(s)} & \cdots & v_{1,n_c}^{(s)} \\ \vdots & \ddots & \vdots \\ v_{n_r,1}^{(s)} & \cdots & v_{n_r,n_c}^{(s)} \end{bmatrix} \begin{bmatrix} n_1^{(s)} \\ \vdots \\ n_c^{(s)} \end{bmatrix} = 0$$

Also, it can be rewritten

$$[v^{(l)}].\tilde{n}^{(l)} + [v^{(s)}].\tilde{n}^{(s)} = 0$$

- **Balance Equations in Tank**

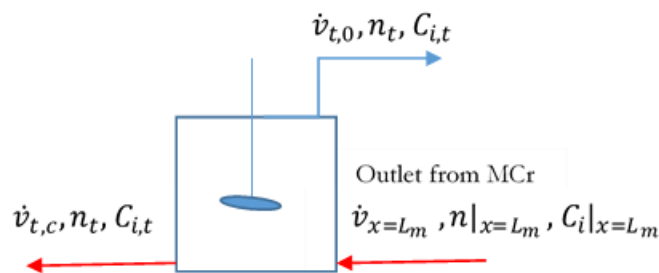**Population balance in tank:** In the crystallization tank as shown below, the PBE is given

Figure 67 Component balance on the tank

$$t . \varepsilon_t . V_t . \Delta L|_{\tau + \Delta \tau}$$

$$= n_t . \varepsilon_t . V_t . \Delta L|_{\tau} + \dot{v}_{x=L_m} . n|_{x=L_m} . \Delta L . \Delta \tau - \dot{v}_{t,0} . n_t . \Delta L . \Delta \tau - \dot{v}_{t,c} . n_t . \Delta L . \Delta \tau$$

$$+ v_L . n_t . \varepsilon_t . V_t|_L \, \Delta \tau - v_L . n_t . \varepsilon_t . V_t|_{L+\Delta L} \, \Delta \tau + \varepsilon_t . V_t . \Delta L . \Delta \tau . (r_{v,B} - r_{v,B})$$

Where V_t and ε_t are the total volume of the tank and the fraction of the total volume occupied by liquid respectively. Rewrite the equation and divide by $\Delta L . \Delta \tau$

$$\frac{\partial (n_t . \varepsilon_t . V_t)}{\partial \tau} = -\frac{\partial (v_L . n_t . \varepsilon_t . V_t)}{\partial L} + \dot{v}|_{x=L_m} . n|_{x=L_m} - \dot{v}_{t,0} . n_t - \dot{v}_{t,c} . n_t + \varepsilon_t . V_t . (r_{v,B} - r_{v,B})$$

After the substitution of the v_L by the general term of growth rate G,

$$\frac{\partial (n_t . \varepsilon_t . V_t)}{\partial \tau} = -V_t \frac{\partial (v_L . n_t . \varepsilon_t)}{\partial L} + \dot{v}|_{x=L_m} . n|_{x=L_m} - \dot{v}_{t,0} . n_t - \dot{v}_{t,c} . n_t + \varepsilon_t . V_t . (r_{v,B} - r_{v,B})$$

In the tank, ε_t is calculated

$$\varepsilon_t = 1 - \varepsilon_{p,t}$$

Where

$$\varepsilon_{p,t} = \frac{V_p}{V_t}$$

The volume is occupied by particles in the tank, is described as

$$V_p = k_v . \int_0^\infty n_t . L^3 dL . (1 - \varepsilon_{p.t}) . V_t$$

The term of $(1 - \varepsilon_{p.t}) . V_t$ goes out from integral

$$V_p = (1 - \varepsilon_{p.t}) . V_t . k_v \int_0^\infty n_t . L^3 dL$$

If rewrite the equation as

$$\frac{V_p}{V_t} = (1 - \varepsilon_{p.t}). k_v \int_0^\infty n_t. L^3 dL$$

And substitute by

$$\varepsilon_{p,t} = \frac{V_p}{V_t}$$

Rewrite the equation

$$\varepsilon_{p.t} = \frac{k_v \int_0^\infty n_t. L^3 dL}{1 - k_v \int_0^\infty n_t. L^3 dL}$$

And finally,

$$\varepsilon_t = \frac{k_v \int_0^\infty n_t. L^3 dL}{1 - 2k_v \int_0^\infty n_t. L^3 dL}$$

Mass balance of component i in tank: In the crystallization tank, the mass balance of component i is written

$$\varepsilon_t. V_t. C_{i,t}|_{\tau+\Delta\tau} + \varepsilon_t. V_t. m_{i,p,t}|_{\tau+\Delta\tau}$$
$$= \varepsilon_t. V_t. C_{i,t}|_\tau + \varepsilon_t. V_t. m_{i,p,t}|_\tau + \dot{v}|_{x=L_m}. C_i|_{x=L_m}. \Delta\tau + \dot{v}|_{x=L_m}. m_{i,p}|_{x=L_m}. \Delta\tau$$
$$- (\dot{v}_{t,0} + \dot{v}_{t,c}). C_{i,t}. \Delta\tau - (\dot{v}_{t,0} + \dot{v}_{t,c}). m_{i,p,t}. \Delta\tau$$

The equation is rewritten

$$\frac{\partial(\varepsilon_t. V_t. C_{i,t})}{\partial\tau} + \frac{\partial(\varepsilon_t. V_t. m_{i,p,t})}{\partial\tau} = \dot{v}. (C_i + m_{i,p})|_{x=L_m} - (\dot{v}_{t,0} + \dot{v}_{t,c}). C_{i.t} - (\dot{v}_{t,0} + \dot{v}_{t,c}). m_{i,p,t}$$

The mass balance of component i in solid

147

$$_t . V_t . m_{i,p,t}|_{\tau + \Delta \tau}$$

$$= \varepsilon_t . V_t . m_{i,p,t}|_\tau + \dot{v}|_{x=L_m} . m_{i,p}|_{x=L_m} . \Delta \tau - (\dot{v}_{t,0} + \dot{v}_{t,c}). \quad _{i,p,t}. \Delta \tau$$

$$+ \varepsilon_t . V_t . \Delta \tau . w_{i,p} . \rho_p . k_v \int_0^\infty (\bar{r}_{v,B} - \bar{r}_{v,D}) L^3 dL$$

$$+ \varepsilon_t . V_t . \Delta \tau . w_{i,p} . \rho_p . 3 k_v \int_0^\infty G_t . n_t . L^2 dL$$

The equation is rewritten

$$\frac{\partial (\varepsilon_t . V_t . m_{i,p,t})}{\partial \tau}$$

$$= \dot{v}. m_{i,p}|_{x=L_m} - (\dot{v}_{t,0} + \dot{v}_{t,c}). m_{i,p,t} + \varepsilon_t . V_t . w_{i,p} . \rho_p . k_v \int_0^\infty (\bar{r}_{v,B} - \bar{r}_{v,D}) L^3 dL$$

$$+ \varepsilon_t . V_t . w_{i,p} . \rho_p . 3 k_v \int_0^\infty G_t . n_t . L^2 dL$$

After substitution, the equation of the mass balance of component i in tank is derived

$$\frac{\partial (\varepsilon_t . V_t . C_{i,t})}{\partial \tau} = \dot{v}. C_i|_{x=L_m} - (\dot{v}_{t,0} + \dot{v}_{t,c}). C_{i.t} - \varepsilon_t . V_t . w_{i,p} . \rho_p . k_v \int_0^\infty (\bar{r}_{v,B} - \bar{r}_{v,D}) L^3 dL$$

$$- \varepsilon_t . V_t . w_{i,p} . \rho_p . 3 k_v \int_0^\infty G_t . n_t . L^2 d$$

Situation on boundary (Blocking/covering the pore of membrane): Since during crystallization, some pores are covered by solid particles, the pore volume should be corrected and the term of effective pore volume is defined as below

Figure 68 Covering the pore and solid part of membrane

$$\frac{eff}{m} = \frac{A_{pore} - A_{pore\ coverd}}{A_m}$$

$$\varepsilon_m^{eff} = \frac{\varepsilon_m . A_m - A_{pore\ covered}}{A_m}$$

ε_m : Porosity of membrane and can be described as A_{pore}/A_m , where A_{pore} and A_{pore} are the pore area and membrane area respectively.

$\varepsilon_s : A_s/A_m$ is defined the area covered by solid phase per membrane area.

Solid particles partially cover pores and partially cover solid part of the membrane, if we assume the same probability of coverage pore and solid part, then the term of standard ratio, $K^*_{Af,s}$ is defined

$$K^*_{Af,s} = \frac{A_{pore\ free}}{A_{m,solid\ free}} = \frac{\varepsilon_m}{1 - \varepsilon_m} = \frac{A_{pore\ covered}}{A_{m,solid\ covered}}$$

The parameter K^{mod}, ratio modification which can change the distribution between coverage of pores and solids is defined:

$$K^{mod} = \frac{A_{pore\ covered}}{A_{m,solid\ covered}} . \frac{1 - \varepsilon_m}{\varepsilon_m}$$

$K^{mod} = 1 \rightarrow$ The same probability of coverage of pore and solid part

$K^{mod} > 1 \rightarrow$ Preferred coverage of pores

$K^{mod} < 1 \rightarrow$ Preferred coverage of solid part of membrane

Therefore, $A_{m,solid\ covered}$ can be written

$$A_{m,solid\ covered} = A_{pore\ covered} . \frac{1 - \varepsilon_m}{\varepsilon_m} . K^{mod}$$

Since the solid area of the membrane, A_s is the pore covered plus the solid part of the membrane

$$A_s = A_{pore\ covered} + A_{m,solid\ covered}$$

149

and it has been defined before as

$$A_s = \varepsilon_s . A_m$$

After substitution and rewriting the equation, it is obtained

$$\varepsilon_s . A_m = A_{pore\ covered} + A_{pore\ covered} . \frac{1 - \varepsilon_m}{\varepsilon_m} . K^{mod}$$

$$\varepsilon_s . A_m = A_{pore\ covered} (1 + \frac{1 - \varepsilon_m}{\varepsilon_m} . K^{mod})$$

Finally, $A_{pore\ covered}$ can be driven as

$$A_{pore\ covered} = \frac{\varepsilon_s . A_m . \varepsilon_m . K^{mod}}{1 + \varepsilon_m (K^{mod} - 1)}$$

And the effective porosity (pore volume) after substitution of $A_{pore\ covered}$ in the equation, will be obtained as

$$\varepsilon_m^{eff} = \frac{\varepsilon_m . A_m - \dfrac{\varepsilon_s . A_m . \varepsilon_m . K^{mod}}{1 + \varepsilon_m (K^{mod} - 1)}}{A_m}$$

$$\varepsilon_m^{eff} = \frac{\varepsilon_m + \varepsilon_m^{2} (K^{mod} - 1) - \varepsilon_s . \varepsilon_m . K^{mod}}{1 + \varepsilon_m (K^{mod} - 1)}$$

$$\varepsilon_m^{eff} = \varepsilon_m . \frac{1 + (\varepsilon_m - \varepsilon_s) K^{mod} - \varepsilon_m}{1 + \varepsilon_m (K^{mod} - 1)}$$

In the case of full blocking of the pores

$$\varepsilon_m^{eff} = 0$$

Therefore

$$1 + (\varepsilon_m - \varepsilon_s{}^{BP}) K^{mod} - \varepsilon_m = 0$$

$$\varepsilon_s{}^{BP} = \frac{1 + \varepsilon_m (K^{mod} - 1)}{K^{mod}}$$

In the case of full blocking of solids in membrane

$$\varepsilon_s{}^{Bs} = 1 + \varepsilon_m(K^{mod} - 1)$$

Equilibrium at boundary (The vapor-liquid equilibrium): Mathematical equations describing this part of the process are developed based on Antoine equation and activity coefficients. Partial pressure in vapor and liquid phases are given

$$p_i^v = P.y_i$$

And

$$p_i^l = p_i^{\circ}.a_i$$

$$p_i^l = p_i^{\circ}.\gamma_i^l.x_i$$

Where γ_i^l , is activity coefficient of component i in mixture at liquid membrane interface, p_i° is vapor pressure of pure component i , is calculated using Antoine equation.

$$\log P = A - \frac{B}{C + T}$$

Where $A = 16.2620$, $B = 3799.89$ and $C = 226.85$, T is in ∘C.

Mass balance in pore volume: Component mass balance in pore volume (Figure 69) over all area of the membrane is written as
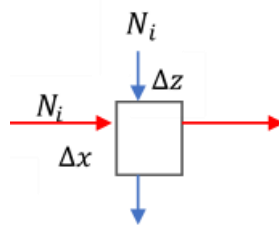

Figure 69 Mass balance in pore volume

$$\left. {}^{A_m}\!/_{L_m} . \Delta x. \Delta z. \varepsilon_m. \tilde{C}_i \right|_{\tau+\Delta\tau}$$

$$= {}^{A_m}\!/_{L_m} . \Delta x. \Delta z. \varepsilon_m. \tilde{C}_i|_{\tau} + {}^{A_m}\!/_{L_m} . \Delta x. \Delta\tau. N_i|_z - {}^{A_m}\!/_{L_m} . \Delta x. \Delta\tau. N_i|_{z+\Delta z}$$

$$+ W. \Delta z. \Delta\tau. N_i|_x - W. \Delta z. \Delta\tau. N_i|_{x+\Delta x}$$

Rewrite the equation after dividing by $\Delta x. \Delta z. \Delta\tau$

$${}^{A_m}\!/_{L_m} \frac{(\varepsilon_m. \tilde{C}_i|_{\tau+\Delta\tau} - \varepsilon_m. \tilde{C}_i|_{\tau})}{\Delta\tau} = {}^{A_m}\!/_{L_m} \frac{(N_i|_z - N_i|_{z+\Delta z})}{\Delta z} + W\frac{N_i|_x - N_i|_{x+\Delta x}}{\Delta x}$$

And then

$${}^{A_m}\!/_{L_m} \frac{\partial(\varepsilon_m. \tilde{C}_i)}{\partial\tau} = - {}^{A_m}\!/_{L_m} \frac{\partial N_i}{\partial z} - W\frac{\partial N_i}{\partial x}$$

Mass transfer in the x-direction can be neglected, therefore

$$\frac{\partial(\varepsilon_m. \tilde{C}_i)}{\partial\tau} = - \frac{\partial N_i}{\partial z}$$

Where $\tilde{C}_i$ is molar concentration of component i , therefore it can be given as

$$\frac{\partial\tilde{C}_i}{\partial\tau} = \tilde{C}\frac{\partial y_i}{\partial\tau} + y_i\frac{\partial\tilde{C}}{\partial\tau}$$

By considering the ideal gas behavior, $\tilde{C}$ can be replaced by term of ${}^{P}\!/_{RT}$

$$\frac{\partial\tilde{C}_i}{\partial\tau} = \tilde{C}\frac{\partial y_i}{\partial\tau} + y_i\frac{\partial(\frac{P}{RT})}{\partial\tau}$$

Where

$$\frac{\partial(\frac{P}{RT})}{\partial\tau} = \frac{1}{RT}\frac{\partial P}{\partial\tau} - \frac{P}{RT^2}\frac{\partial T}{\partial\tau}$$

- **Population balance of node for crystal removal**: To calculate the population density of crystals leaving the tank, it is needed to define the new parameter, split fraction, $S_r(L)$ which is expressed the amount of crystal removed per total amount of crystals in the solution and it can be calculated
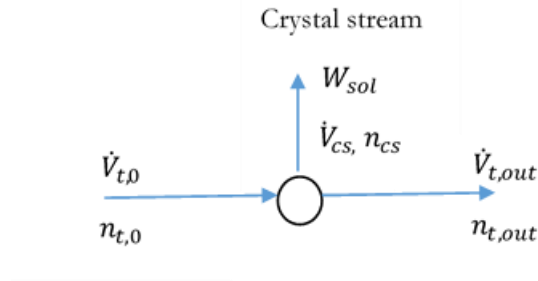

Figure 70 mass balance of a node for crystal removal

$$S_r(L) = \frac{n(L)_{cs}.\dot{v}_{cs}}{n(L)_{t,0}.\dot{v}_{t,0}}$$

Or

$$S_r(L) = \frac{\dot{m}(L)_{cs}}{\dot{m}(L)_{t,0}}$$

Where, $\dot{m}(L)_{t,0}$ is the amount of crystals in the solution leaving the membrane module and is calculated as

$$\dot{m}(L)_{t,0} = k_v.\rho_p.\dot{v}_{t,0}.n(L)_{t,0}.L^3$$

Therefore, $\dot{m}(L)_{cs}$ the amount of crystals that is filtered, is obtained as

$$\dot{m}(L)_{cs} = S_r(L).k_v.\rho_p.\dot{v}_{t,0}.n(L)_{t,0}.L^3$$

And after integrating

$$\dot{m}_{cs} = k_v.\rho_p.\dot{v}_{t,0} \int_0^\infty S_r(L).n(L)_{t,0}.L^3 dL$$

Also, according to the first equation, it can also be written

$$n(L)_{cs} = S_r(L)\frac{n(L)_{t,0}.\dot{v}_{t,0}}{\dot{v}_{cs}}$$

Since

$$\rho_{cs}.\dot{v}_{cs} = W_{sol}.\dot{m}_{cs}$$

Where, ρ_{cs} is the solution density. After substituting the terms of $\dot{v}_{cs}$ and $\dot{m}_{cs}$ in the equation, it will be obtained

$$n(L)_{cs} = \frac{S_r(L).n(L)_{t,0}.\dot{v}_{t,0}.\rho_{cs}}{W_{sol}.k_v.\rho_p.\dot{v}_{t,0}\int_0^\infty S_r(L).n(L)_{t,0}.L^3 dL}$$

The population density of crystals leaving the tank,$n(L)_{t,out}$since

$$\dot{v}_{t,out}.n(L)_{t,out} = \dot{v}_{t,0}.n(L)_{t,0} - \dot{v}_{cs}.n(L)_{cs}$$

After substituting is obtained

$$n(L)_{t,out} = \frac{\dot{v}_{t,0}.n(L)_{t,0} - \dot{v}_{cs}.n(L)_{cs}}{\dot{v}_{t,out}}$$

- **Population balance for mixer of fresh stream and recycle:** After removal of crystals, the tank outlet is mixed with the fresh feed as illustrated in Figure 71and the total mass balance and the component mass balance are given
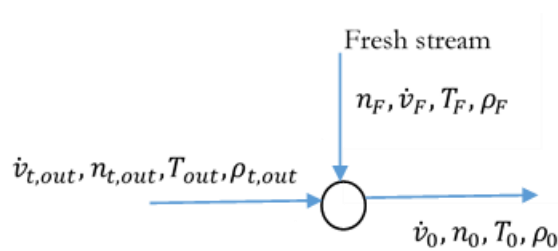

Figure 71 Mass balance for a mixer of fresh stream and recycle

$$\dot{v}_{t,out} \cdot \rho_{t,out} + \dot{v}_F \cdot \rho_F = \dot{v}_0 \cdot \rho_0$$

$$w_{i,t,out} \cdot \dot{v}_{t,out} \cdot \rho_{t,out} + w_{i,F} \cdot \dot{v}_F \cdot \rho_F = w_{i,0} \cdot \dot{v}_0 \cdot \rho_0$$

Also the PBE will be writen

$$\dot{v}_{t,out} \cdot n_{t,out}(L) + \dot{v}_F \cdot n_F(L) = \dot{v}_0 \cdot n_0(L)$$

And the energy balance

$$\dot{v}_{t,out} \cdot \rho_{t,out} \int_{T_{ref}}^{T_{t,out}} c_{p_{t,out(l)}} dT + \dot{v}_{t,out} \cdot k_v \cdot \rho_p \int_0^\infty n_{t,out}(L) \cdot L^3 dL \int_{T_{ref}}^{T_{t,out}} c_{p_{t,out(s)}} dT$$

$$+ \dot{v}_F \cdot \rho_F \int_{T_{ref}}^{T_F} c_{p_{F(l)}} dT + \dot{v}_F \cdot k_v \cdot \rho_p \int_0^\infty n_F(L) \cdot L^3 dL \cdot \int_{T_{ref}}^{T_F} c_{p_{F(s)}} dT$$

$$= \dot{v}_0 \cdot \rho_0 \int_{T_{ref}}^{T_0} c_{p_{0(l)}} dT + \dot{v}_0 \cdot k_v \cdot \rho_p \int_0^\infty n_0(L) \cdot L^3 dL \cdot \int_{T_{ref}}^{T_0} c_{p_{0(s)}} dT$$